

Study on Flow Synthesis Process for Core-Shell Nanoparticle Catalysts

橋口, 雄太

<https://hdl.handle.net/2324/6787409>

出版情報 : Kyushu University, 2022, 博士 (理学), 課程博士
バージョン :
権利関係 :

**Study on Flow Synthesis Process for Core-Shell
Nanoparticle Catalysts**

Yuta HASHIGUCHI

Catalysis Organic Chemistry Laboratory

**Department of Chemistry
Graduate School of Science
Kyushu University**

January, 2023

Contents

Chapter 1. General Introduction

1.1. Core-Shell Nanoparticle Catalysts for Fuel Cells	4
1.2. Core-Shell Nanoparticle Catalysts for Organic Synthetic Reactions.....	8
1.3. Structure of Disratitation.....	9
1.4. References	10

Chapter 2. Continuous-Flow Synthesis of Pd@Pt Core-Shell Nanoparticles

2.1. Introduction.....	13
2.2. Results and Discussion.....	15
2.3. Conclusion.....	28
2.4. Experimental	29
2.5. References	33

Chapter 3. Flow Synthesis Process for Pd@Pt Core-Shell Catalysts with Highly Controlled Pt Shell Thickness

3.1. Introduction.....	36
3.2. Results and Discussion.....	37
3.3. Conclusion.....	58
3.4. Experimental	59
3.5. References	64

Chapter 4. Effects of the Pt Shell Thickness on the Oxygen Reduction Reaction on a Well-Defined Pd@Pt Core-Shell Model Surface

4.1. Introduction.....	67
4.2. Results and Discussion.....	69
4.3. Conclusion.....	78
4.4. Experimental	79
4.5. References	82

Chapter 5. Application of Flow Synthesized Pd@Pt Core-Shell Nanoparticle Catalysts to Acceptorless Dehydrogenation of Pyrimidines from Alcohols and Amidines

5.1. Introduction.....	85
5.2. Results and Discussion.....	87
5.3. Conclusion.....	98
5.4. Experimental	99
5.5. References	104
Concluding Remarks.....	107
Acknowledgments.....	109
List of Publications.....	111

Chapter 1. General Introduction

1.1. Core-Shell Nanoparticle Catalysts for Fuel Cells

1.1.1 Fuel cells

Fuel cells are a power system that converts the chemical energy of fuel and oxidizer into electrical energy. As long as the fuel and oxidizer continue to be supplied, there is no need to recharge the battery, as is the case with batteries. Furthermore, when hydrogen is used as fuel, the only byproduct is water, which has attracted attention as a clean power source system. Fuel cells have been put to practical use in the fields of transportation, stationary, and portable power generation, and are expected to contribute to solving the global issues of energy supply and environmental problems.¹⁻³

There are several types of fuel cells, depending on the type of electrolyte used. In recent years, research has been conducted on four major types of fuel cells: polymer electrolyte fuel cells (PEFCs), phosphoric acid fuel cells (PAFCs), molten carbon salt fuel cells (MCFCs), and solid oxide fuel cells (SOFCs) (Figure. 1). Among these, PEFCs are being promoted for use in fuel cell vehicle (FCV) and household cogeneration systems because of their high energy conversion efficiency, long service life, and low temperature operation (room temperature to 120°C).

	Electrolyte	Operating temperature (°C)	Main application
PEFC	Polymer membrane	Room temperature – 120	Portable Terminal, Home Power Supply, Automobile
PAFC	Liquid H ₃ PO ₃	Approx. 200	Stationary power generation
MCFC	Molten Carbonate	Approx. 700	Stationary power generation
SOFC	Ceramic	600 - 1000	Home Power Supply, Stationary power generation

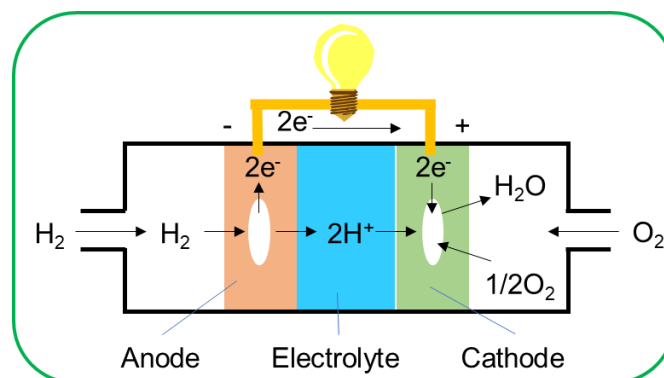
Figure 1. Various type of fuel cell

FCV is zero-emission vehicles that do not emit harmful substances such as carbon dioxide, nitrogen oxides, and sulfur oxides, which cause global warming, while driving. Compared to electric vehicle (BEV), FCV has the advantages of superior energy conservation and less susceptibility to natural battery discharge. For this reason, research and development for practical application has been widely conducted, and the world's first mass-produced FCV, Toyota Motor Corporation's MIRAI, was launched commercially in 2014.

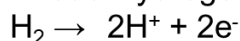
However, there are still several issues that need to be addressed to expand the use of PEFCs, one of which is the electrocatalyst. A schematic diagram of a PEFCs is shown below (Figure 2).

At the anode of the fuel cells, hydrogen oxidation reaction (HOR) occurs, producing electrons and

protons, which are transferred to the cathode via the external circuit and proton exchange membrane, respectively. At the cathode, oxygen oxidation reaction (ORR) occurs, producing water through the reaction of electrons, protons, and oxygen.



Anode: hydrogen oxidation reaction (HOR)



Cathode: oxygen oxidation reaction (ORR)

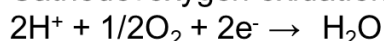


Figure 2. A schematic diagram of a PEFCs

1.1.2 Issues of fuel cell catalysts

Pt is generally the most effective catalyst for both anodes and cathodes.⁴⁻⁷ The reaction rate of HOR on Pt is so fast that only a very small amount of Pt loading on the electrocatalyst is required. On the other hand, even with Pt, the reaction rate of ORR is very slow, so more Pt must be used to achieve the desired fuel cell performance. However, since platinum is an expensive and scarce metal, a significant reduction in Pt usage is essential to expand the use of PEFCs. In addition, the problem of catalyst stability under fuel cell operating conditions has also been pointed out.⁸⁻¹²

Therefore, much research has been done on cheaper and more active electrocatalysts that use less Pt.¹³ For example, carbon-based non-precious metal and non-metal catalysts that do not use platinum at all have been reported. However, these carbon-based catalysts have many issues such as catalytic activity and catalytic lifetime. In this context, Yabu et al. reported that a catalyst combining an inexpensive carbon material (carbon black) and an azaphthalocyanine-based metal complex exhibited ORR activity comparable to or better than that of platinum catalysts under basic conditions, attracting much attention.¹⁴

Bimetallic nanocrystals combining Pt with various metals have also been widely studied. These catalysts show higher activity than Pt alone, contributing to the reduction of Pt usage. For example,

Chen et al. reported that Pt₃Ni nanoframes supported on carbon showed 20 times higher activity than carbon-supported Pt catalysts (Pt/C).¹⁵ Although the nanoframes of this catalyst have a special structure and require multiple synthesis steps, they have attracted widespread attention because of their very high activity. Bimetallic nanocrystals have a variety of structures, including core-shell, random alloy, and cluster-bonded structures.¹⁶ Among these, I focused on core-shell nanoparticles for the following reasons. Core-shell nanoparticles (Figure 3) are metal nanoparticles in which the inner core and outer shell are composed of different metals. The core metal is not directly involved in the reaction because the catalytic reaction usually proceeds only on the particle surface. Therefore, using Pt as the shell metal maximizes the efficiency of Pt utilization. Furthermore, it is expected to create a synergistic effect between Pt and core metals. The NPs are formed as a single-layer or multilayer shell structure by epitaxial growth of Pt atoms on the core metal.¹⁷

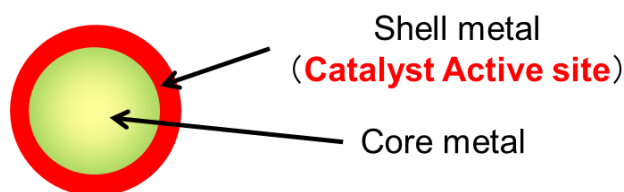


Figure 3. Core-shell structure

Because of these characteristics, core-shell catalysts with a Pt shell and various core metals have long been studied. In particular, Pd core-Pt shell (Pd@Pt) catalysts with Pd as the core metal have been reported to show an improvement in the mass activity per Pt weight (MA) compared to Pt catalysts.¹⁸⁻²²

1.1.3. Synthesis methods for core-shell nanoparticles

Various methods have been reported for the synthesis of core-shell catalysts. One example is the Cu-Underpotential Deposition method (Cu-UPD), which is a Cu-mediated platinum deposition method.²³⁻²⁵ In this method, a single layer of Cu is electrochemically deposited on a noble metal core at a lower potential than the bulk deposition (Underpotential Deposition). A Pt shell is then formed by galvanic substitution of Pt precursors (Figure 4a). Various types of core metals have been investigated. Although this method allows precise control of the Pt shell structure (ideally, a monoatomic layer of Pt (1ML) can be formed), the complexity of the process and the batch method make it a low productivity method.

Another method is the liquid-phase reduction method using a batch reactor.²³⁻²⁸ In this method,

the Pt precursor is reduced by a reducing agent in solution and deposited on the core particles to form a Pt shell (Figure 4b). Various types of core metals, solvents, capping agents, and reducing agents have been investigated. Although this method is simpler than the Cu-UPD method and therefore more versatile, it has issues such as the difficulty of precise control of the catalyst structure. In addition, because it is a batch method, there are limits to the improvement of productivity.

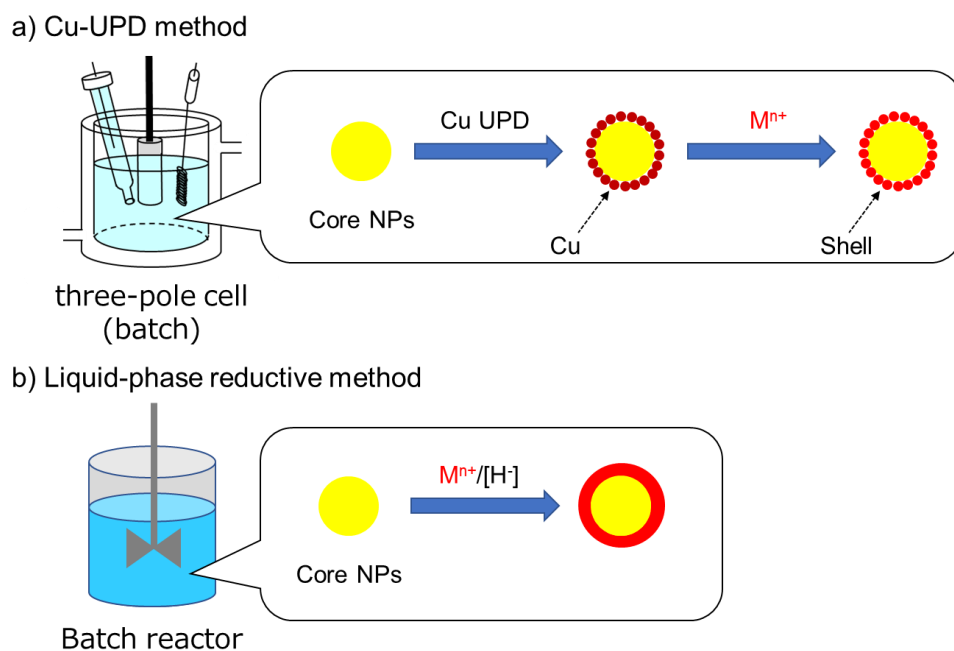


Figure 4. Existing synthesis method for core-shell nanoparticles

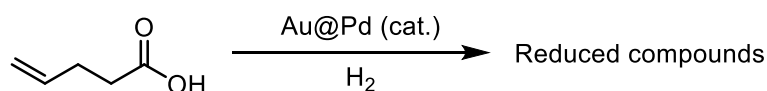
Against this background, there is a need to establish a synthesis process for core-shell catalysts that allows precise control of catalyst structure and high productivity. Recently, flow synthesis process has been attracting attention as a highly productive process capable of continuous production. In addition, flow synthesis process is characterized by its ability to control residence time and homogeneous mixing, which enables precise control of the reaction. Therefore, flow synthesis processes with precise control of particle size, size distribution, and structure of NPs have been widely studied, and synthesis of various noble metal nanoparticles has been reported.²⁹⁻³¹ However, there are only a few applications for the synthesis of core-shell nanoparticles.³²⁻³⁵ Therefore, I decided to develop a flow synthesis process for Pd@Pt catalysts in order to establish a synthetic method for core-shell type catalysts with both high productivity and advanced catalyst structure control.

1.2. Core-Shell Nanoparticle Catalysts for Organic Synthetic Reactions

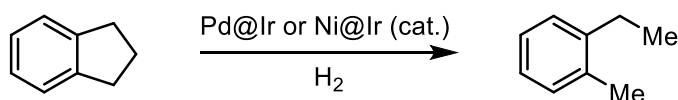
1.2.1. Various catalytic reactions using core-shell catalysts

Core-shell catalysts have also been utilized in various organic synthesis reactions, although there are fewer reported cases compared to electrocatalysts for fuel cells. For example, Mizukoshi et al. reported on the hydrogenation of 4-pentenoic acid using Au@Pd catalysts (Scheme 1a).³⁶ Semagina et al. also reported Pd@Ir and Ni@Ir catalyzed selective ring opening reaction of indan (Scheme 1b).³⁷ Furthermore, Suzuki et al. reported the oxidative esterification of aldehydes and alcohols using Au@NiO_x catalyst (Scheme 1c).³⁹ This catalyst system has been put into practical use at the methyl methacrylate (MMA) production plant of Asahi Kasei Corporation.

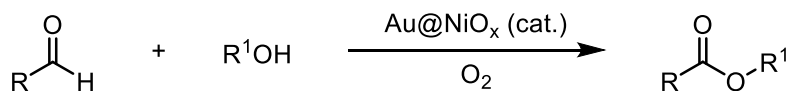
a) Hydrogenation of 4-pentenoic acid using Au@Pd (Mizukoshi et al.)



b) Selective ring opening reaction of indan using Pd@Ir and Ni@Ir (Semagina et al)



c) Oxidative esterification of aldehydes and alcohols using Au@NiO_x (Suzuki et al.)

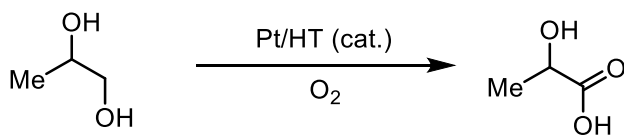


Scheme 1. Various organic synthesis reactions using core-shell catalysts

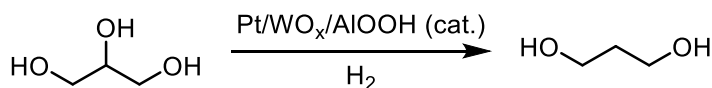
1.2.2 Pt-catalyzed organic synthesis reactions and application of flow synthesis Pd@Pt catalysts

Various organic synthetic reactions catalyzed by Pt have also been reported. For example, Ebitani et al. reported the oxidation of alcohols using Pt-supported hydrotalcite catalyst (Pt/HT) (Scheme 2a).⁴⁰ In addition, Kaneda et al. reported highly selective hydrogenolysis of 1,3-Propanediol using Pt/WO_x/AlOOH catalyst (Scheme 2b).⁴¹ Furthermore, Poly and Shimizu et al. reported Pt/C-catalyzed pyrimidine synthesis using alcohols and amidines as substrates (Scheme 2c).⁴² Since Pt is the active site of these reactions, the aforementioned flow synthesized Pd@Pt catalyst may improve catalytic activity and catalyst life. Therefore, I decided to investigate the application of the flow synthesis method of core-shell nanoparticle catalysts to organic synthesis reactions to further validate its usefulness.

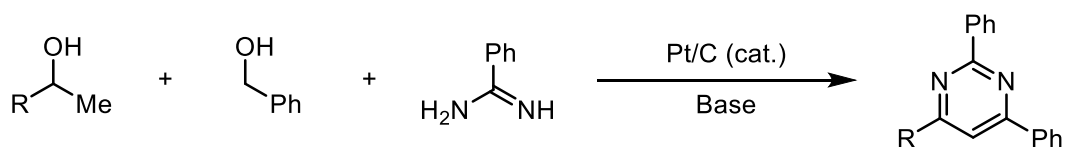
a) Oxidation of alcohols using Pt/HT (Ebitani et al.)



b) Hydrogenolysis of 1,3-Propanediol using Pt/WO_x/AlOOH (Kaneda et al.)



c) Pt/C-catalyzed pyrimidine synthesis using alcohols and amidines as substrates (Poly, Shimizu et al.)



Scheme 2. Various organic synthesis reactions using Pt catalysts

1.3. Structure of Disratitation

In disratitation, flow synthesis of core-shell nanoparticle catalysts was investigated. Chapter 2 describes the development of the flow synthesis of Pd@Pt nanoparticle catalysts. Pd@Pt/C was successfully synthesized without using polymeric capping agents that inhibit ORR activity. The obtained catalyst showed activity higher than that of Pt/C. Chapter 3 describes the development of a flow synthesis process for Pd@Pt_{1ML}/C with highly controlled Pt shell thickness. A high-throughput flow synthesis system was developed and reaction conditions were rapidly optimized. As a result, Pd@Pt_{1ML}/C with a uniform 1 ML Pt shell was successfully synthesized by using 2MePy·BH₃ as the reductant for Pt. The obtained catalysts showed catalytic activity comparable to that of the existing method (Cu-UPD) synthesis. Chapter 4 describes the results of the study on the effect of Pt shell thickness on ORR reaction in order to elucidate the factor of ORR activity on core-shell type catalysts. Pd@Pt model surface experiments and density functional theory (DFT) calculations suggest that core-shelling results in charge transfer from Pd to Pt (Pt^{δ-}), which lowers the activation energy of the rate-determining step of the ORR. In Chapter 5, I describe a three-component one-pot synthesis of multi substituted pyrimidines using Pd@Pt catalysts. Pd@Pt catalyst was effective for this reaction and showed high activity at lower catalyst loading than Pt catalyst.

1.4. References

- [1] B.C. Steele, A. Heinzl, *Nature* **2001**, *414*, 345–352.
- [2] M.K. Debe, *Nature* **2012**, *486*, 43–51.
- [3] H. Mistry, A.S. Varela, S. Kühl, P. *Nat. Rev. Mater.* **2016**, *1*, 1–14.
- [4] L. Zhang, L.T. Roling, X. Wang, M. Vara, M. Chi, J. Liu, S.-Il Choi, J. Park, J. A. Herron, Z. Xie, M. Mavrikakis, Y. Xia, *Science* **2015**, *349*, 412–416.
- [5] Y. Nie, L. Li, Z. Wei, *Chem. Soc. Rev.* **2015**, *44*, 2168–2201.
- [6] S. Guo, S. Zhang, S. Sun, *Angew. Chem. Int. Ed.* **2013**, *52*, 8526–8544.
- [7] N.V. Long, Y. Yang, C.M. Thi, N.V. Minh, Y. Cao, M. Nogami, *Nano Energy* **2013**, *2*, 636–676.
- [8] S.T. Hunt, M. Milina, A.C. Alba-Rubio, C.H. Hendon, J.A. Dumesic, Y. Rom'an-Leshkov, *Science* **2016**, *352*, 974–978.
- [9] C. Cui, L. Gan, M. Heggen, S. Rudi, P. Strasser, *Nat. Mater.* **2013**, *12*, 765–771.
- [10] Y.-J. Wang, N. Zhao, B. Fang, H. Li, X.T. Bi, H. Wang, *Chem. Rev.* **2015**, *115*, 3433–3467.
- [11] H.A. Gasteiger, S.S. Kocha, B. Sompalli, F.T. Wagner, *Appl. Catal. B* **2005**, *56*, 9–35.
- [12] J.K. Nørskov, J. Rossmeisl, A. Logadottir, L. Lindqvist, J.R. Kitchin, T. Bligaard, H. J'onsson, *J. Phys. Chem. B* **2004**, *108*, 17886–17892.
- [13] R. Ferrando, J. Jellinek, R.L. Johnston, *Chem. Rev.* **2008**, *108*, 845–910.
- [14] H. Yabu, K. Nakamura, Y. Matsuo, Y. Umejima, H. Matsuyama, J. Nakamura, K. Ito *ACS Appl. Energy Mater.* **2021**, *4*, 14380–14389.
- [15] C. Chen, Y. Kang, Z. Huo, Z. Zhu, W. Huang, H. L. Xin, J. D. Snyder, D. Li, J. A. Herron, M. Mavrikakis, M. Chi, K. L. More, Y. Li, N. M. Markovic, G. A. Somorjai, P. Yang, V. R. Stamenkovic *Science* **2014**, *343*, 1339–1343.
- [16] M. Shao, Q. Chang, J.-P. Dodelet, R. Chenitz, *Chem. Rev.* **2016**, *116*, 3594–3657.
- [17] J. Zhang, M.B. Vukmirovic, Y. Xu, M. Mavrikakis, R.R. Adzic, *Angew. Chem. Int. Ed.* **2005**, *44*, 2132–2135
- [18] R.R. Adzic, J. Zhang, K. Sasaki, M.B. Vukmirovic, M. Shao, J.X. Wang, A.U. Nilekar, M. Mavrikakis, J.A. Valerio, F. Uribe, *Top. Catal.* **2007**, *46*, 249–262.
- [19] K. Sasaki, H. Naohara, Y.-M. Choi, Y. Cai, W.-F. Chen, P. Liu, R.R. Adzic, *Nat. Commun.* **2012**, *3*, 1–9.
- [20] K. Gong, Y.-M. Choi, M.B. Vukmirovic, P. Liu, C. Ma, D. Su, R.R. Adzic, *Z. Phys. Chem.* **2012**, *226*, 1025–1038.
- [21] K. Cao, Q. Zhu, B. Shan, R. Chen, *Sci. Rep.* **2015**, *5*, 8470.
- [22] R. R. Adzic, *Electrocatalysis* **2012**, *3*, 163–169.

- [23] R. R. Adzic, J. Zhang, K. Sasaki, M.B. Vukmirovic, M. Shao, J. X. Wang, A. U. Nilekar, M. Mavrikakis, J. A. Valerio, F. Uribe, *Top. Catal.* **2007**, *46*, 249–262.
- [24] W.-P. Zhou, K. Sasaki, D. Su, Y. Zhu, J. X. Wang, R. R. Adzic, *J. Phys. Chem. C*, **2010**, *114*, 8950–8957.
- [25] N. Jung, Y.-H. Chung, D. Y. Chung, K.-H. Choi, H.-Y. Park, J. Ryu, S.-Y. Lee, M. Kim, Y.-E. Sung, S. J. Yoo, *Phys. Chem. Chem. Phys.* **2013**, *15*, 17079–17083.
- [26] B. Du, O. Zaluzhna, Y. J. Tong, *Phys. Chem. Chem. Phys.* **2011**, *13*, 11568–11574.
- [27] D. O. Atienza, T. C. Allison, Y. J. Tong, *J. Phys. Chem. C* **2012**, *116*, 26480–26486.
- [28] N. V. Long, M. Ohtaki, T. D. Hien, J. Randy, M. A. Nogami, *Electrochim. Acta* **2011**, *56*, 9133–9143.
- [29] Y. Song, J. Hormes, C.S.S.R. Kumar, *small* **2008**, *4*, 698–711.
- [30] G. Tofighi, H. Lichtenberg, J. Pesek, T.L. Sheppard, W. Wang, L. Schöttner, G. Rinke, R. Dittmeyer, J.-D. Grunwaldt, *React. Chem. Eng.* **2017**, *2*, 876–884.
- [31] M. Solsona, J.C. Vollenbroek, C.B.M. Tregouet, A.-E. Nieuwelink, W. Olthuis, A. van den Berg, B.M. Weckhuysen, M. Odijk, *Lab Chip* **2019**, *19*, 3575–3601.
- [32] M.T. Rahman, E.V. Rebrov, *Processes* **2014**, *2*, 466–493.
- [33] A. Pekkari, Z. Say, A. Susarrey-Arce, C. Langhammer, H. Härelind, V. Sebastian, K. Moth-Poulsen, *ACS Appl. Mater. Interfaces* **2019**, *11*, 36196–36204.
- [34] J. Shen, M. Shafiq, M. Ma, H. Chen, *Nanomaterials* **2020**, *10*, 1177.
- [35] S. Cattaneo, S. Althahban, S.J. Freakley, M. Sankar, T. Davies, Q. He, N. Dimitratos, C.J. Kiely, G.J. Hutchings, *Nanoscale* **2019**, *11*, 8247–8259.
- [36] Y. Mizukoshi, T. Fujimoto, Y. Nagata, R. Oshima, Y. Maeda, *J. Phys. Chem. B* **2000**, *104*, 6028–6032.
- [37] H. Ziaei-azad, C. -X. Yin, J. Shen, Y. Hub, D. Karpuzov, N. Semagina, *Journal of Catalysis* **2013**, *300*, 113–124.
- [38] H. Ziaei-Azad, N. Semagina, *ChemCatChem* **2014**, *6*, 885–894.
- [39] K. Suzuki, T. Yamaguchi, K. Matsushita, C. Iitsuka, J. Miura, T. Akaogi, H. Ishida, *ACS Catal.* **2013**, *3*, 1845–1849.
- [40] D. Tongsakul, S. Nishimura, K. Ebitani, *J. Phys. Chem. C* **2014**, *118*, 11723–11730.
- [41] R. Arundhathi, T. Mizugaki, T. Mitsudome, K. Jitsukawa, K. Kaneda, *ChemSusChem* **2013**, *6*, 1345–1347.
- [42] S. S. Poly, S.M.A.H. Siddiki, A.S. Touchy, K.W. Ting, T. Toyao, Z. Maeno, Y. Kanda, K.I. Shimizu, *ACS Catal.* **2018**, *8*, 11330–11341.

Chapter 2. Continuous-flow synthesis of Pd@Pt core-shell nanoparticles

2.1. Introduction

As mentioned in Chapter 1, Polymer electrolyte membrane fuel cells (PEFCs) are attracting much attention as a clean power supply system, but reducing the amount of expensive Pt used as a cathode catalyst is important for expanding their use. Core-shell catalysts are the predominant choice for this purpose in recent years.¹ For example, Adzic et al. have demonstrated that Pd@Pt core-shell NPs can be synthesized by the deposition of a Pt monolayer on Pd-based NPs, which are supported by electrodes, through underpotential deposition (UPD) of Cu; this process is followed by galvanic substitution with a Pt precursor.²⁻⁴ Additionally, Chen et al. have reported an atomic-scale controllable synthesis of Pd@Pt core-shell NPs by region-selective atomic layer deposition on modified substrates.⁵ In another case, it has been reported that colloidal bimetallic Cu@Ag core-shell NPs can be prepared using a simple chemical reduction method.^{6,7} In this method, polyvinyl pyrrolidone (PVP) is used as a capping agent, and ascorbic acid ($C_6H_8O_6$) and sodium borohydride ($NaBH_4$) are used as reducing agents. Moreover, the addition of ammonium hydroxide (NH_4OH) stabilized the resulting Cu@Ag core-shell NPs over time, when pure deionized water was used as a solvent.⁷ Although these prior studies report an enhanced the mass activity per Pt weight (MA) for ORR activity, the internal structure of the core-shell, exposed facet surface, and synergistic effects with the core metal have not been sufficiently clarified in terms of the effect on ORR activity.^{8,9}

More importantly, in all of these studies, the synthesis of such core-shell NPs requires the use of a substrate as a support, which severely limits large-scale production. Therefore, designing and synthesizing novel ORR catalysts that possess high catalytic activity and durability with high productivity remains an important challenge. Daimon et al. reported improved core-shell catalyst productivity by a direct substitution method that simplified Cu-UPD.¹⁰

However, even with these examples, no practical improvement in productivity has been achieved to date. Because batch reaction systems, such as the Cu-UPD method, cannot easily improve the productivity of core-shell catalysts, I attempted to apply the chemical reduction method using a continuous-flow reactor for the synthesis of core-shell catalysts.

This synthesis requires the formation of core metal particles and subsequent deposition of shell metal films in a continuous process. Therefore, I designed the flow reactor shown in Figure 1. First, the core metal precursor is reduced in the first-stage mixer (M1) to form core particles. Then, the Pt precursor mixed in the second-stage mixer (M2) is reduced by the reductant mixed in the third-stage mixer (M3) to sequentially form the Pt shell. In this case, the reactions that must be controlled include: i) formation of core particles of an appropriate particle size, ii) thickness of the shell film, iii) suppression of Pt nanoparticle formation, and iv) aggregation of NPs. In the flow process, using the

chemical reduction method, the reaction can be accurately controlled by uniformly mixing the reducing agent with the raw metal material and optimizing the residence time.

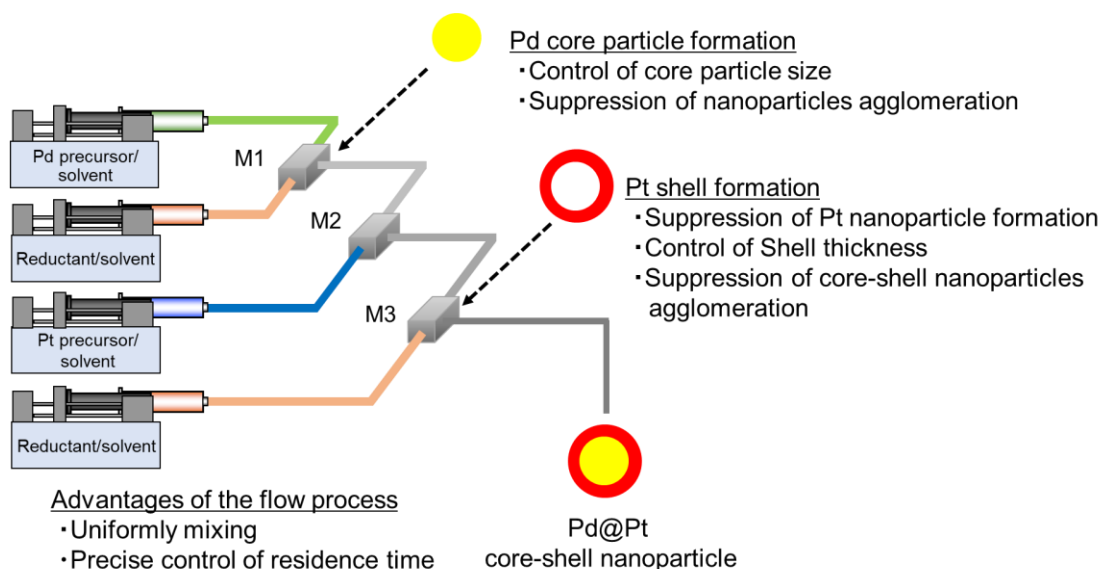


Figure 1. Flow path diagram of flow reactor for Pd@Pt core-shell NPs synthesis.

As described in Chapter 1, flow synthesis processes that precisely control the particle size, size distribution, and structure of NPs have been widely studied,¹¹⁻¹³ and the synthesis of core-shell NPs by using flow processes has been reported.¹⁴⁻¹⁷ In many of these reports, various capping agents are used to maintain the dispersibility of NPs. Hutchings et al. reported the flow synthesis of the supported Au, AuPd, and Au@Pd core-shell NPs catalysts with capping agent by a continuous stream of TiO₂ support suspended in water.¹⁷ However, capping agents cannot be used for fuel cell catalysts because they inhibit the accessibility of reaction reagents by strong adsorption to the catalytic active site.¹⁸ Therefore, it is necessary to synthesize the core-shell NPs catalysts with improved catalytic performance by a high productivity flow process. I have successfully synthesized NPs with controlled core-shell structure by the flow process without the use of capping agents that inhibit the ORR activity. In this Capture, I report the synthesis and characterization of Pd@Pt core-shell NPs with high ORR activity prepared using a continuous-flow system.

2.2. Results and Discussion

2.2.1. Synthesis conditions of Pd NPs in the flow reactor

For the synthesis of core-shell particles with a uniform structure, it is essential to control the structure of the core particles. Therefore, prior to the synthesis of core-shell NPs in a flow reactor, the synthesis reaction conditions of Pd core NPs were investigated using the flow reactor shown in Figure 2 with K_2PdCl_4 as a Pd precursor, $NaBH_4$ as a reductant, and PVP K30 as a capping agent. The obtained Pd NPs were evaluated for their average particle size and polydispersity using small angle X-ray scattering (SAXS) measurement.

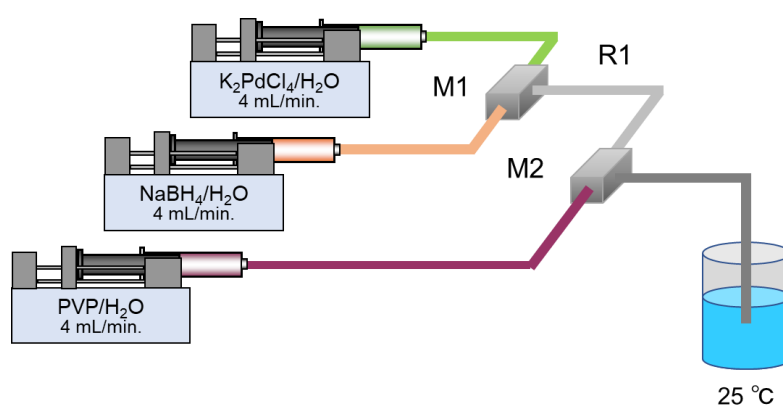


Figure 2. Schematic of Pd NPs synthesis in flow reactor

First, the effect of the ratio of the raw material Pd to the reducing agent on the size of Pd NPs was investigated. The molar ratio of $NaBH_4$ to K_2PdCl_4 ($NaBH_4/K_2PdCl_4$) was varied from 0.8 to 16 (Table 1). As a result, when the $NaBH_4/K_2PdCl_4$ ratio was 0.8 to 1.6, the average particle size of Pd NPs was about 3.0 nm. As the reductant/Pd ratio increased, the particle size of Pd NPs increased. Aggregation of Pd NPs was observed when the ratio of reductant/Pd was greater than 6.4.

Table 1. Effect of the ratio of Pd raw material to reductant on the Pd NPs size.

Molar ratio of NaBH ₄ /K ₂ PdCl ₄	Equivalence ratio	Average particle size of Pd [nm]	Polydispersion [(σ/R) ²]
0.8	1.6	2.8	0.27
1.6	3.2	3.0	0.22
3.2	6.4	3.9	0.32
6.4	12.8	Agglomeration	-
16.0	32.0	Agglomeration	-

K₂PdCl₄: 5 mM, NaBH₄: 4–80 mM, PVP: 0.1 wt%, Flow rate of K₂PdCl₄, NaBH₄, and PVP solution: 4 mL/min, Inner diameter of the mixer (M1, M2): 0.33 mm, Inner diameter of reactor: 1 mm, length: 50 mm, Reaction temperature: 25 °C.

Next, the effect of residence time in the reaction zone on the size of Pd NPs was investigated (Table 2). Residence time was adjusted by changing the length of the line (R1) in the reaction zone. Immediately after the mixer without the reaction zone, the size of Pd NPs was estimated to be 2.0 nm. The length of the reaction section was varied from 50 to 100 mm, but no significant difference in the size or polydispersity of the Pd NPs was observed. This indicates that the residence time of the raw Pd feedstock and reductant in the reaction zone has no effect on the synthesized Pd NPs.

Table 2. Effect of residence time in the reaction zone on the Pd NPs size.

Length of reaction zone [mm]	Residence time of reaction zone [s]	Average particle size of Pd [nm]	Polydispersion [(σ/R) ²]
0	0	2.0	0.25
25	0.15	2.7	0.26
50	0.30	3.0	0.22
75	0.45	3.1	0.22
100	0.60	3.1	0.23

K₂PdCl₄: 5 mM, NaBH₄: 8 mM, PVP: 0.1 wt%, Flow rate of K₂PdCl₄, NaBH₄, and PVP solution: 4 mL/min, Inner diameter of the mixer (M1, M2): 0.33 mm, Inner diameter of reactor: 1 mm, Reaction temperature: 25 °C.

The effect of the inner diameter (i.d.) of the mixer (M1) in which K₂PdCl₄ and NaBH₄ are mixed was investigated (Table 3). When the mixer I.D. was less than 0.5 mm, the diameter of the Pd NPs was 2 nm and the polydispersity was low at 0.25, indicating that uniform Pd NPs were produced. However, when the I.D. of the mixer was reduced to 0.15 mm, the diameter of the Pd NPs was as small as 1.2 nm, but the polydispersity increased to 0.42. When the mixer inner diameter was increased to 1.0 mm or larger, the diameter of the Pd NPs increased to about 2.5 nm and the polydispersity also

increased.

Table 3. Effect of the inner diameter of the mixer for mixing the K_2PdCl_4 and the $NaBH_4$.

Inner diameter of the mixer [mm]	Average particle size of Pd [nm]	Polydispersion [$(\sigma/R)^2$]
0.15	1.2	0.42
0.25	1.9	0.25
0.33	2.0	0.24
0.50	2.0	0.30
1.00	2.5	0.37
1.50	2.6	0.36
2.00	2.5	0.35

K_2PdCl_4 : 5 mM, $NaBH_4$: 8 mM, PVP: 0.1 wt%, Flow rate of K_2PdCl_4 , $NaBH_4$, and PVP solution: 4 mL/min, Inner diameter of the mixer (M1, M2): 0.15–2.00 mm, Inner diameter of reactor: 1 mm, length: 50 mm, Reaction temperature: 25 °C.

Finally, the effect of the amount of capping agent added on the size of Pd NPs was investigated (Table 4). When the PVP concentration was varied from 0.05 to 1.0 wt%, the size and polydispersity of the Pd NPs did not change. This indicates that the concentration of PVP does not significantly affect the synthesized Pd NPs.

Table 4. Effect of the amount of PVP added on the Pd NPs size.

Concentration of PVP [wt%]	Average particle size of Pd [nm]	Polydispersion [$(\sigma/R)^2$]
0.05	2.9	0.22
0.10	3.0	0.22
0.20	2.8	0.23
0.50	2.8	0.22
1.00	2.8	0.22

K_2PdCl_4 : 5 mM, $NaBH_4$: 8 mM, PVP: 0.05–1.00 wt%, Flow rate of K_2PdCl_4 , $NaBH_4$, and PVP solution: 4 mL/min, Inner diameter of the mixer (M1, M2): 0.33 mm, Inner diameter of reactor: 1 mm, length: 50 mm, Reaction temperature: 25 °C.

2.2.2. Pd@Pt core-shell synthesis in the flow reactor

Next, I synthesized Pd@Pt core-shell NPs using the flow-reactor process shown in Figure 3, with K_2PdCl_4 as a Pd precursor, H_2PtCl_6 as a Pt precursor, $NaBH_4$ as a reductant for Pd and Pt, and PVP

K30 as a capping agent. The details of the flow reactor are as follows. The reactors (R1–R3) have an I.D. of 1.0 mm and a length of 50 mm. The I.D. of each mixer (M1–M4) was 0.33 mm. The flow rates of the metal precursor, reductant, and capping agent solutions were 4 mL/min. The molar ratio of the reductant/metal precursor was 1.6, the molar ratio of the Pd/Pt precursor was 2.0, and the PVP K30 concentration was 0.1 wt%. The reaction temperature was adjusted to 25 °C. The obtained NPs were supported on carbon by the method described in the experimental section.

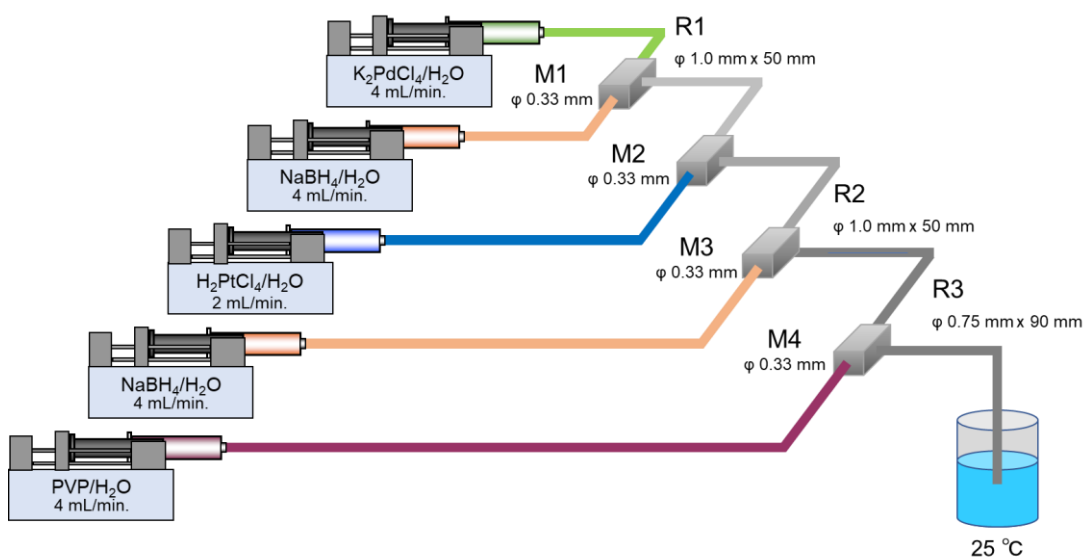


Figure 3. Schematic of the flow reactor used to synthesize Pd@Pt core-shell NPs.

The dark field scanning transmission electron microscopy (DF-STEM) image and Energy dispersive X-ray spectroscopy (EDS) mapping images of flow-synthesized Pd@Pt/PVP/C are shown in Figure 4. TEM image showed that the NPs were highly dispersed on the carbon support (Figure 4A). From the particle size analysis, the average particle size of NPs was estimated to be 3.6 nm (Figure 4B). Figure 4D shows the distribution of Pd throughout the particle in green, indicating that Pd atoms were uniformly present in the particles. In contrast, the distribution of Pt, shown in red in Figure 4E, is not uniform throughout the particle. That is, the concentration of Pt on the outer surface was high, however, the concentration inside was low. Further, the particle size of Pt is larger than that of Pd (Figure 4D and 4E). The superimposed EDS mapping of Pd and Pt (Figure. 4F) clearly shows that the outer surface of the particle is red, and the inside is green, confirming that the particle consists of a Pd core and Pt shell structure.

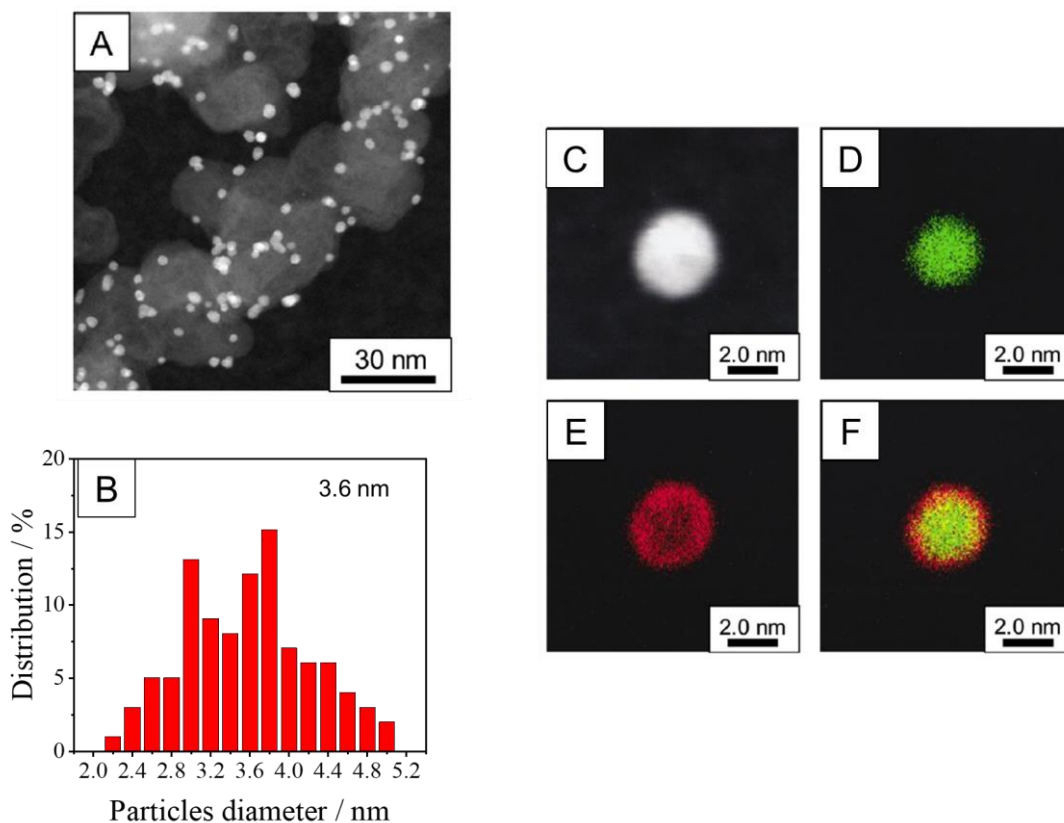


Figure 4. DF-STEM image (A), Size distributions (B) and DF-STEM-EDS mapping images (C–F), with Pd shown in green and Pt in red, of Pd@Pt/PVP/C NPs synthesized by the flow process.

Moreover, the thickness of the Pt shell was estimated to be about 0.5 nm from the Electron energy loss spectroscopy (EELS) line analysis results (Figure 5). Since the atomic diameter of Pt is 0.28 nm, the result of EELS suggesting that the Pt shell is composed of two atomic layers. Thus, the results in Figures 4 and 5 indicate that it is possible to prepare Pd@Pt core-shell catalysts in a flow system.

However, as already mentioned, the Pd/Pt metal ratio in the flow synthesis is 2/1 (mol/mol), which corresponds to a ratio of forming a monatomic layer Pt shell to a 3.5 nm core-shell particle. From the results shown in Figure 4 and 5, the observed Pd@Pt particle exhibited a particle size of approximately 3.6 nm and a Pt shell thickness of approximately two atomic layers, suggesting that the Pt shell thickness of the synthesized Pd@Pt NPs were non-uniform.

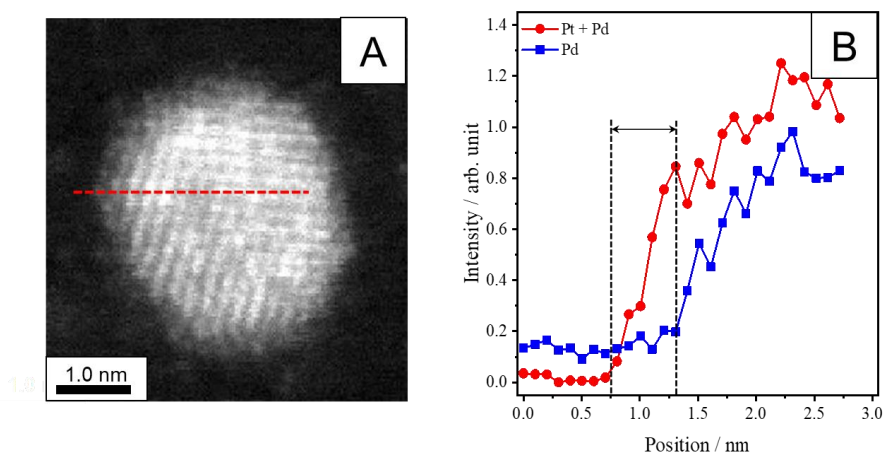


Figure 5. HAADF-STEM atomic-resolved (A) image of the Pd@Pt/PVP/C catalyst synthesized by flow method. Chemical mapping (B) of the Pd@Pt/PVP/C catalyst depicting the HAADF intensity (red curve) and the EELS signal (blue curve) derived from the Pd peak of M edge around 420 eV.

Next, the ORR activity of the synthesized Pd@Pt/PVP/C catalyst was evaluated using the rotating electrode method. For comparison, the ORR activity of commercial Pt/C was also evaluated. Details of the activity evaluation method are given in the experimental section. The results of the ORR activity evaluation of catalysts are summarized in Table 5. The electrochemical Pt surface area (ECSA) of Pd@Pt/PVP/C was approximately 2.5 times higher than that of Pt/C, indicating that Pt was abundant on the particle surface, indicating that the core-shell structure increased the concentration of Pt. Moreover, in the underpotentially adsorbed hydrogen (H_{upd}) region of the cyclic voltammetry (CV) waveform, a clear double peak was confirmed in Pt/C, however, a broad single peak was observed in Pd@Pt/PVP/C (Figure 6), suggesting that the change in the Pt peak profile of Pd@Pt/PVP/C was due to an alteration in the surface geometry of Pt caused by the formation of a Pd@Pt core-shell structure.^{19,20}

In contrast, the MA of Pd@Pt/PVP/C and Pt/C were similar, however, the specific activity (SA) of Pd@Pt/PVP/C was approximately 2.5 times smaller than that of Pt/C, indicating that the ORR activity per Pt atom of Pd@Pt/PVP/C was extremely low compared with that of Pt/C. However, the MA value of Pd@Pt/C synthesized by the Cu-UPD method has been reported to be approximately three times higher than that of Pt/C.²¹ This is most likely because PVP, which is a capping agent for NPs that not used by Cu-UPD method, inhibits the ORR activity.^{18,22,23} Safo et al. have reported that the low ORR activity of the PVP-capped Pt nanocubes is attributed to the strong adsorption behavior of PVP which blocks the catalytically active Pt sites.¹⁸ Thus, in order to improve ORR activity, it is

necessary to support the highly dispersed Pd@Pt NPs on carbon support without the use of PVP.

Table 5. ORR activities of Pt/C and Pd@Pt/PVP/C.

Catalyst	ECDSA [m ² g-Pt ⁻¹]	MA@0.9V [A g-Pt ⁻¹]	SA@0.9V [μA cm ⁻²]
Pt/C ^{a)}	40	180	447
Pd@Pt/PVP/C ^{b)}	109	198	181

a): Pt/C is a commercial product. b): Pd@Pt/PVP/C was synthesized by the flow process. K₂PdCl₄: 5 mM, H₂PtCl₆: 2.5mM, NaBH₄: 8 mM (for Pd) and 4mM (for Pt), PVP: 0.1 wt%, Flow rate of K₂PdCl₄, H₂PtCl₆, NaBH₄, and PVP solution: 4 mL/min, Inner diameter of the mixers (M1-M4): 0.33 mm, Inner diameter of reactors (R1-R3): 1.0 mm, length: 50 mm, Reaction temperature: 25 °C. The obtained NPs were supported on carbon.

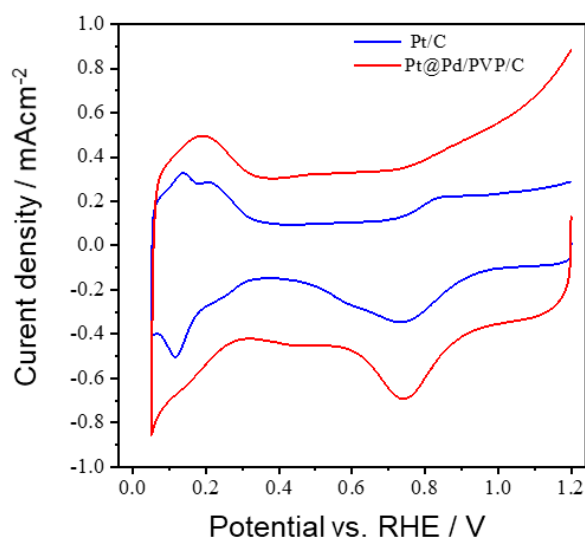


Figure 6. CVs of Pd@Pt/PVP/C synthesized by direct supporting flow process and commercial Pt/C in 0.1 M HClO₄ at a scan rate of 50 mVs⁻¹.

2.2.3. Pd@Pt core-shell synthesis by the direct-support method

It has been reported that metal NPs can be directly supported on activated carbon support without using polymer capping agents in a liquid-phase batch process.²⁴ That is, the metal precursor and the reducing agent are violently agitated in the presence of activated carbon to promote rapid adsorption of the formed metal NPs on to the carbon support. Therefore, I applied this method to my flow process.

A schematic diagram of the flow reactor used for the synthesis of Pd@Pt core-shell NPs by the direct-support method is shown in Figure 7. The PVP supply line, R4, and M4 were removed from the flow reactor shown in Figure 3. The synthesized NPs quickly come into contact with the carbon slurry

added to the receiving vessel. Details are described in the experimental section.

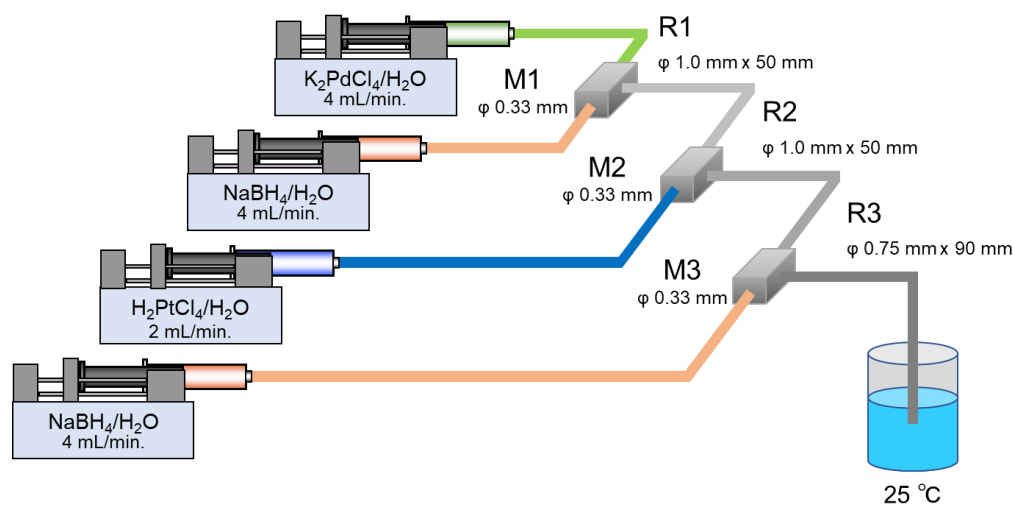


Figure 7. Schematic of the flow reactor used to synthesize Pd@Pt core-shell NPs by the direct-support method.

The DF-STEM image of the catalyst synthesized by the direct-support method is shown in Figure 8A. No significant metal NP agglomerates were observed, indicating that metal NPs could be supported on carbon without PVP by the direct-support method. From the TEM image, the average primary particle size was estimated to be 3.8 nm (Figure 9A), however, secondary particles were observed as indicated by the circle, in which approximately three particles were bound in the form of beads. I concluded that the formation of bead-like secondary particles was due to insufficient mixing in the flow system. Because this flow system could not improve the mixing of carbon support and generated NPs, the application of a capping agent that does not inhibit the ORR activity was investigated

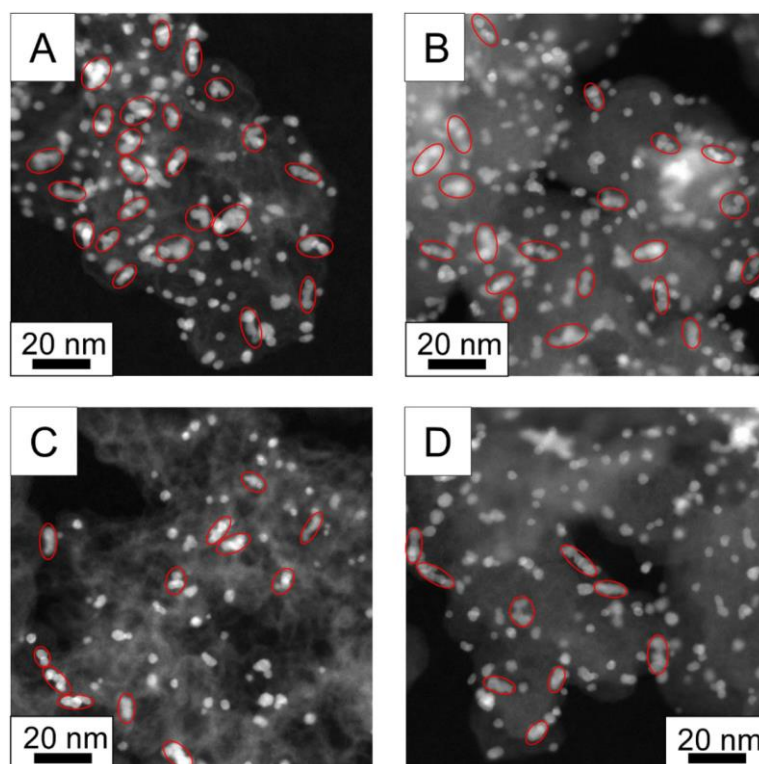


Figure 8. DF-STEM images of Pd@Pt/C synthesized by the direct-support flow process using A) none, B) DMF, C) IPA, and D) diglyme as a capping agent.

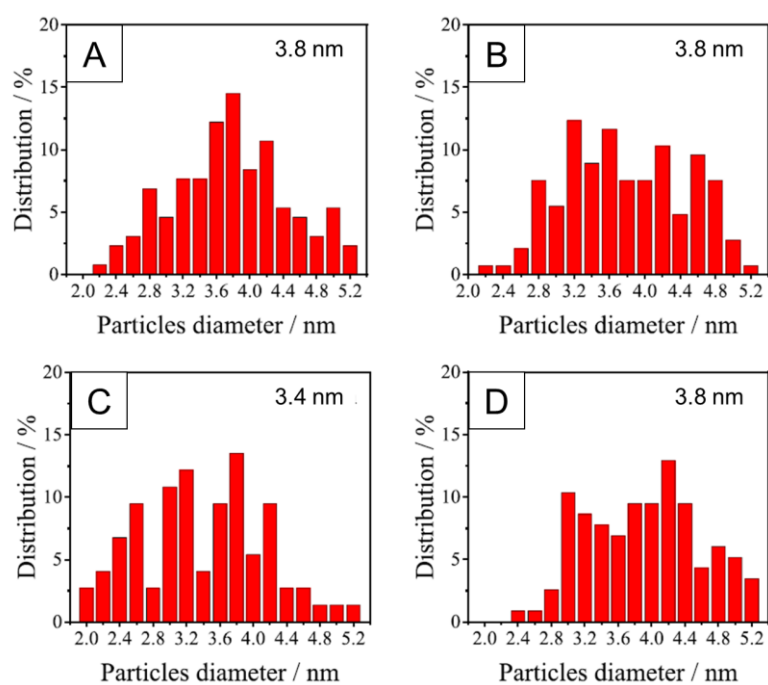


Figure 9. Size distributions of the Pd@Pt NPs synthesized by the direct-support flow process using A) none, B) DMF, C) IPA, and D) diglyme as a capping agent.

Coordination solvents, such as N,N-dimethylformamide (DMF) and methanol have been reported as potential capping agents for NPs.^{25,26} Alcoholic solvents, such as methanol and ethanol, may not inhibit reactions in the same manner as PVP because they are used in the dispersion of catalyst evaluations.²⁷ Ethers have also been used as coordination solvents. Thus, I investigated the additive effect of capping agents such as DMF, alcohols, and ethers on Pd@Pt core-shell NPs formation.

The results of the TEM analysis of the catalysts synthesized with different capping agents are shown in Figure 8. Various capping agents were added to the carbon slurry. Details are described in the experimental section. When DMF was used as a capping agent, the average particle size of the obtained primary particles was estimated to be 3.8 nm (Figure 9B). However, bead-like secondary particles were also observed (Figure 8B), similar to the results of the direct-support method without capping agent, suggesting that DMF had no effect as a capping agent. When methanol, ethanol, and isopropyl alcohol (IPA) were used as capping agents, only IPA was found to improve the dispersion of NPs. The average particle size of the obtained primary particles was 3.4 nm (Figure 9C), and a decrease in the formation of bead-like secondary particles was confirmed (Figure 8C). When bis(2-methoxyethyl) ether (diglyme), an ether-based solvent, was used, the number of bead-like secondary particles was further reduced as compared with the case where IPA was used. The average particle diameter of the obtained primary particles was 3.8 nm (Figure 9D). The size distribution of the primary particles using diglyme seems to be larger than that using none capping agent. However, as can be seen from the TEM images in Figure 8, the formation of bead-like secondary particles was clearly suppressed in the case of using diglyme as a capping agent. Therefore, a quantitative evaluation of the ratio of primary particles to secondary particles was performed. Then, I calculated the ratio of the average size of the primary particles (D) to the electrochemical Pt surface area (ECSA) of the particles (D/ECSA), where the D (nm) and the ECSA ($\text{m}^2 \text{g-Pt}^{-1}$) were estimated from the TEM image and the CV measurement, respectively. As a result, the D (nm)/ECSA ($\text{m}^2 \text{g-Pt}^{-1}$) values of the core-shell NPs synthesized using none, DMF, IPA, and diglyme as a capping agent were obtained to be 0.042, 0.040, 0.043, and 0.033, respectively. The aggregation inhibition effect of NP capping agents was thus shown to follow IPA < none < DMF < diglyme, clearly indicated that diglyme was most effective suppressed the growth of secondary particles. I believe that the characteristic required for the capping agent is the moderate adsorption behavior with the Pt surface without inhibiting the ORR.

The results of the EDS mapping images of NPs obtained using various capping agents are shown in Figure 10. The obtained primary particles possessed a Pd@Pt core-shell structure, regardless of the type of capping agent, clearly indicating that the capping agent did not participate in the formation of the core-shell structure of the primary particles, and only affected the dispersibility of the primary

particles.

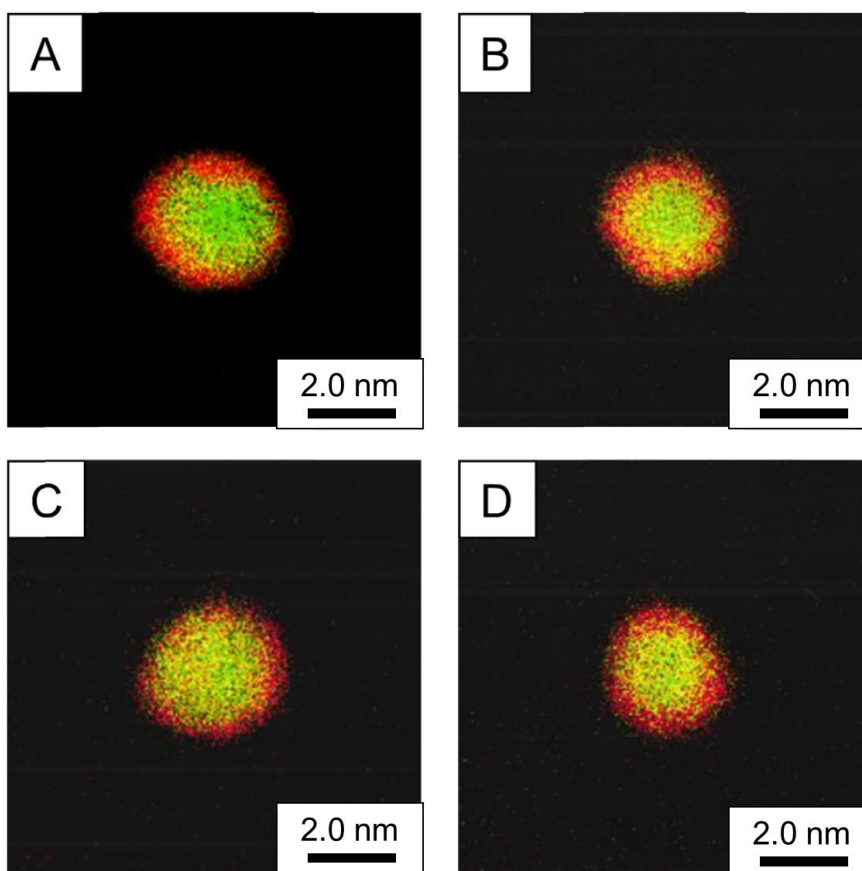


Figure 10. DF-STEM-EDS mapping image (Pd in green and Pt in red) of Pd@Pt/C synthesized by the direct-support flow process using A) none, B) DMF, C) IPA, or D) diglyme as a capping agent.

Next, I evaluated the ORR activities of the various catalysts. Figure 11 shows the CV wave forms and the activity evaluation results at 1600 rpm for each catalyst. For comparison, the results for Pt/C are also shown in Figure 11. For all Pd@Pt/C synthesized by the direct-support method using various capping agents, no peak separation was observed in the H_{upd} region of the CV waveform, similar to the CV waveform for Pd@Pt/PVP/C, confirming that the obtained NPs possessed a core-shell structure, even in CV analysis. From the results of the activity evaluation at 1600 rpm for each catalyst, the capping agents were confirmed to affect the ORR activity. The order of the effect of the capping agents on ORR activity was DMF < IPA < none < diglyme, in good agreement with the order of the aggregation inhibitory effect of the capping agents, except for DMF.

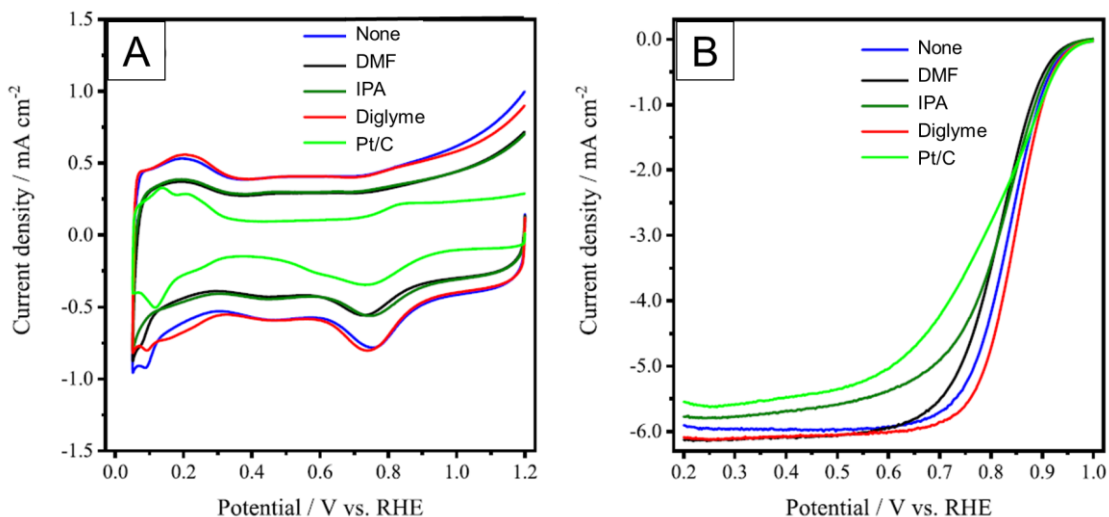


Figure 11. CVs of (A) Pt/C and Pd@Pt/C synthesized by the direct-support flow process using none, DMF, IPA, and diglyme as a capping agent in 0.1 M HClO₄ at a scan rate of 50 mV s⁻¹. ORR polarization curves (B) of the various catalysts in O₂-saturated 0.1 M HClO₄ at a scan rate of 10 mV s⁻¹ and rate of 1600 rpm.

The results of the ORR activity evaluation of the catalysts are shown in Table 6. In the case of no addition of a capping agent, the ECSA was 92 m² g-Pt⁻¹, slightly lower than 109 m² g-Pt⁻¹, the ECSA obtained for Pd@Pt/PVP/C (Table 5). The ECSA with DMF was almost the same as that with no capping agent, clearly indicating that DMF was ineffective as a capping agent; however, the ECSA value decreased when IPA was used.

TEM observations confirmed that the dispersibility of NPs was improved by using IPA as a capping agent. However, the results of the ECSA showed that the aggregation of NPs increased compared to the case without the addition of a capping agent. The ECSA value with diglyme was 112 m² g-Pt⁻¹, similar to 109 m² g-Pt⁻¹, the ECSA obtained for Pd@Pt/PVP/C (Table 5), suggesting that the NPs with ether were supported on the carbon with the same level of dispersibility as that with PVP.

Table 6. ORR activities of Pd@Pt/C synthesized by the direct-support flow process using capping agents.

Capping agent	ECSA [m ² g-Pt ⁻¹]	MA@0.9V [A g-Pt ⁻¹]	SA@0.9V [μA cm ⁻²]
None	92	278	302
DMF	95	194	204
IPA	79	249	316
Diglyme	112	332	297
Triethylene glycol dimethyl ether	85	235	277
Tetrahydrofuran	82	239	293

Pd@Pt/C was synthesized by the direct-support flow process. K₂PdCl₄: 5 mM, H₂PtCl₆: 2.5mM, NaBH₄: 8 mM (for Pd) and 4mM (for Pt), Flow rate of K₂PdCl₄, H₂PtCl₆, NaBH₄ solution: 4 mL/min, Capping agents (4 vol%) were added to ethanol in the carbon slurry, as necessary. Inner diameter of the mixers (M1-M4): 0.33 mm, Inner diameter of reactors (R1-R3): 1.0 mm, length: 50 mm, Reaction temperature: 25 °C.

The MA value without a capping agent was found to be 1.4 times higher than that of Pd@Pt/PVP/C. Similarly, the SA value was significantly improved compared with that of Pd@Pt/PVP/C, indicating that the inhibitory effect of PVP on the ORR activity was significant. The MA and SA values of Pd@Pt/C with DMF as a capping agent were similar to those of Pd@Pt/PVP/C, suggesting that DMF remained on the catalyst and inhibited the reaction in a similar manner as PVP. I believe that the amide structures in PVP and DMF may inhibit ORR activity on the Pt surface. When IPA was used as a capping agent, no significant differences in SA and MA values were observed compared with the case of without capping agent, indicating that alcohol did not inhibit the ORR activity. With the addition of diglyme, the MA value was approximately 1.7 and 1.8 times higher than those of Pd@Pt/PVP/C and Pt/C, respectively. Thus, diglyme performed excellently as a capping agent, maintaining a high dispersibility of NPs without inhibit the ORR activity. Therefore, triethylene glycol dimethyl ether and tetrahydrofuran were also studied, which have the same ether structure, as capping agents, but their ECSA and MA were lower than that of diglyme (Table 6). The underlying mechanism of why diglyme, but not the other ether-based solvents, improved the ECSA and MA values is currently unknown.

Thus, I succeeded in improving the dispersibility of core-shell NPs without inhibit with ORR activity by using diglyme, and synthesized Pd@Pt/C with higher activity than Pt/C. However, even the core-shell catalyst synthesized by the direct-support method using diglyme, which had the highest activity, was inferior to the ORR activity of the Cu-UPD synthesis catalyst. Therefore, further optimization of flow synthesis conditions is needed.

2.3. Conclusion

I have investigated a flow manufacturing process for the synthesis of Pd@Pt core-shell catalysts with high productivity and exact structural control. However, the ORR activity of the Pd@Pt/PVP/C catalyst was found to be significantly lower than that of commercial Pt/C catalysts. This is due to inhibition of the remaining PVP. To synthesize Pd@Pt without capping agents that inhibit the ORR reaction, I explored the characteristics of the flow reactor for Pd@Pt core-shell NPs synthesis. Furthermore, I have demonstrated that Pd@Pt NPs can be uniformly dispersed on activated carbon by adding diglyme as a capping agent. Particle size and core-shell particle size and core-shell structure of Pd@Pt NPs did not differ significantly depending on the capping agent such as PVP or diglyme. This indicates that a high degree of structural control is possible even without PVP. Furthermore, the ORR activity of Pd@Pt/diglyme/C with diglyme was found to be 1.7 times higher than that of Pd@Pt/PVP/C. I demonstrated that Pd@Pt core-shell NPs with precisely controlled structure and high ORR activity can be synthesized by a flow process. Due to the high productivity, the relative low-cost, and the simplicity, this flow synthesis technique by combining a continuous stream of the suspended activated carbon support should be highly appealing for the industrial production of the Pd@Pt/C catalyst. However, the ORR activity of the core-shell catalyst synthesized by this flow process was inferior to that of the Cu-UPD synthesized catalyst. Henceforth, further improve the ORR activity in the future, it is necessary to develop a synthesis method to control the core-shell structure more precisely. Nevertheless, I have demonstrated that the flow process is an effective method for the synthesis of core-shell catalysts that can achieve continuity, productivity, and scalability.

2.4. Experimental

2.4.1. Chemicals and materials

All chemicals were commercial products and used without further purification. K_2PdCl_4 (99.99%) and $H_2PtCl_6 \cdot 6H_2O$ ($\geq 37.50\%$ Pt basis) were purchased from Sigma-Aldrich. $NaBH_4$, PVP K30, DMF, IPA, ethanol, diglyme, 5 wt% Nafion solution, and 60% $HClO_4$ were purchased from Fujifilm Wako Pure Chemical Corporation. Pt/C was purchased from Ishifuku Metal Industry Co., Ltd. Carbon ECP was purchased from Lion Specialty Chemicals Co., Ltd. All aqueous solutions were prepared using highly purified deionized water with a resistivity of 18.2 M Ω cm.

2.4.2. Synthesis of Pd/PVP NPs by the flow process

The synthesis of Pd/PVP NPs was performed using the flow process shown in Figure 2. The mixers (M1 and M2) were constructed using SUS-316 union tees with different inner diameters (Swagelok®, SS-1F0-3GC, I.D. = 0.15–2.0 mm). PEEK tubes of different lengths (I.D. = 1 mm, length = 15–100 mm) were connected between the mixers and used as reactors. A syringe pump (Harvard Apparatus PHD Ultra XF, PHD Ultra 4400) was used as the liquid delivery pump. The syringes used for the Pd precursor and PVP solutions were SUS316 syringes (Harvard Apparatus). Glass syringes (SGE) were used for the reductant.

K_2PdCl_4 (163 mg) was dissolved in H_2O in a 100 mL flask to prepare a 5 mM Pd solution, and then transferred to syringe pump A. $NaBH_4$ (3.8–76 mg) was dissolved in H_2O in a 25 mL flask to prepare a 4–80 mM reducing agent solution, and transferred to syringe pump B. PVP K30 (250–5000 mg) was dissolved in H_2O in a 1000 mL flask to prepare the capping agent solution with various concentrations, and transferred to syringe pump C. Each solution was pumped at a flow rate of 4 mL/min.

The resulting NPs were collected at the outlet of the flow reactor and washed three times with an ultrafiltration filter (Sartorius VIVASPIN 20 MWCO 3000). The concentration of the unreacted metals precursor in the filtrate was measured by inductively coupled plasma atomic emission spectroscopy (ICP–AES, Shimadzu ICPE-9800), however, no metal species were detected.

2.4.3. Synthesis of Pd@Pt/PVP/C NPs catalyst by the flow process

The synthesis of Pd@Pt NPs was carried out using the flow reactor shown in Figure 3. The mixers (M1–M4) employed a SUS-316 union tee (Swagelok®, SS 1F0-3GC, I.D. = 0.33 mm). Either SUS-316 or PEEK tubes (I.D. = 1 mm, length = 50 mm) were connected between the mixers. The same syringe pump, as for preparation Pd/PVP NPs, was used as the liquid delivery pump. The syringes

used for the metal precursors and PVP were SUS316 syringes. A glass syringe was used for the reductant.

K_2PdCl_4 (163 mg) was dissolved in H_2O in a 100 mL flask to prepare a 5 mM Pd solution, and transferred to syringe pump A. $NaBH_4$ (7.6 mg) was dissolved in H_2O in a 25 mL flask to prepare an 8 mM reducing agent solution, and transferred to syringe pump B. $H_2PtCl_6 \cdot 6 H_2O$ (130 mg) was dissolved in H_2O in a 100 mL flask to prepare a 2.5 mM Pt solution, and transferred to syringe pump C. $NaBH_4$ (3.8 mg) was dissolved in H_2O in a 25 mL flask to prepare a 4 mM reducing agent solution, and transferred to syringe pump D. PVP K30 (500 mg) was dissolved in H_2O in a 500 mL flask to prepare a 0.1 wt% capping agent solution, and transferred to syringe pump E. Each solution was pumped and mixed at a flow rate of 4 mL/min. The recovery of the obtained NPs and measurement of the metal concentration in the filtrate were performed in the same manner as the synthesis of Pd/PVP NPs.

The Pd@Pt/PVP/C catalyst was prepared with a 5 wt% total loading of Pd and Pt. A concentrated and purified solution containing a predetermined amount of Pd@Pt/PVP NPs was added to a suspension of Carbon ECP and ethanol. The mixture was stirred at 25 °C for 18 h. The resultant Pd@Pt/PVP/C was filtered by Kiriya filtration and dried at 40 °C for 4 h under vacuum. ICP–AES analysis of the filtrate showed that all metals were loaded on the Carbon ECP.

2.4.4. Synthesis of Pd@Pt/C by the direct-support method

The synthesis of Pd@Pt NPs by the direct-support method was carried out using the flow reactor shown in Figure 7. The concentrations of the raw materials and feed rates were the same as those for the synthesis of Pd@Pt/PVP NPs using the flow process. The synthesized NPs discharged from the flow reactor were directly added to a carbon slurry. The carbon slurry was prepared by adding Carbon ECP, such that the total Pd and Pt loading was 5 wt%, to 85 mL of ethanol with stirring using a magnetic bar at 300 rpm. To prevent the aggregation of the synthesized NPs, capping agents (4 vol%) were added to ethanol in the carbon slurry, as necessary. The NP and carbon mixture was stirred at 25 °C for 15 min. The resultant Pd@Pt/C catalysts were filtered by Kiriya filtration and dried at 40 °C for 4 h under vacuum. ICP–AES analysis of the filtrate showed that all metals were loaded on the Carbon ECP.

2.4.5. Characterization of catalyst

2.4.5.1. TEM / EDS / EELS

All analyses were performed at the UBE Scientific Analysis Laboratory. DF-STEM and DF-STEM-EDS mapping images were obtained using a JEOL JEM-ARM200F operating at 60 kV with an EDS attachment. DF-STEM–EELS images were obtained using a JEOL JEM-2100 F operating at 120 kV and a beam size of > 0.07 nm with a Gatan ENFINA 1000 attachment. The sample was prepared by depositing the deionized ethanol-dispersed catalyst on a copper grid, followed by evaporation of ethanol. The size distributions of Pd@Pt NPs were determined by counting about 200 particles from DF-STEM images.

2.4.5.2. SAXS measurement

SAXS measurements were carried out with a Bruker D8 Discover diffractometer, with a Cu microfocus X-ray source ($\lambda = 15.4184$ nm) and a 2-dimensional Vantec-500 detector. The sample was injected into a glass capillary tube and mounted in a capillary sample holder. The measurement was performed in transmission mode with an exposure time of 600 s. The data analysis was performed using the Diffrac. Suite SAXS software (Bruker).

2.4.5.3. Electrochemical measurements

Electrochemical experiments were carried out in a three-electrode cell at 25 °C using a BAS ALS-760E electrochemical workstation with a BAS RRDE-3A rotation system. A Pt wire and reversible hydrogen electrode were used as the counter electrode and reference electrode, respectively. The electrolyte used was 0.1 M HClO₄, prepared by diluting a 60% stock solution with H₂O. The catalyst ink was prepared by dispersing 20 mg of catalyst powder in a mixture of 2.5 mL of H₂O, 2.5 mL of IPA, and 45 μ L of 5% Nafion by sonication. A 6.5 μ L aliquot of the catalyst ink was drop-cast on a glassy carbon working electrode (GCE) with a diameter of 5 mm and dried at room temperature under ambient conditions. Before drop casting, the GCE was polished successively with 1 μ m diamond paste and 0.05 μ m alumina paste (BAS). The amount of Pt loaded on the GCE was estimated to be 3.1 μ g Pt cm⁻².

The CV curve was recorded over the potential range 0.05–1.2 V at a scanning rate of 50 mV s⁻¹ in a 0.1 M HClO₄ aqueous solution purged for 30 min with Ar gas prior to use. We calculated the electrochemical Pt surface area (ECSA) of each catalyst on the basis of the charges associated with the adsorption of hydrogen in the region 0.05–0.4 V after a double-layer correction with a reference value of 210 μ C cm⁻² for the adsorption of a monolayer of hydrogen from the Pt surfaces. The rotating

disk electrode experiments were performed in the potential range 0.05–1.0 V at a scanning rate of 10 mV s⁻¹ in a 0.1 M HClO₄ aqueous solution purged for 30 min with O₂ gas prior to use. The ORR polarization curves measured at various rotational speeds (400–3600 rpm) were used to estimate the kinetic current I_k from the Koutecký-Levich (KL) plot. The KL plot was obtained by Equation (1).

$$I^{-1} = I_k^{-1} + I_d^{-1} = I_k^{-1} + (B\omega^{1/2})^{-1} \quad (1)$$

Where I is the experimentally measured current, I_d is the diffusion-limited current, and ω is the angular frequency of rotation. The B parameter is defined as in Equation (2).

$$B = 0.62nFAcD^{2/3}\nu^{-1/6} \quad (2)$$

Where F is the Faraday constant, A is the disk electrode geometric area, c is the concentration of O₂ in the electrolyte, D is the diffusion coefficient of O₂, and ν is the viscosity of the electrolyte. KL plots were generated using data obtained from the RDE experiments (Figure 12). The I_k for ORR can be determined from the intercept of the I^{-1} axis at $\omega^{1/2} = 0$ and potential of 0.9 V.

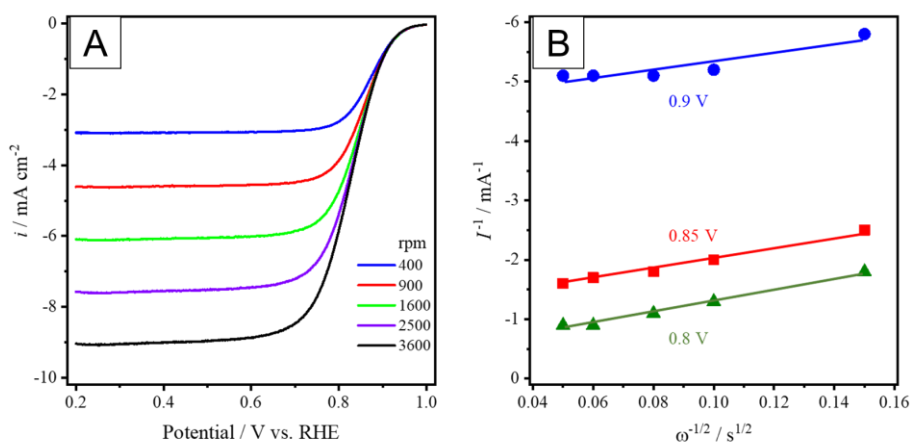


Figure 12. ORR polarization curves (A) of Pd@Pt/C synthesized by direct supporting flow process using diglyme in 0.1 M HClO₄ at a scan rate of 10 mVs⁻¹. Koutecký-Levich plot (B) at different potentials using the data obtained from (A).

2.5. References

- [1] R. Jiang, S. O. Tung, Z. Tang, L. Li, L. Ding, X. Xi, Y. Liu, L. Zhang, J. Zhang, *Energy Stor. Mater.* **2018**, *12*, 260–276.
- [2] R. R. Adzic, J. Zhang, K. Sasaki, M. B. Vukmirovic, M. Shao, J. X. Wang, A. U. Nilekar, M. Mavrikakis, J.A. Valerio, F. Uribe, *Top. Catal.* **2007**, *46*, 249–262.
- [3] K. Sasaki, H. Naohara, Y.-M. Choi, Y. Cai, W.-F. Chen, P. Liu, R. R. Adzic, *Nat. Commun.* **2012**, *3*, 1–9
- [4] K. Gong, Y.-M. Choi, M. B. Vukmirovic, P. Liu, C. Ma, D. Su, R. R. Adzic, *Z. Phys. Chem.* **2012**, *226*, 1025–1038.
- [5] K. Cao, Q. Zhu, B. Shan, R. Chen, *Sci. Rep.* **2015**, *5*, 8470.
- [6] V. R. Manikam, K. Y. Cheong, K. A. Razak, *Mater. Sci. Eng. B* **2011**, *176*, 187–203.
- [7] D. C. Trinh, T. M. D. Dang, K. K. Huynh, E. Fribourg-Blanc, M. C. Dang, *Adv. Nat. Sci. Nanosci. Nanotechnol.* **2015**, *6*, 025018.
- [8] X. Wang, Y. Orikasa, Y. Takesue, H. Inoue, M. Nakamura, T. Minato, N. Hoshi, Y. Uchimoto, *J. Am. Chem. Soc.* **2013**, *135*, 5938–5941.
- [9] V. Stamenkovic, B. S. Mun, K. J. J. Mayrhofer, P. N. Ross, N. M. Markovic, J. Rossmeisl, J. Greeley, J. K. Nørskov, *Angew. Chem. Int. Ed.* **2006**, *45*, 2897–2901.
- [10] T. Doi, M. Inaba, K. Higashi, T. Uruga, Y. Iwasawa, H. Tanida, Q. Yuan, N. Takao, H. Imai, T. Mikami, A. Daimaru, *J. Electrochem. Soc.* **2020**, *167*, 044513.
- [11] Y. Song, J. Hormes, C. S. S. R. Kumar, *small* **2008**, *4*, 698–711.
- [12] G. Tofighi, H. Lichtenberg, J. Pesek, T. L. Sheppard, W. Wang, L. Schöttner, G. Rinke, R. Dittmeyer, J.-D. Grunwaldt, *React. Chem. Eng.* **2017**, *2*, 876–884.
- [13] M. Solsona, J. C. Vollenbroek, C. B. M. Tregouet, A.-E. Nieuwelink, W. Olthuis, A. van den Berg, B. M. Weckhuysen, M. Odijk, *Lab Chip* **2019**, *19*, 3575–3601.
- [14] M. T. Rahman, E. V. Rebrov, *Processes* **2014**, *2*, 466–493.
- [15] A. Pekkari, Z. Say, A. Susarrey-Arce, C. Langhammer, H. Haerelind, V. Sebastian, K. Moth-Poulsen, *ACS Appl. Mater. Interfaces* **2019**, *11*, 36196–36204.
- [16] J. Shen, M. Shafiq, M. Ma, H. Chen, *Nanomaterials* **2020**, *10*, 1177.
- [17] C. J. Kiely, G. J. Hutchings, *Nanoscale* **2019**, *11*, 8247–8259.
- [18] I. A. Safo, C. Dosche, M. Ozaslan, *Phys. Chem. Chem. Phys.* **2019**, *20*, 3010–3023.
- [19] D. F. Vliet, C. Wang, D. Li, A. P. Paulikas, J. Greeley, R. B. Rankin, D. Strmcnik, D. Tripkovic, N. M. Markovic, V. R. Stamenkovic, *Angew. Chem. Int. Ed.* **2012**, *51*, 3139–3142.
- [20] Y.-N. Wu, S.-J. Liao, Z.-X. Liang, L.-J. Yang, R.-F. Wang, *J. Power Sources* **2009**, *194*, 805–810.

- [21] K. Sasaki, J. X. Wang, H. Naohara, N. Marinkovic, K. More, H. Inada, R. R. Adzic, *Electrochim. Acta* **2010**, *55*, 2645–2652.
- [22] M. Shao, Q. Chang, J.-P. Dodelet, R. Chenitz, *Chem. Rev.* **2016**, *116*, 3594–3657.
- [23] G. Zhang, Z.-G. Shao, W. Lu, F. Xie, H. Xiao, X. Qin, B. Yi, *Appl. Catal. B* **2013**, *132–133*, 183–194.
- [24] J. Zhang, X. Wang, C. Wu, H. Wang, B. Yi, H. Zhang, *React. Kinet. Catal. Lett.* **2004**, *83*, 229–236.
- [25] Q.-L. Zhu, N. Tsumori, Q. Xu, *J. Am. Chem. Soc.* **2015**, *137*, 11743–11748.
- [26] H. Kawasaki, H. Yamamoto, H. Fujimori, R. Arakawa, M. Inada, Y. Iwasaki, *Chem. Commun.* **2010**, *46*, 3759–3761.

**Chapter 3. Flow Synthesis Process for Pd@Pt Core-Shell Catalysts
with Highly Controlled Pt Shell Thickness**

3.1. Introduction

In Chapter 2, I found that Pd@Pt core-shell catalysts could be synthesized with high productivity by the flow method. However, the activity of the obtained catalysts was lower than that of the catalysts synthesized by the Cu-UPD method.¹ Since the local structure by TEM-EDS showed a core-shell structure, I thought that there might be a problem with the average structure and decided to perform X-ray absorption fine structure (XAFS) measurement, which can obtain average information. XAFS is an analytical technique that enables element-selective evaluation of valence and local structure (coordination number, bond distance) by measuring and analyzing the X-ray absorption spectrum (XAFS spectrum) of a sample. This method has been widely used for structural analysis of catalysts for fuel cells. For example, Adzic et al. calculated the Pt–Pt and P–Pd coordination numbers from XAFS measurements of Pd@Pt catalysts synthesized by the Cu-UPD method and reported that the synthesized catalysts have a 1 ML Pt shell even as an average structure.²

This analysis identified the cause of the low activity of the flow-synthesized Pd@Pt catalyst and led to further optimization of the process conditions with the aim of establishing a flow synthesis method for core-shell catalysts with a structure and activity comparable to existing methods.

By the way, the process conditions to be considered in the flow synthesis of Pd@Pt core-shell catalysts are diverse and require much time for optimization. For example, the types of metal precursors, reactants, and additives, mixing efficiency of reaction solutions, residence time, and temperature. In recent years, attention has been focused on accelerating the development of materials using high-throughput synthesis systems, and many examples have been reported for catalyst and nanoparticle synthesis. For example, Shinke and Fujitani et al. reported the development of highly active heterogeneous catalysts for 1,3-butadiene synthesis by utilizing a high-throughput synthesis systems.³ Kashiwagi and Takebayashi et al. reported the development of AgNPs for optical materials utilizing a batch-type high-throughput synthesis systems.⁴ Therefore, I also developed a new high-throughput flow synthesis system for core-shell synthesis, shown in Figure 1, based on these examples, and used it for condition optimization.

The high-throughput flow synthesis system is outlined below. First, Pd@Pt NPs are synthesized by pumping any metal feedstock and reducing agent into the reactor by means of an autosampler and a feed pump. The resulting Pd@Pt catalyst is collected and stored in specific sample tubes by fraction collectors. A control PC performs all of these operations automatically and continuously. The number of catalysts synthesized per day can be increased from 4 to 20 by using this system.

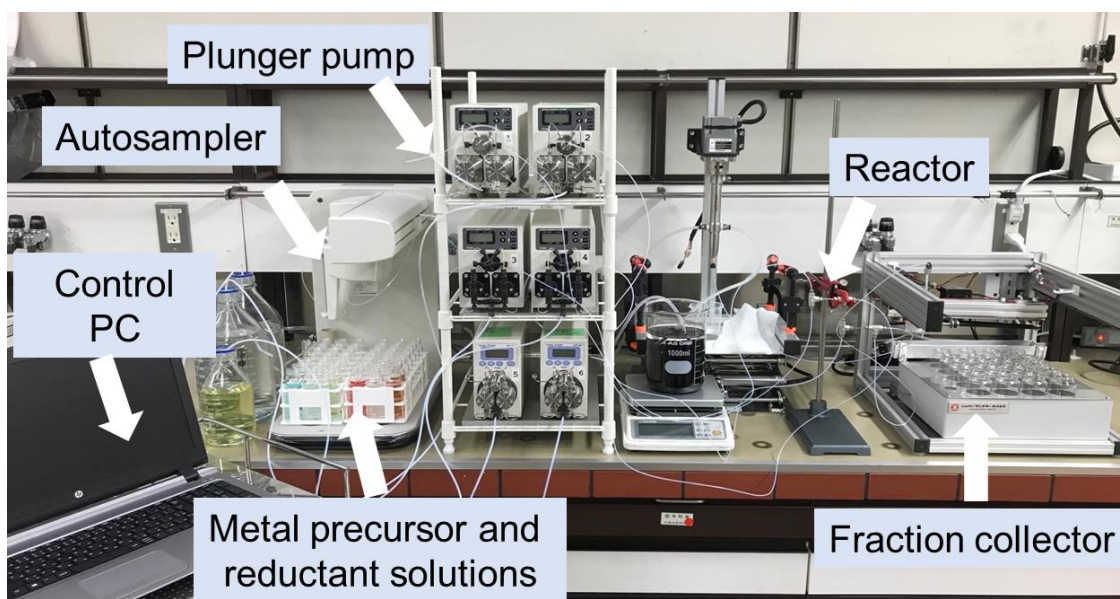


Figure 1. High-throughput flow synthesis system for core-shell catalysts synthesis.

In this chapter, I first identified the cause of the low activity of flow-synthesized Pd@Pt catalysts by XAFS. Next, based on the findings obtained here, I developed a flow synthesis method for Pd@Pt with activity and structure comparable to those of Cu-UPD synthesis catalysts by rapidly optimizing the process conditions using a high-throughput flow synthesis system.

3.2. Results and Discussion

3.2.1. Structural analysis of Pd@Pt/C by XAFS

In Chapter 2, I reported that diglyme was found to be an excellent capping agent in the synthesis of Pd@Pt/C catalysts by the direct-support method, but the ORR activity was lower than catalysts prepared by Cu-UPD. Therefore, as mentioned in the introduction, to elucidate the reason for the low ORR activity of Pd@Pt/C prepared by the flow process, I investigated the structure of Pd@Pt/C using XAFS measurement. Figure 2 shows the X-ray Absorption Near Edge Structure (XANES) and X-ray absorption fine structure (EXAFS) k -space spectra for Pd@Pt/PVP/C (Cat. 1) and the diglyme (as the capping agent) added catalyst displaying the highest ORR activity produced by the direct-support method (Pd@Pt/diglyme/C, Cat. 2). The results for Pt foil are also shown for comparison. Cat. 1 and Cat. 2 exhibited similar XANES and EXAFS k -space spectra, indicating that both catalysts possessed the same structure; the core-shell structure revealed by TEM. Specially, the XANES spectra of both Cat. 1 and Cat. 2 agreed with that of Pt foil, indicating that the Pt in both core-shell catalysts was predominantly metallic. X-ray photoelectron spectroscopy (XPS) results for Pd@Pt synthesized by

the direct-support flow process with various capping agents are shown in Figure 3. The results obtained from XANES are consistent with XPS results.

On the other hand, the amplitudes of the k -space EXAFS oscillations at each absorption edge were smaller than those of bulk Pt, which was attributed to the finite size effect of NPs.⁵ It was thus shown that the coordination number of Pt–Pt was decreased, strongly suggesting that Cat. 1 and Cat. 2 possessed a core-shell structure with a thin film of Pt. The oscillations of EXAFS for the Pd@Pt core-shell NPs phase shift to a slightly higher k value at the Pt edge, implying that the core is formed from Pd metal and the Pt shell somewhat distorted.⁶

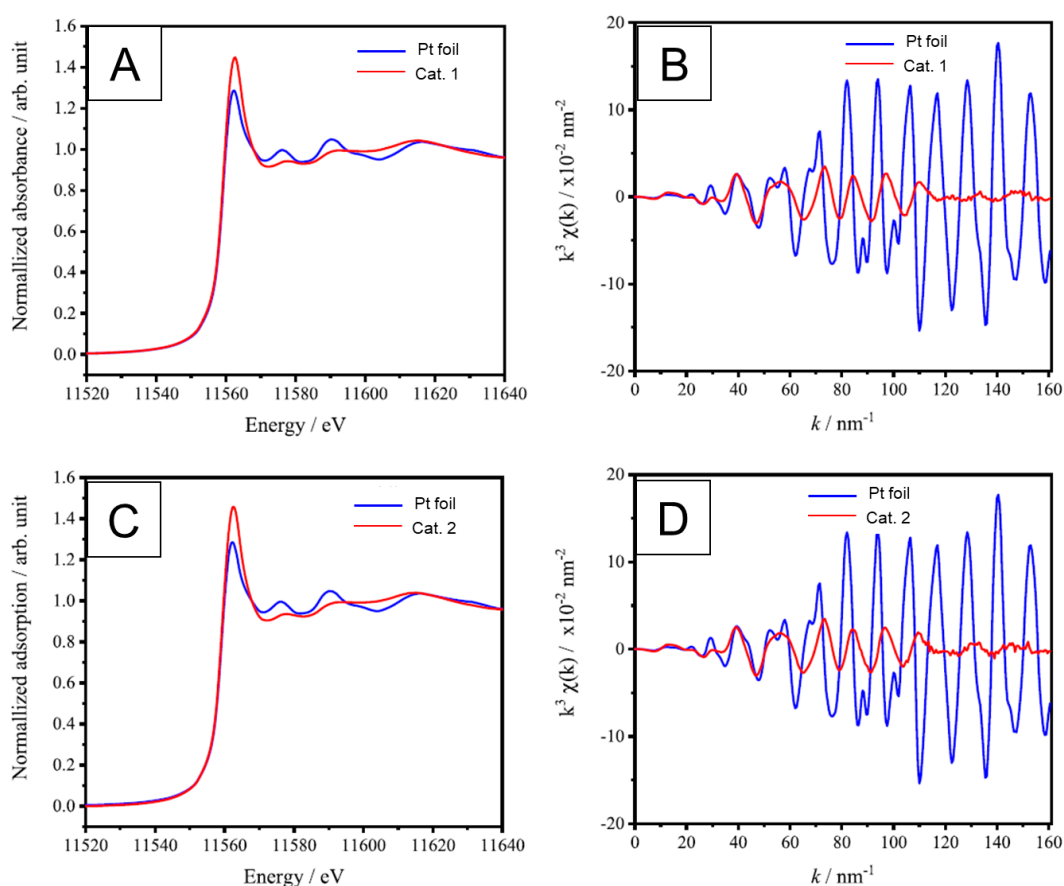


Figure 2. A) XANES and B) EXAFS k -space spectra (k^3 -weighted) of Pt L₃ obtained from Cat. 1, and C) XANES and D) EXAFS k -space spectra (k^3 -weighted) of Pt L₃ obtained from Cat. 2, together with those from a reference Pt foil.

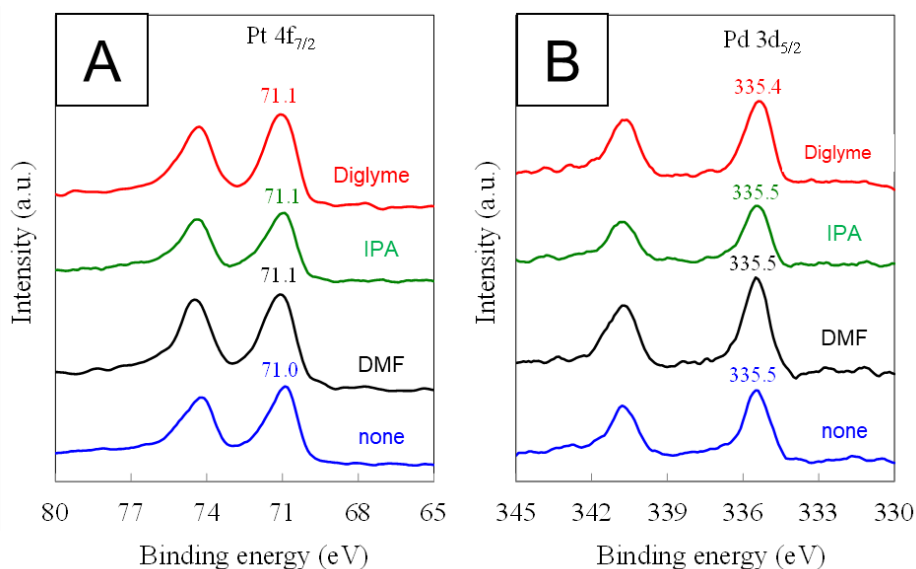


Figure 3. XP spectra of Pt 4f (A) and Pd 3d (B) for Pd@Pt/C synthesized by the direct-support flow process using none, DMF, IPA, and diglyme as the capping agents.

EXAFS data and theoretical fits for the Pt L_{3} edge of the Cat. 1 and Cat.2 are shown in Figure 4. I analyzed the EXAFS data by fitting the Pt edge data in consideration of homometallic (Pt–Pt and Pd–Pd) and heterometallic (Pt–Pd and Pd–Pt) interactions. I summarize the best fit values of the first nearest neighbor structure parameters in Table 1 and Table 16 in experimental section. From the best fitting results, the approximations used in the fit were validated by good fit quality and physically meaningful values. These fitting results estimated the Pt–Pt and Pt–Pd coordination numbers for both catalysts to be approximately 5 and 2, respectively. A Pt–Pt coordination number of 6 and Pt–Pd coordination number of 3 have been reported for core-shell particles with a particle size of 3.5 nm and a one-layer thick Pt shell.⁷⁻⁹ Both the Pt–Pt and Pt–Pd coordination numbers of the flow-synthesized Pd@Pt catalyst are smaller than those reported for the 1 ML Pt shell catalyst. In contrast, the Pt shell thickness was approximately two atomic layers based on the results from the EELS analysis described in the previous section. The structure of the flow-synthesized Pd@Pt catalyst expected from these facts is shown in Figure 5. It is expected that the flow-synthesized Pd@Pt catalyst contains not only areas where 1 ML of Pt shell are formed, but also areas that are not covered by Pt and areas where more than 2 ML of Pt shell are formed. Cat. 5 with a uniform 1 ML Pt shell synthesized by Cu-UPD shows high ORR activity. Therefore, the heterogeneous Pt shell structure could be the reason for the lower ORR activity of the flow-synthesized core-shell catalysts compared to the Cu-UPD catalysts.

For example, in the case of the 2ML Pt shell, the activity per Pt weight is expected to be lower due to the presence of Pt not involved in the reaction. Indeed, Adzic et al. reported that Pd@Pt_{2ML}

catalysts have inferior MA compared to Pd@Pt1ML.² The presence of Pt atoms with a low Pt-Pt coordination number of less than 6, i.e., deficient Pt shells, is also considered to be responsible for the lower activity.^{10,11} Therefore, uniform 1 ML shell formation without defects is necessary to obtain a catalyst with activity comparable to the existing method. Thus, I next decided to examine the synthesis conditions for the Pt shell formation stage.

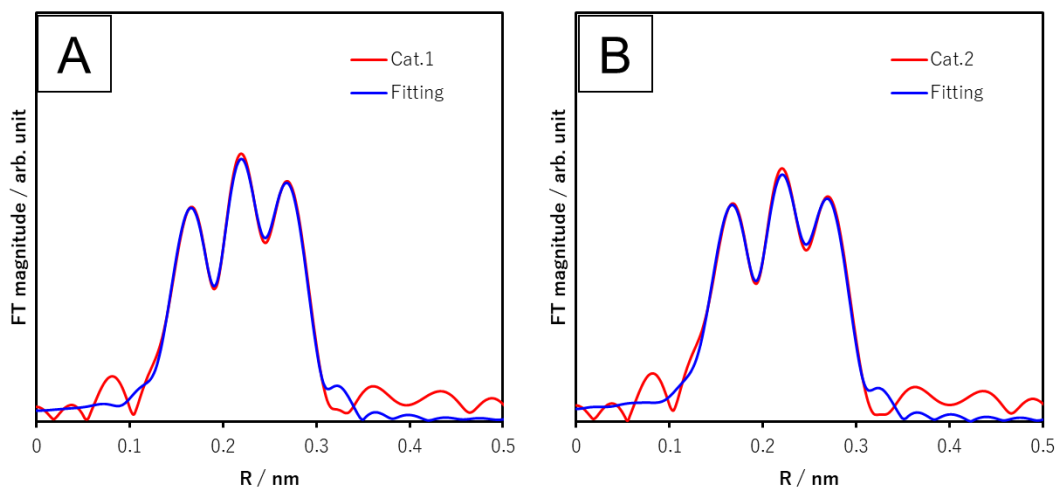


Figure 4. Fourier transform of the data (red lines) and first-shell fit (blue line) of A) Pt L₃ edges from Cat. 1, and B) Pt L₃ edges from Cat. 2.

Table 1. Activity and coordination number of core-shell catalysts synthesized by flow and Cu-UPD methods.

Cat.	Method	N _{Pt-Pt}	N _{Pt-Pd}	MA@0.9V [A g-Pt ⁻¹]
1 ^{a)}	Flow	5.0	2.0	198
2 ^{b)}	Flow (direct-support)	4.7	1.7	332
3 ^{c)}	Cu-UPD	5.8	2.7	570

a): Pd@Pt/PVP/C reported in Chapter 2 which was synthesized by the flow process.
 b): Pd@Pt/diglyme/C reported in Chapter 2 which was synthesized by the direct-support flow process. c): Literature values for catalysts synthesized by Cu-UPD method²

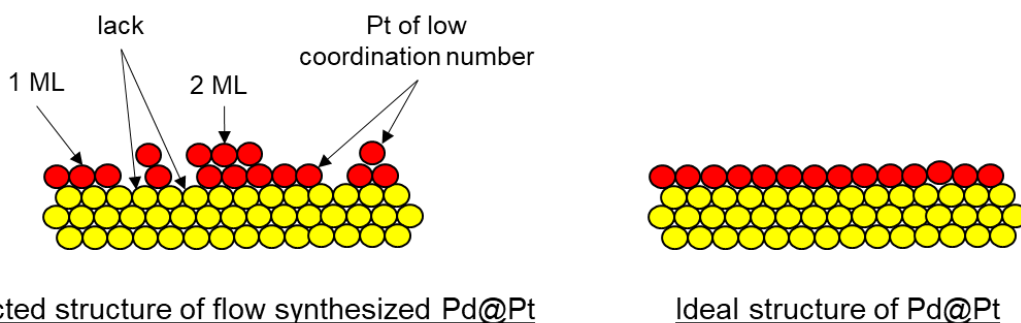


Figure 5. Predicted and ideal structures of flow-synthesized Pd@Pt

3.2.2. Effect of Pt precursors and reductants on the Pt shell structure and catalytic properties of Pd@Pt core-shell particles

First, I utilized a high-throughput flow synthesis system to examine various process conditions for the Pt shell formation stage. As a result of XAFS measurement of the obtained catalysts, no significant change in the obtained spectra was confirmed by changing the conditions such as mixing efficiency of the reaction solution, residence time, and reactant concentration. In other words, these conditions did not affect the Pt shell structure. Since it was found that the type of Pt precursor and reductant for Pt had a particularly large effect on the Pt shell structure, we decided to study these conditions in more detail.

First, the reductant for Pt was fixed to NaBH_4 to study the effect of the Pt precursor on the Pt shell structure and catalytic activity. The activity of each catalyst and the Pt–Pt and Pt–Pd coordination numbers obtained from the results of the fitting analysis of the EXAFS spectra shown in Figure 6 (Table 17 in the experimental section) are shown in Table 2. In Chapter 2, I reported that diglyme improves the dispersion of Pd@Pt NPs without inhibiting ORR activity.¹ Therefore, diglyme, which was effective in dispersing nanoparticles, was also added to the activated carbon slurry in this study. In the case of K_2PtCl_6 (Cat. 4), which is the same tetravalent Pt precursor as the previously used H_2PtCl_6 , the Pt–Pt and Pt–Pd coordination numbers were found to be almost identical to those obtained when H_2PtCl_6 was used (Cat. 2). This value is considerably lower than the theoretical value for 1 ML ($N_{\text{Pt-Pt}} : 6, N_{\text{Pt-Pd}} : 3$). This indicates that there are some areas where the Pd core particles are not partially covered by the Pt shell,¹ and that core-shell particles with uniform Pt shell thickness have not been obtained. Therefore, the ORR activity is only half that of the core-shell catalyst prepared by the Cu-UPD method.

Next, the effect of the reducing agent was examined using H_2PtCl_6 as the Pt precursor (Cat. 5, 6). The borane complex 2-methylpyridine· BH_3 (2-MePy· BH_3) and $\text{NaBH}(\text{OAc})_3$, in which the three H's of NaBH_4 were replaced by acetoxy groups, were used as reducing agents. I consider the following ordinal order of strength as a reducing agent.¹²



The results of the fitting analysis of the EXAFS spectra of the catalysts with 2-MePy· BH_3 as reductant are shown in Figure 6B. The Pt–Pt and Pt–Pd coordination numbers were estimated to be 6.8 and 2.4, respectively. This is close to the theoretical value of $\text{Pt}_{1\text{ML}}$ and may be due to the formation of core-shell particles with a controlled structure similar to a $\text{Pt}_{1\text{ML}}$ shell. Although the reducing power of 2-MePy· BH_3 is said to be weaker than that of NaBH_4 , it is not possible to say at this time whether the reducing power of the reductant has any effect on the Pt shell formation. However, the ECSA and ORR activities do not differ much from those of catalysts with heterogeneous Pt shell structure using NaBH_4 as reductant (Cat. 2, 4). The reasons for the lower Pt surface area and ORR activity despite the $\text{Pt}_{1\text{ML}}$ shell structure are discussed in detail in the next section. The results of the fitting analysis of the EXAFS spectra of the catalysts with $\text{NaBH}(\text{OAc})_3$, the least reductive agent as reductant are shown in Figure 6C. From the analysis, the Pt–Pt and Pt–Pd coordination numbers were estimated to be 5.0 and 1.9, respectively. The ECSA and ORR activities are also not significantly different from those of NaBH_4 as reducing agent. Although the reducing power of $\text{NaBH}(\text{OAc})_3$ is weaker than that of NaBH_4 and the reduction rate of Pt precursor may be the slowest, it is unlikely that the reduction rate of Pt precursor affects the formation of Pt shell structure, since the Pt shell structure is almost unchanged from that of NaBH_4 . The above results indicate that the Pt shell structure of core-shell particles is hardly affected by the reduction rate of the Pt precursor, but the use of 2-MePy· BH_3 reducing agent allows the formation of a single layer of Pt shell. The reason for this is discussed below.

Table 2. Effect of Pt precursors and reductants on the Pt shell structure and catalytic properties of Pt@Pd core-shell particles^a.

Cat.	Pt precursor	Reductant	N _{Pt-Pt}	N _{Pt-Pd}	ECSA [m ² g-Pt ⁻¹]	MA@0.9V [A g-Pt ⁻¹]	SA@0.9V [μA cm ⁻²]
2 ^b)	H ₂ PtCl ₆	NaBH ₄	4.7	1.7	112	332	297
4	K ₂ PtCl ₆	NaBH ₄	4.3	2.0	110	307	281
5	H ₂ PtCl ₆	2-MePy·BH ₃	6.8	2.5	84	340	403
6	H ₂ PtCl ₆	NaBH(OAc) ₃	5.0	1.9	108	313	291

a): Pd@Pt/C was synthesized by the direct-support flow process. K₂PdCl₄: 5 mM, Pt precursor: 2.5mM, NaBH₄: 8 mM (for Pd), Reductant 4~16mM (for Pt). The amount of reducing agent used was 6.4 equivalents of H to Pt. NaBH₄ (4mM), 2-MePy·BH₃ (5.3 mM), NaBH(OAc)₃ (16 mM). Flow rate of K₂PdCl₄, Pt precursor, NaBH₄, reductant for Pt solution: 4 mL/min. Diglyme as the capping agents (4 vol%) were added to ethanol in the carbon slurry. Inner diameter of the mixers (M1-M4): 0.5 mm, Inner diameter of reactors (R1-R3): 1.0 mm, length: 50 mm, Reaction temperature: 25 °C. b): Catalysts reported in Chapter 2.¹

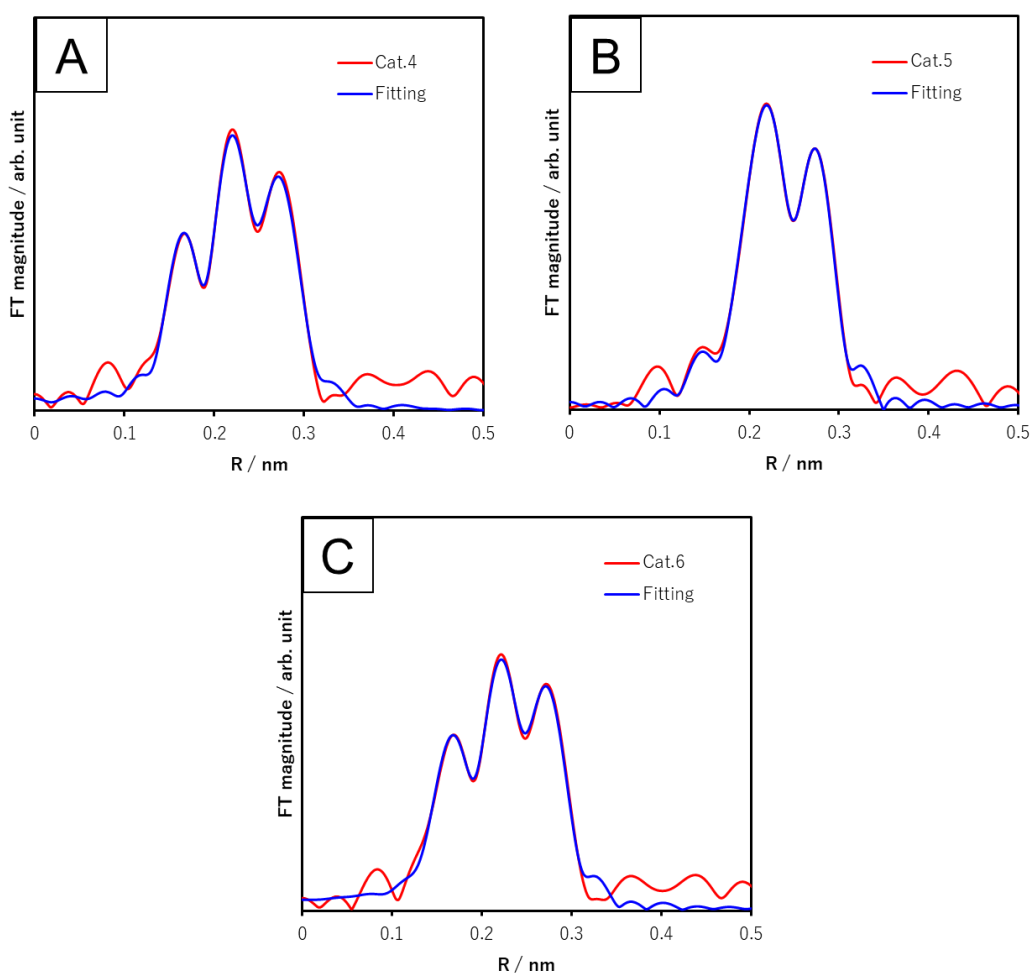


Figure 6. Fourier transform of the data (red lines) and first-shell fit (blue line) of A) Pt L₃ edges from Cat. 4, B) Pt L₃ edges from Cat. 5, and C) Pt L₃ edges from Cat. 6.

3.2.3. Morphology of core-shell catalysts

XAFS analysis revealed that Pd@Pt core-shell particles with a Pt_{1ML} shell can be synthesized by using 2-MePy·BH₃ reductant, but the Pt surface area and ORR activity showed low values. In order to elucidate the cause of this, the structure of the core-shell particles was analyzed by TEM. TEM images of Cat. 5 and Cat. 6 are shown in Figure 7. Primary particles with an average diameter of 3.7 nm and 3.8 nm were observed in Cat. 5 and Cat. 6, respectively. However, agglomeration is more advanced in Cat. 5 than in Cat. 2 (Capture 2. Figure 7D). The primary particles are agglomerated in a bead-like or block-like shape. XAFS confirms the Pt_{1ML} shell structure in Cat. 5, but the core-shell particles generated are highly aggregated, resulting in low surface area of Pt and low ORR activity. In Cat. 6, although some particles were agglomerated and bead-like secondary particles were observed, they were found to be very well dispersed on the carbon carrier.

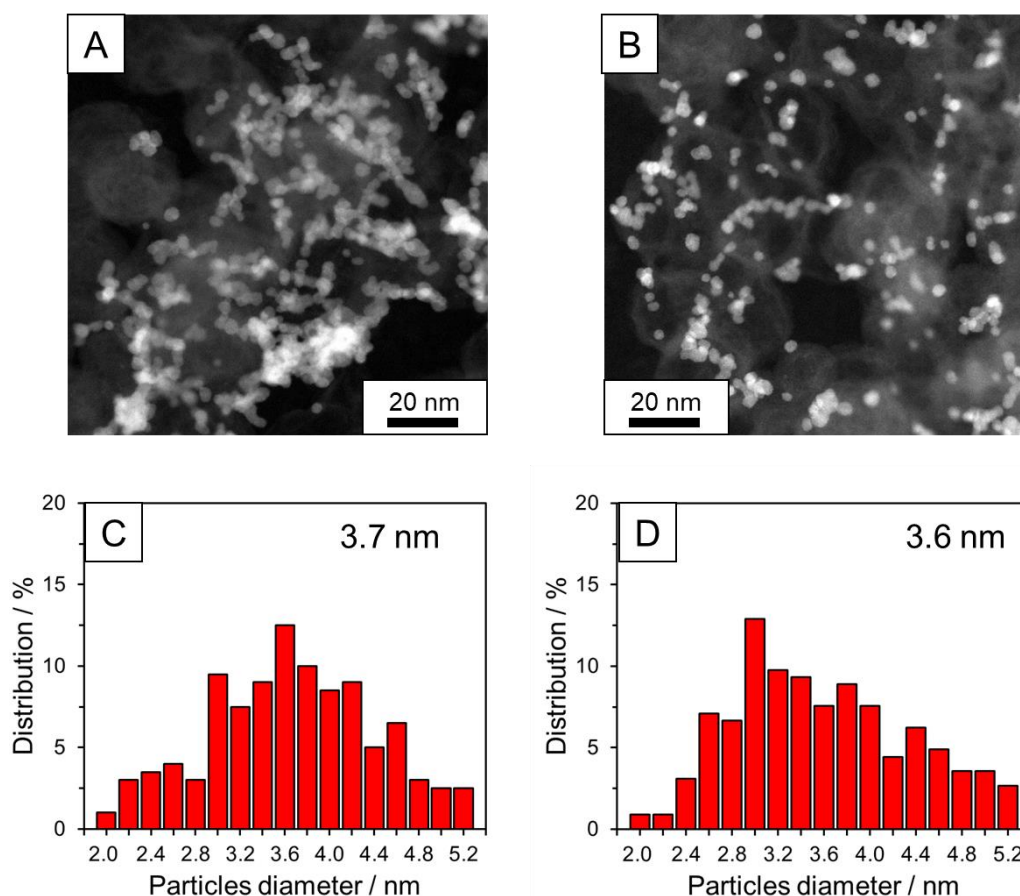


Figure 7. DF-STEM images and size distributions of A, C) Cat. 5 and B, D) Cat. 6.

To confirm the structure of the aggregated primary particles of Cat. 5, EDS analysis was performed focusing on the secondary particles, which are a bead-like aggregation of three particles (Fig. 8). Green (B) shows the distribution of Pd, which indicates the presence of spherical Pd particles of about 3 nm in diameter. Red (C) shows the distribution of Pt, which is larger than that of Pd (B), with 3.5 nm spherical particles. The color of the central part overlapped with Pd is light, indicating that the amount of Pt in the central part is small. The superposition of Pd and Pt EDS mapping (D) clearly shows a Pt-only (red) region on the surface of the particle, confirming that it has a Pd core-Pt shell structure.

As described above, together with the results of the XAFS analysis described earlier, it was clear that by using the 2-MePy·BH₃ reductant, the core-shell particles produced have a Pt_{1ML} shell structure, but the surface area of Pt is also reduced because the core-shell particles are loaded on carbon carrier with progressive aggregation between them, and thus the ORR activity is not sufficiently high.

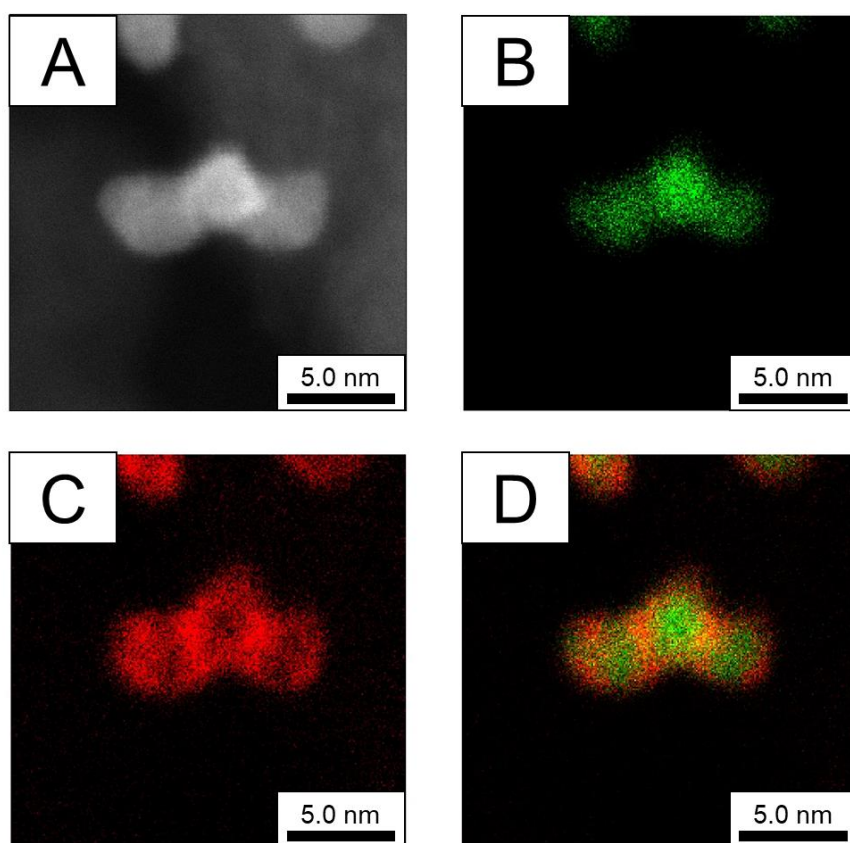


Figure 8. DF-STEM-EDS mapping images, with Pd shown in green and Pt in red, of Cat. 5.

3.2.4. Improvement of dispersibility of core-shell particles by adding capping agents

Therefore, I investigated a method to support core-shell particles with a Pt_{1ML} shell structure on the carbon carrier without agglomeration. First, I considered that diglyme was not effective enough as a capping agent, so I decided to examine the amount of diglyme added in the carbon slurry solution. The results of the fitting analysis of the EXAFS spectra are shown in Figure 9, and the Pt–Pt and Pt–Pd coordination numbers obtained from the analysis (Table 18 in the experimental section) and the ORR activity evaluation results are shown in Table 3. As the amount of diglyme added was increased by a factor of 2 or 10 over that used in Cat. 5, the Pt–Pt coordination number, Pt–Pd coordination number, and MA values tended to decrease, indicating that the excessive addition of diglyme hindered the formation of the core-shell structure. In particular, in Cat. 8, where 10 times the amount of diglyme was added, the Pt–Pt coordination number was estimated to be 4.6 and the Pt–Pd coordination number was 1.5, indicating a heterogeneous shell structure with 0~ several ML of Pt shells mixed together. On the other hand, TEM analysis shows that as the amount of diglyme added is increased by a factor of 2 and 10, the number of blocky secondary particles decreases and the percentage of bead-like interlinked particles increases (Figure 10, A and B). This improvement in dispersibility is consistent with the improvement in ECSA with increasing diglyme addition. Thus, increasing the amount of diglyme addition improves the dispersibility of the nanoparticles, but does not improve the catalytic activity due to the heterogeneous Pt shell structure. I had assumed that the reduction proceeds quickly at the stage where the Pt precursor and reductant come into contact (in the third mixer), and after the Pt shell is formed, the core-shell particles come into contact with the carbon slurry and are supported on the activated carbon. However, the diglyme added to the carbon slurry affected the Pt shell formation, suggesting that the reduction rate of the Pt precursor or the deposition rate of Pt(0) on Pd NPs was slower than expected and that the Pt shell may be formed in the carbon slurry.

Then, PVP, a proven capping agent for NPs, was added to the carbon slurry to check dispersibility. The same amount of PVP was used as in Cat. 1, 3.6 equivalents of monomer to Pt. The results of XAFS analysis (Figure 9) showed that Cat. 9 had a Pt–Pt coordination number of 6.2 and a Pt–Pd coordination number of 2.6, which is close to the coordination number of the Pt_{1ML} shell (Table 3). The TEM results also confirmed that the dispersibility of the particles in Cat. 9 is greatly improved compared to Cat. 5 (Figure 10C). The improvement in dispersibility is evident from the increase in ECSA. This may be due to the stronger coordination of PVP with the amide structure to the particles than with the diglyme with the ether structure. In addition, the amount of PVP added in the carbon slurry is much smaller than in the diglyme, indicating that PVP has no negative effect on the formation of the Pt shell. However, PVP significantly inhibits ORR activity,¹ and MA drops to 142. These results

suggest that a new dispersant that can improve dispersibility while maintaining the Pt shell structure of 1ML without inhibiting Pt shell formation needs to be selected.

Table 3. Effect of capping agents on the Pt shell structure and catalytic properties of Pt@Pd core-shell particles^{a)}.

Cat.	Capping agent	$N_{\text{Pt-Pt}}$	$N_{\text{Pt-Pd}}$	ECSA [$\text{m}^2 \text{g-Pt}^{-1}$]	MA@0.9V [A g-Pt^{-1}]	SA@0.9V [$\mu\text{A cm}^{-2}$]
7	diglyme (1175 eq.-Pt)	5.9	1.9	99	260	264
8	diglyme (5875 eq.-Pt)	4.5	1.5	114	212	184
9	PVP (3.6 eq.-Pt)	6.5	2.7	115	142	125

a): Pd@Pt/C was synthesized by the direct-support flow process. K_2PdCl_4 : 5 mM, H_2PtCl_6 : 2.5mM, NaBH_4 : 8 mM (for Pd), 2-MePy· BH_3 : 5.3 mM (for Pt). Flow rate of K_2PdCl_4 , H_2PtCl_6 , NaBH_4 , 2-MePy· BH_3 solution: 4 mL/min, Capping agents were added to ethanol in the carbon slurry, as necessary. Inner diameter of the mixers (M1-M4): 0.5 mm, Inner diameter of reactors (R1-R3): 1.0 mm, length: 50 mm, Reaction temperature: 25 °C.

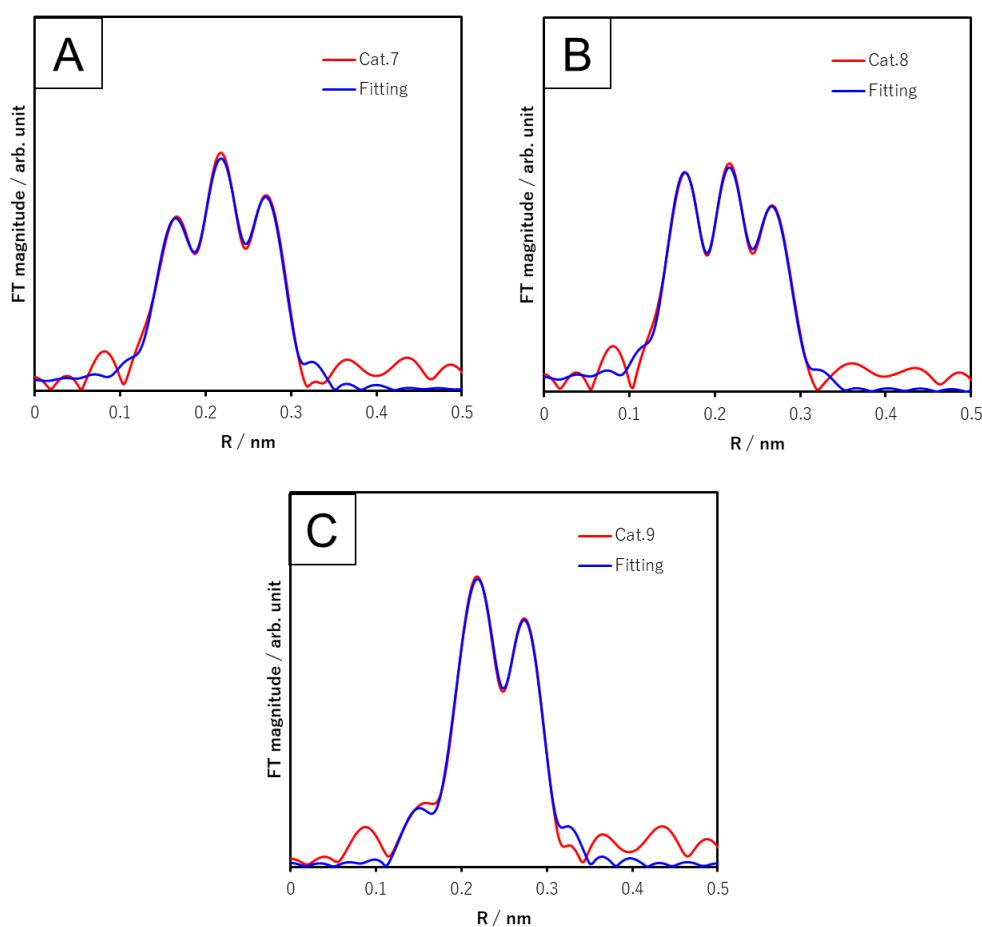


Figure 9. Fourier transform of the data (red lines) and first-shell fit (blue line) of A) Pt L3 edges from Cat. 7, B) Pt L3 edges from Cat. 8, and C) Pt L3 edges from Cat. 9.

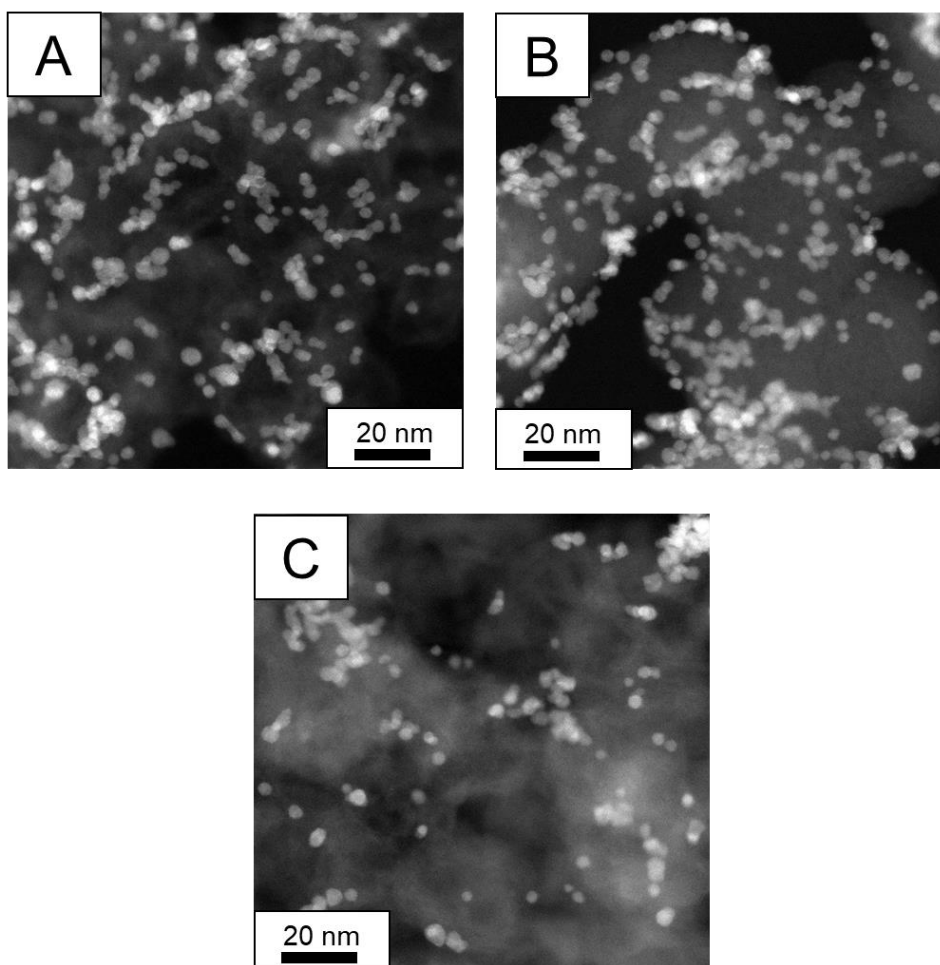


Figure 10. DF-STEM images of A) Cat. 7, B) Cat. 8, and C) Cat. 9.

Coordinating organic compounds that coordinate to nanoparticles with heteroatoms such as O, S, and N are widely used as capping agents.¹³ Carbonyl compounds, alcohols, and ethers are known as functional groups that coordinate with O.¹³ The carbonyl compound, PVP with an amide skeleton, is considered unsuitable because it inhibits the ORR reaction as mentioned above. Alcohols and ethers are also known to be inappropriate as capping agents for Pd@Pt core-shell particles due to their weak coordination strength.¹ S generally has a very strong coordination force, but like PVP, it is thought that it may inhibit the ORR reaction.^{14,15} On the other hand, pyridine compounds that coordinate with N have also been used as protectants in some cases.¹⁶⁻¹⁸ However, there was concern that they might inhibit ORR activity, so we decided to conduct a preliminary validation.

Commercially available Pt/C was added to an ethanol solution of 2-MePy, a pyridine compound, and stirred to adsorb 2-MePy on Pt NPs. The catalyst was collected by filtration and evaluated for ORR activity. For comparison, PVP K30, which is known to inhibit ORR activity, was also examined

in the same manner. The results of the ORR activity evaluation are shown in Table 4. The addition of 2-MePy to Pt at 2.1 and 6.4 equivalents showed almost the same MA as that of Pt/C. From this result, it is expected that pyridine compounds have little effect on ORR activity. By the way, it has been reported that the addition of some nitrogen-containing compounds such as melamine improves the ORR activity of Pt/C.^{19,20} However, from the results of this study, it was confirmed that 2-MePy has no effect on the enhancement of ORR activity. In the case of PVP K30-doped Pt/C catalyst synthesized by the same method, MA decreased in proportion to the amount of PVP K30 added. This result is consistent with the inhibition of Pd@Pt catalyst activity by PVP K30 described in Chapter 2.

Table 4. Effect of 2-MePy and PVP on ORR activity of Pt/C.

Cat.	ECSA [m ² g-Pt ⁻¹]	MA@0.9V [A g-Pt ⁻¹]	SA@0.9V [μA cm ⁻²]
Pt/C	40	180	447
Pt/C+2-MePy (2.1 eq.-Pt)	42	186	440
Pt/C+2-MePy (6.4 eq.-Pt)	43	180	422
Pt/C+PVP K30 (0.6 eq.-Pt)	42	159	382
Pt/C+PVP K30 (1.2 eq.-Pt)	41	144	350
Pt/C+PVP K30 (2.4 eq.-Pt)	43	129	300

Therefore, a pyridine compound was added as a protective material to study its effect on the catalyst structure, dispersibility, and ORR activity. As a pyridine compound, 2-MePy, which is also contained in the reducing agent, was selected. The results of the fitting analysis of the EXAFS spectra are shown in Figure 11, and the Pt–Pt and Pt–Pd coordination numbers obtained from the analysis (Table 19 in the experimental section) and the ORR activity evaluation results are shown in Table 5. 2-MePy was supplied mixed with 2-MePy·BH₃, a reducing agent for Pt. The Pt–Pt coordination number decreased gradually as the amount of 2-MePy added increased, but at 2.1 to 10.5 equivalents, the value was around 6.0, which was consistent with the coordination number of Pt_{1ML}. On the other hand, the Pt–Pd coordination number also shows little change, ranging from 2.5-3.0. This is also in good agreement with the Pt_{1ML} values. ECSA and MA also increase with the addition of 2-MePy, with a maximum value of 472 for MA at Cat. 12 with the addition of 10.5 equivalents. It is clear that the addition of 2-MePy improves the dispersibility of Pd@Pt core-shell catalysts with a Pt_{1ML} shell and increases the Pt surface area and MA. However, as the amount of 2-MePy increases above 10.5 equivalents, the Pt–Pt and Pt–Pd coordination numbers decrease, and at 42.0 equivalents of 2-MePy addition, the coordination numbers decrease to 3.3 and 1.2 (Cat. 15). This result indicates that the

excess addition of 2-MePy results in a non-uniform Pt shell structure or does not form a Pt shell. Furthermore, the result that ECSA continues to increase with both the amount of 2-MePy added suggests that Pt that has not taken on a shell structure may be loaded on carbon supports in a near-atomic state. Therefore, MA is explained as decreasing with the addition of excess 2-MePy because the formation of the core-shell structure is inhibited.

Table 5. Effect of 2-MePy doping on Pt shell structure and catalytic properties of Pt@Pd core-shell particles^{a)}.

Cat.	Amount of 2MePy added ^{b)} [eq.-Pt]	$N_{\text{Pt-Pt}}$	$N_{\text{Pt-Pd}}$	ECSA [m ² g-Pt ⁻¹]	MA@0.9V [A g-Pt ⁻¹]	SA@0.9V [μ A cm ⁻²]
5 ^{c)}	0 (2.1)	6.8	2.5	84	340	403
10	2.1 (4.2)	6.5	3.0	95	400	422
11	4.2 (6.3)	5.7	2.5	100	408	401
12	10.5 (12.6)	5.4	2.4	105	472	449
13	21.0 (23.1)	5.3	2.2	111	442	400
14	31.5 (33.7)	5.2	1.6	119	371	310
15	42.0 (44.1)	3.3	1.2	120	232	192

a): Pd@Pt/C was synthesized by the direct-support flow process. K₂PdCl₄: 5 mM, H₂PtCl₆: 2.5mM, NaBH₄: 8 mM (for Pd), 2-MePy·BH₃: 5.3 mM (for Pt). Flow rate of K₂PdCl₄, H₂PtCl₆, NaBH₄, 2-MePy·BH₃ solution: 4 mL/min. Diglyme as the capping agents (4 vol%) were added to ethanol in the carbon slurry. Inner diameter of the mixers (M1-M4): 0.5 mm, Inner diameter of reactors (R1-R3): 1.0 mm, length: 50 mm, Reaction temperature: 25 °C. b): 2-MePy was supplied in addition to the reductant solution for Pt. The numbers in parentheses are equal amounts including 2-MePy in the reductant for Pt (2-MePy·BH₃). c): Catalysts reported in Chapter 2¹.

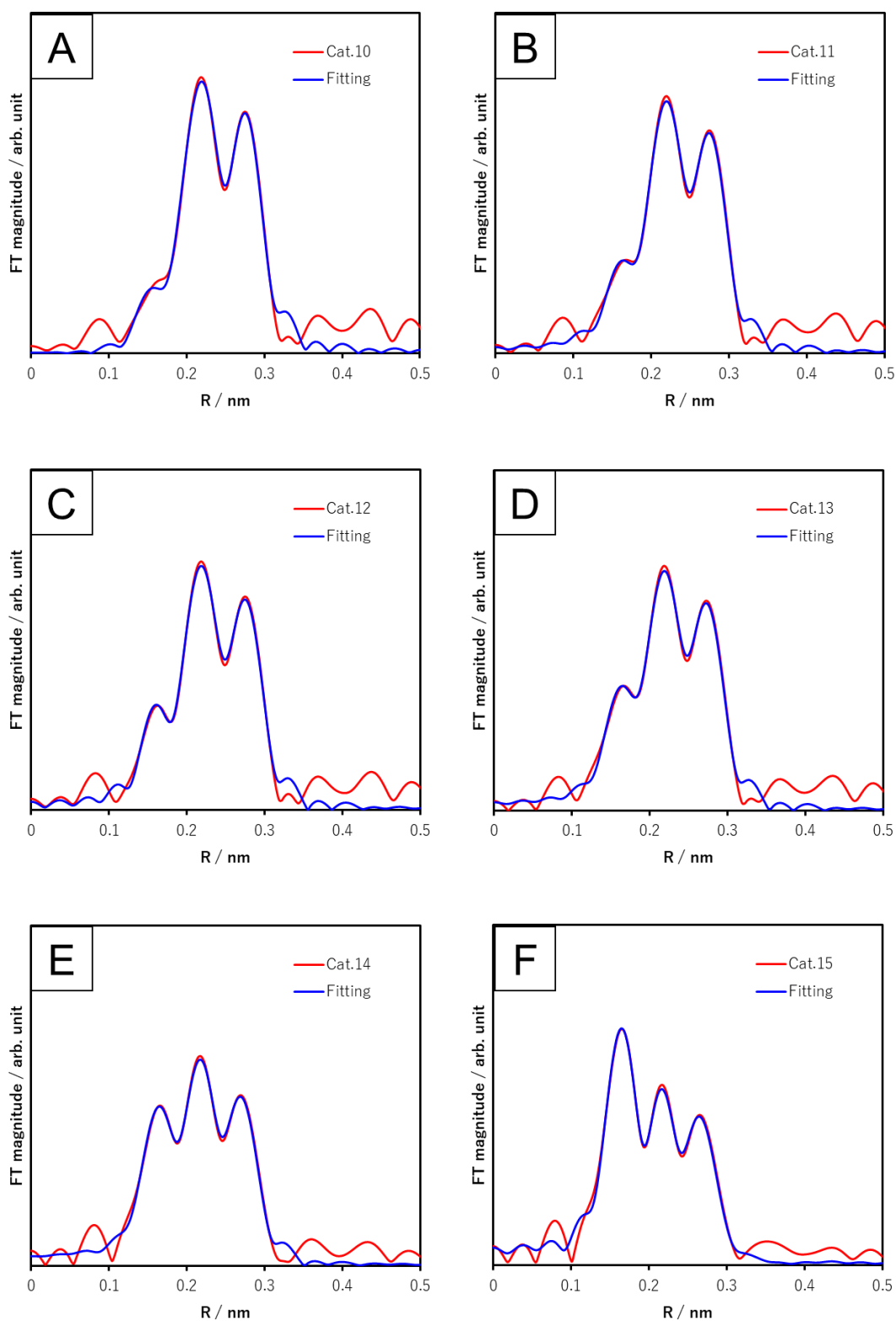


Figure 11. Fourier transform of the data (red lines) and first-shell fit (blue line) of A) Pt L3 edges from Cat. 10, B) Pt L3 edges from Cat. 11, C) Pt L3 edges from Cat. 12, D) Pt L3 edges from Cat. 13, E) Pt L3 edges from Cat. 14 and F) Pt L3 edges from Cat. 15.

3.2.5. Effect of 2-MePy

Since it was found that the addition of an appropriate amount of 2-MePy can disperse Pd@Pt on carbon supports while maintaining the Pd@Pt core-shell structure, I next investigated the effect of varying the amount of 2-MePy·BH₃ on the core-shell structure and dispersibility in order to examine whether the reducing agent containing 2-MePy can act as a capping agent. The results of the fitting analysis of the EXAFS spectra are shown in Figure 12, and the Pt–Pt and Pt–Pd coordination numbers obtained from the analysis (Table 20 in the experimental section) and the results of the ORR activity evaluation are shown in Table 6.

Up to 6.4 equivalents of 2-MePy·BH₃, the Pt–Pt and Pt–Pd coordination numbers are close to the theoretical values of Pt_{1ML}, indicating that a uniform 1 ML shell structure is maintained. ECSA and MA increase with increasing reductant, with MA having the highest value of 522 at 6.4 equivalents (Cat. 17). This value is almost comparable in activity to the Pd@Pt catalyst by the Cu-UPD method.² However, it can be seen that MA decreases with further increase of 2-MePy·BH₃ addition. The effect of 2-MePy addition on Pt–Pt and Pt–Pd coordination number, ECSA, and MA is almost the same whether 2-MePy is added as a reductant or as 2-MePy. In other words, it is considered that 2-MePy generated from 2-MePy·BH₃ acts as a capping agent. Complexes of BH₃ with pyridine derivatives having a structure similar to 2-MePy·BH₃ have been reported to form Pyridine derivatives and B(OH)₃ by reduction and hydrolysis.^{21,22} Therefore, I believe that the Pt precursor and 2-MePy·BH₃ also react in the reaction system as follows to give 2-MePy. The following reaction equation is based on a reported example of the reaction equation between NaBH₄ and H₂PtCl₆.^{23,24}



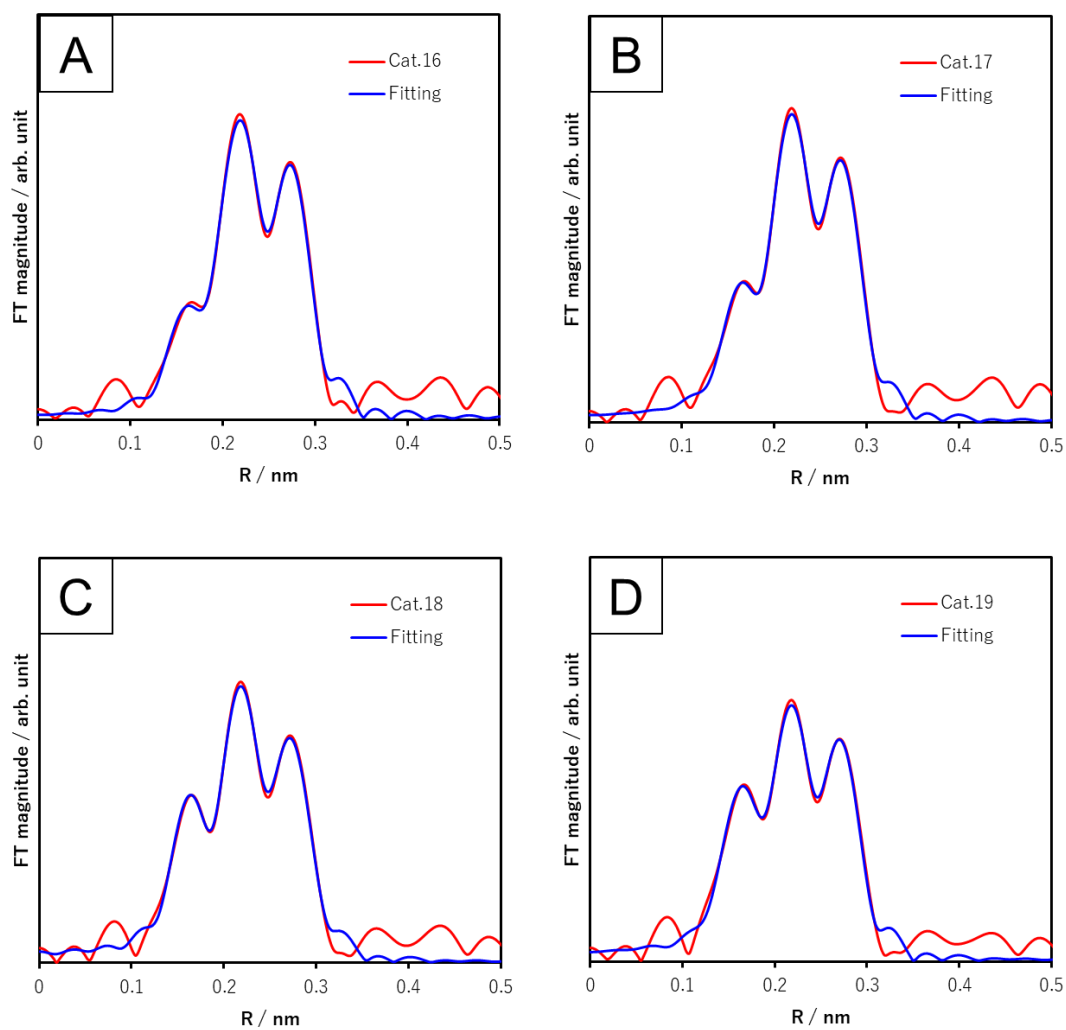


Figure 12. Fourier transform of the data (red lines) and first-shell fit (blue line) of A) Pt L3 edges from Cat. 16, B) Pt L3 edges from Cat. 17, C) Pt L3 edges from Cat. 18 and D) Pt L3 edges from Cat. 19.

Table 6. Effect of the amount of 2-MePy·BH₃ (reducing agent) on the Pt shell structure and catalytic properties of Pt@Pd core-shell particles^{a)}.

Cat.	Amount of 2-MePy·BH ₃ [eq.-Pt]	N _{Pt-Pt}	N _{Pt-Pd}	ECSA [m ² g-Pt ⁻¹]	MA@0.9V [A g-Pt ⁻¹]	SA@0.9V [μA cm ⁻²]
5 ^{b)}	2.1	6.8	2.5	84	340	403
16	4.3	6.0	2.4	101	480	476
17	6.4	5.6	2.4	107	522	489
18	10.7	5.2	2.0	115	404	353
19	21.3	5.4	2.0	121	388	319

a): Pd@Pt/C was synthesized by the direct-support flow process. K₂PdCl₄: 5 mM, H₂PtCl₆: 2.5mM, NaBH₄: 8 mM (for Pd), 2-MePy·BH₃: 5.3~53.3 mM (for Pt). Flow rate of K₂PdCl₄, H₂PtCl₆, NaBH₄, 2-MePy·BH₃ solution: 4 mL/min. Diglyme as the capping agents (4 vol%) were added to ethanol in the carbon slurry. Inner diameter of the mixers (M1-M4): 0.5 mm, Inner diameter of reactors (R1-R3): 1.0 mm, length: 50 mm, Reaction temperature: 25 °C. b): Catalysts reported in Chapter 2¹

TEM image of Cat. 17, which showed the highest activity, is shown in Figure 13A. The Pd@Pt NPs showed a significant improvement in particle dispersion compared to Cat. 4. This is consistent with the ECSA results, and it is clear that 2-MePy functions as a capping agent. In addition, a single Pd@Pt particle was taken out and subjected to EDS mapping analysis (Figure 13B), which clearly shows that Pt (red area) is uniformly distributed on the spherical Pd particles, confirming that the Pd core-Pt shell structure is present. Here, in order to examine the Pt shell structure in detail, an EELS line analysis was performed, and the results are shown in Figure 13C. The analysis estimated the thickness of the Pt shell to be about 0.25 nm. Since the atomic diameter of Pt is 0.28 nm, it is clear that Pd@Pt core-shell NPs were synthesized with a Pt_{1ML} shell, even as a local structure.

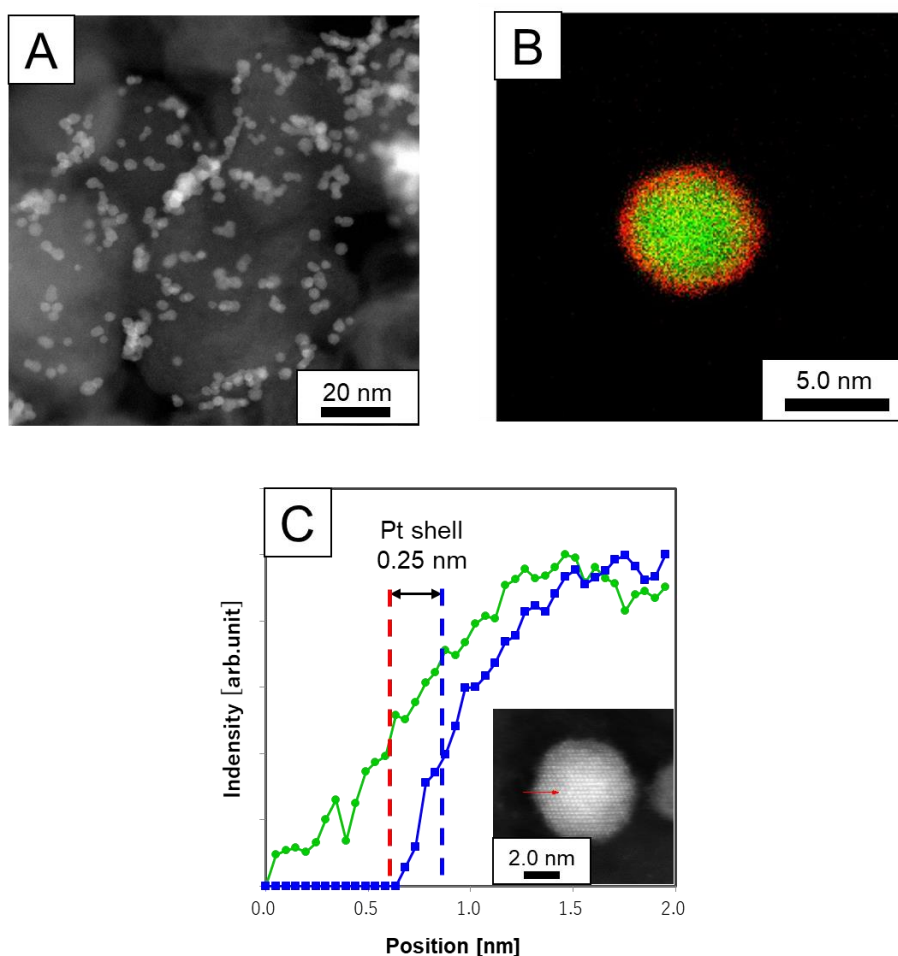


Figure 13. DF-STEM images (A), EDS-mapping image (B), and EELS signal (C) of Cat. 17.

Finally, the effect of 2-MePy is discussed based on the previous results. The roles of 2-MePy are i) to form a monoatomic Pt shell structure and ii) to suppress the aggregation of the generated Pt@Pd NPs. Regarding the first point, the effect on the formation of monoatomic layer Pt shells, it is known that in metal NPs, the shape is controlled by changing the growth rate of the crystal plane by adding various additives.^{25,26} There are also reported cases where the crystal structure of Pt NPs is changed by controlling the amount of polymeric capping agents added.^{26,27} This is due to the selective adsorption of additive molecules on certain crystal planes, which restricts growth on crystal planes with strong binding strength and promotes growth on crystal planes with weak binding strength.^{25,26} This suggests that 2-MePy has a similar effect. In other words, a Pt shell is formed by the precipitation of Pt with 2-MePy N coordination on Pd. On the other hand, 2-MePy on Pt is considered to have formed a monatomic layer of Pt shell by inhibiting the formation of Pt stacking structure (Figure 14). The resurfacing of the Pt shell is a Pt(111) structure, suggesting that 2-MePy may have inhibited crystal

growth on the Pt (111) surface. I also believe that nitrogen suppressed the ligand and aggregation to NPs as in previous reports (Figure 14).¹⁶⁻¹⁸ Note that when the total amount of 2-MePy in the reaction system was the same, the ECSA was higher when 2-MePy was added as part of the reducing agent than when it was added separately and was more effective as a dispersant (Cat. 10 vs Cat. 16, and Cat. 11 vs Cat. 17). I believe this is because in the case of 2-MePy·BH₃, Py is present in the vicinity of Pt (0) immediately after reduction, allowing for more rapid coordination and protection.

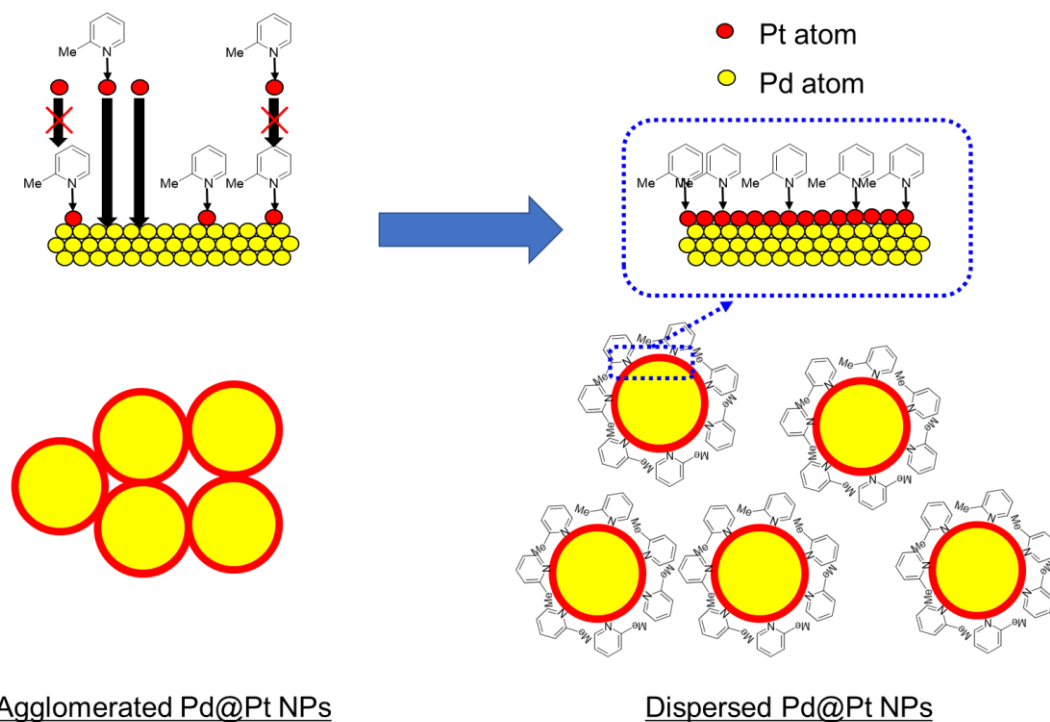


Figure 14. Effects of 2-MePy.

To verify this effect, Cat. 20 was synthesized by using NaBH₄ as a reductant for Pt and adding 2-MePy to this reductant solution for Pt. When synthesizing a complex of a pyridine derivative and BH₃ such as 2-MePy·BH₃ from NaBH₄, a method of synthesizing a pyridine salt in advance and reacting it with NaBH₄ has been reported, or a method of synthesizing NaBH₄ by reacting it with an acid or metal salt and trapping the borane generated in the system in pyridine.^{28,29} Therefore, I believe that 2-MePy·BH₃ is not generated when NaBH₄ and 2-MePy are simply mixed as described above. The results of the fitting analysis of the EXAFS spectra of catalyst 20 are shown in Figure 15A, and the Pt–Pt and Pt–Pd coordination numbers obtained from the analysis (Table 21 in the experimental section) and the ORR activity evaluation results are shown in Table 7. The Pt–Pt and Pt–Pd coordination numbers of Cat. 20 are 6.0 and 2.4, which are close to the theoretical values of Pt_{1ML},

indicating that Pt has a uniform 1 ML shell structure. This result indicates that 2-MePy is effective in forming a uniform Pt_{1ML} shell. On the other hand, the MA of Cat. 20 is 210, which is very low activity compared to Cat. 5, which uses 2-MePy·BH₃ as reductant. This is explained by the ECSA and TEM (Figure 15B) results, which show that particle agglomeration was more pronounced than for Cat. 5.

Table 6. Effect of the amount of 2-MePy·BH₃ (reducing agent) on the Pt shell structure and catalytic properties of Pt@Pd core-shell particles^{a)}.

Cat.	Reductant ^{b)}	N _{Pt-Pt}	N _{Pt-Pd}	ECSA [m ² g-Pt ⁻¹]	MA@0.9V [A g-Pt ⁻¹]	SA@0.9V [μA cm ⁻²]
20	NaBH ₄ + 2-MePy	6.0	2.4	50	210	420

a): Pd@Pt/C was synthesized by the direct-support flow process. K₂PdCl₄: 5 mM, H₂PtCl₆: 2.5 mM, NaBH₄: 8 mM (for Pd), NaBH₄: 4 mM (for Pt). 2-MePy (4 mM) was supplied in addition to the reductant solution for Pt. Flow rate of K₂PdCl₄, H₂PtCl₆, NaBH₄, 2-MePy·BH₃ solution: 4 mL/min. Diglyme as the capping agents (4 vol%) were added to ethanol in the carbon slurry. Inner diameter of the mixers (M1-M4): 0.5 mm, Inner diameter of reactors (R1-R3): 1.0 mm, length: 50 mm, Reaction temperature: 25 °C.

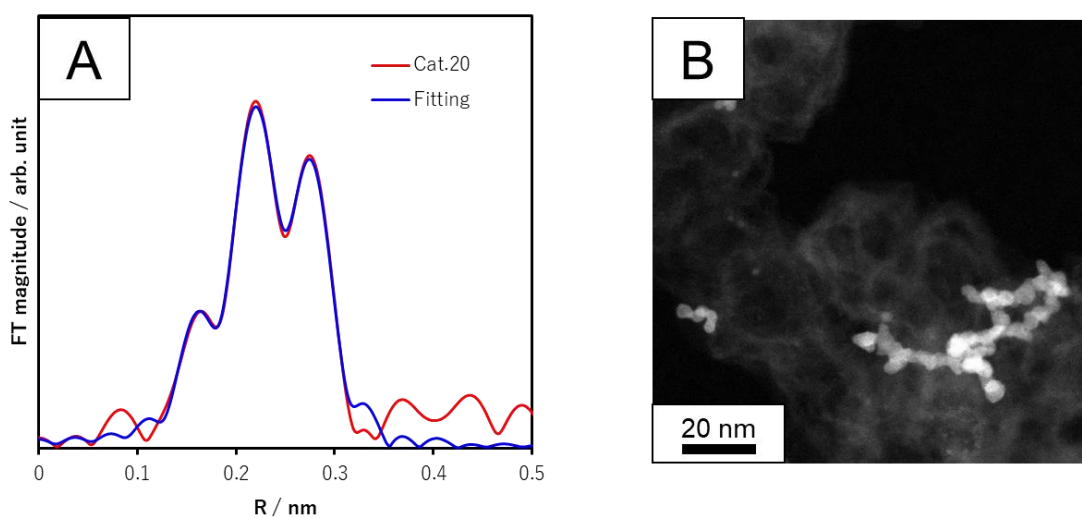


Figure 15. (A) Fourier transform of the data (red lines) and first-shell fit (blue line) of Pt L3 edges from Cat. 20, and (B) DF-STEM images of Cat. 20.

3.3. Conclusion

Flow synthesis of Pd@Pt_{1ML}/C with highly controlled Pt shell thickness has been successfully achieved. By utilizing a newly developed high-throughput flow synthesis system for the preparation of core-shell catalysts, various conditions were rapidly evaluated, and it was quickly found that Pd@Pt_{1ML}/C with a uniform 1 atomic layer of Pt shell can be synthesized by using 2-MePy·BH₃ as the reductant for Pt. The dispersibility was improved by increasing the amount of 2-MePy in the reaction system while maintaining the 1ML structure, and finally, by using 6.4 equivalents of reducing agent, the ORR activity was comparable to that of catalysts synthesized by the Cu-UPD method. The role of 2-MePy is to coordinate to Pt with N to suppress the stacking of Pt shells to form a uniform Pt_{1ML} shell, and to suppress the aggregation of the formed NPs. This flow method was shown to be a promising alternative to the Cu-UPD method for the synthesis of core-shell type catalysts with high productivity and a high degree of catalyst structure control.

3.4. Experimental

3.4.1. Chemicals and materials

All chemicals were commercial products and used without further purification. K_2PdCl_4 (99.99%) and $H_2PtCl_6 \cdot 6H_2O$ ($\geq 37.50\%$ Pt basis) were purchased from Sigma-Aldrich. $2-MePy \cdot BH_3$, $NaBH_4$, $NaBH(OAc)_3$, PVP K30, ethanol, diglyme, 5 wt% Nafion solution, and 60% $HClO_4$ were purchased from Fujifilm Wako Pure Chemical Corporation. Carbon ECP was purchased from Lion Specialty Chemicals Co., Ltd. All aqueous solutions were prepared using highly purified deionized water with a resistivity of 18.2 $M\Omega$ cm.

3.4.2. Synthesis of Pd@Pt/C catalysts by the flow process

Flow synthesis of the Pd@Pt catalyst was performed using the method described in the experimental section of Chapter 2.

3.4.3. Characterization of catalyst

3.4.3.1. TEM / EDS / EELS

Analyzed using the same methods as described in the experimental section of Chapter 2.

3.4.3.2. XPS measurement

XPS measurements were carried out by means of a VG Scientific ESCALAB 250. XP spectra were measured with Al $K\alpha$ radiation (1486.6 eV), and were obtained at pass energy of 20 eV and step size of 0.1 eV. The photoelectrons were collected at the angle normal to the surface.

3.4.3.3. XAFS measurement

All measurements were performed at the Super Photon ring-8 GeV (SPring-8) using Beam Line BL14B2.^{30,31} The sample was packed into a SUS pipe (I.D. = 7 mm) and measured at the Pt L_3 edge (11, 564 eV) and Pd L_3 edge (24,350 eV) at room temperature using a Si (311) double crystal monochromator in a transmission mode. The data were processed and analyzed by Athena and Artemis software.³² In the curve-fitting analysis, backscattering amplitude, phase shift were calculated by FEFF6 and then the other parameters, including the number of neighboring atoms, interatomic distance between the adsorbed atom to the neighboring atom, the Debye-Waller factor, and absorption edge energy, were treated as fitting parameters. The intrinsic loss factor was obtained by curve-fitting analysis of the extended X-ray absorption fine structure (EXAFS) data for the Pt foil.

Table 16. EXAFS fit parameters^{a)} of Cat. 1 and Cat. 2.

Sample	Shell	CN ^{b)}	S ₀ ^{2,c)}	R ^{d)} / x 10 ⁻¹ [nm]	σ ^{2,e)} / x 10 ⁻² [nm ²]	R _{factor} ^{f)}
Pt foil	Pt–Pt	12	0.80	2.77 ± 0.00	0.0044 ± 0.0002	0.001
Cat. 1	Pt–Pt	5.0	0.80	2.68 ± 0.07	0.0096 ± 0.0077	0.006
	Pt–Pd	2.0	0.80	2.72 ± 0.05	0.0081 ± 0.0077	
	Pt–O	1.3	0.80	1.99 ± 0.06	0.0042 ± 0.0054	
Cat. 2	Pt–Pt	4.7	0.80	2.69 ± 0.07	0.0096 ± 0.0082	0.008
	Pt–Pd	1.7	0.80	2.73 ± 0.05	0.0077 ± 0.0078	
	Pt–O	1.5	0.80	2.00 ± 0.06	0.0058 ± 0.0071	

a): k^3 : k-range = 0.3–1.2 nm⁻¹. r-range = 0.17–0.33 and 0.10–0.33 nm for Pt foil and Pd@Pt catalysts, respectively. b): Coordination number. c): Intrinsic loss factor. d): Bond length. e): Debye-Waller factor. f): Goodness-of-fit index.

Table 17. EXAFS fit parameters^{a)} of Cat. 4, Cat. 5, and Cat. 6.

Sample	Shell	CN ^{b)}	S ₀ ^{2,c)}	R ^{d)} / x 10 ⁻¹ [nm]	σ ^{2,e)} / x 10 ⁻² [nm ²]	R _{factor} ^{f)}
Pt foil	Pt–Pt	12	0.80	2.77 ± 0.00	0.0043 ± 0.0002	0.001
Cat. 4	Pt–Pt	4.3	0.80	2.72 ± 0.05	0.0071 ± 0.0061	0.008
	Pt–Pd	2.0	0.80	2.73 ± 0.03	0.0058 ± 0.0054	
	Pt–O	1.2	0.80	2.02 ± 0.06	0.0052 ± 0.0075	
Cat. 5	Pt–Pt	6.8	0.80	2.70 ± 0.01	0.0089 ± 0.0021	0.002
	Pt–Pd	2.5	0.80	2.72 ± 0.01	0.0071 ± 0.0020	
	Pt–O	0.2	0.80	1.81 ± 0.07	-0.0014 ± 0.0094	
Cat. 6	Pt–Pt	5.0	0.80	2.71 ± 0.05	0.0092 ± 0.0065	0.007
	Pt–Pd	1.9	0.80	2.73 ± 0.04	0.0075 ± 0.0061	
	Pt–O	1.2	0.80	2.01 ± 0.06	0.0056 ± 0.0066	

a): k^3 : k-range = 0.3–1.2 nm⁻¹. r-range = 0.17–0.33 and 0.10–0.33 nm for Pt foil and Pd@Pt catalysts, respectively. b): Coordination number. c): Intrinsic loss factor. d): Bond length. e): Debye-Waller factor. f): Goodness-of-fit index.

Table 18. EXAFS fit parameters^{a)} of Cat. 7, Cat. 8, and Cat. 9.

Sample	Shell	CN ^{b)}	S ₀ ^{2,c)}	R ^{d)} / x 10 ⁻¹ [nm]	σ ^{2,e)} / x 10 ⁻² [nm ²]	R _{factor} ^{f)}
Pt foil	Pt–Pt	12	0.78	2.77 ± 0.00	0.0041 ± 0.0009	0.003
	Pt–Pt	5.9	0.78	2.68 ± 0.06	0.0098 ± 0.0069	
Cat. 7	Pt–Pd	1.9	0.78	2.71 ± 0.04	0.0079 ± 0.0078	0.008
	Pt–O	1.3	0.78	1.98 ± 0.07	0.0056 ± 0.0069	
Cat. 9	Pt–Pt	6.4	0.78	2.71 ± 0.02	0.0085 ± 0.0024	0.004
	Pt–Pd	2.7	0.78	2.72 ± 0.02	0.0070 ± 0.0023	
	Pt–O	0.3	0.78	1.84 ± 0.08	0.0030 ± 0.0111	
Pt foil	Pt–Pt	12	0.81	2.77 ± 0.00	0.0044 ± 0.0002	0.001
	Pt–Pt	4.5	0.81	2.68 ± 0.07	0.0090 ± 0.0080	
Cat. 8	Pt–Pd	1.5	0.81	2.70 ± 0.04	0.0067 ± 0.0079	0.007
	Pt–O	1.6	0.81	2.00 ± 0.06	0.0053 ± 0.0054	

a): k^3 : k-range = 0.3–1.2 nm⁻¹. r-range = 0.17–0.33 and 0.10–0.33 nm for Pt foil and Pd@Pt catalysts, respectively. b): Coordination number. c): Intrinsic loss factor. d): Bond length. e): Debye-Waller factor. f): Goodness-of-fit index.

Table 19. EXAFS fit parameters^{a)} of Cat. 10 to Cat. 15.

Sample	Shell	CN ^{b)}	S ₀ ^{2,c)}	R ^{d)} / x 10 ⁻¹ [nm]	σ ^{2,e)} / x 10 ⁻² [nm ²]	R _{factor} ^{f)}
Pt foil	Pt–Pt	12	0.81	2.77 ± 0.00	0.0044 ± 0.0002	0.001
Cat. 10	Pt–Pt	6.5	0.81	2.71 ± 0.02	0.0087 ± 0.0032	0.006
	Pt–Pd	3.0	0.81	2.73 ± 0.02	0.00877 ± 0.0031	
	Pt–O	0.5	0.81	1.89 ± 0.12	0.0055 ± 0.0148	
Cat. 11	Pt–Pt	5.7	0.81	2.61 ± 0.03	0.0083 ± 0.0051	0.008
	Pt–Pd	2.5	0.81	2.73 ± 0.03	0.0071 ± 0.0049	
	Pt–O	0.7	0.81	1.98 ± 0.13	0.0066 ± 0.0149	
Cat. 12	Pt–Pt	5.4	0.81	2.71 ± 0.03	0.0079 ± 0.0047	0.007
	Pt–Pd	2.3	0.81	2.72 ± 0.02	0.0069 ± 0.0047	
	Pt–O	0.7	0.81	1.98 ± 0.09	0.0049 ± 0.0104	
Cat. 13	Pt–Pt	5.3	0.81	2.70 ± 0.04	0.0083 ± 0.0055	0.008
	Pt–Pd	2.2	0.81	2.72 ± 0.03	0.0069 ± 0.0055	
	Pt–O	1.0	0.81	1.99 ± 0.09	0.0065 ± 0.0100	
Cat. 14	Pt–Pt	5.2	0.81	2.68 ± 0.06	0.0095 ± 0.0070	0.006
	Pt–Pd	1.6	0.81	2.71 ± 0.04	0.0073 ± 0.0076	
	Pt–O	1.3	0.81	1.00 ± 0.07	0.0059 ± 0.0066	
Cat. 15	Pt–Pt	3.3	0.81	2.69 ± 0.07	0.0082 ± 0.0084	0.006
	Pt–Pd	1.2	0.81	2.70 ± 0.04	0.0060 ± 0.0080	
	Pt–O	2.0	0.81	2.01 ± 0.04	0.0052 ± 0.0040	

a): k^3 : k-range = 0.3–1.2 nm⁻¹. r-range = 0.17–0.33 and 0.10–0.33 nm for Pt foil and Pd@Pt catalysts, respectively. b): Coordination number. c): Intrinsic loss factor. d): Bond length. e): Debye-Waller factor. f): Goodness-of-fit index.

Table 20. EXAFS fit parameters^{a)} of Cat. 16 to Cat. 19.

Sample	Shell	CN ^{b)}	S ₀ ^{2,c)}	R ^{d)} / x 10 ⁻¹ [nm]	σ ^{2,e)} / x 10 ⁻² [nm ²]	R _{factor} ^{f)}
Pt foil	Pt–Pt	12	0.81	2.77 ± 0.00	0.0044 ± 0.0002	0.001
Cat. 16	Pt–Pt	6.0	0.81	2.70 ± 0.03	0.0088 ± 0.0046	0.006
	Pt–Pd	2.4	0.81	2.72 ± 0.02	0.0073 ± 0.0043	
	Pt–O	0.6	0.81	1.96 ± 0.10	0.0054 ± 0.0110	
Cat. 17	Pt–Pt	5.6	0.81	2.70 ± 0.04	0.0085 ± 0.0056	0.007
	Pt–Pd	2.4	0.81	2.72 ± 0.03	0.0069 ± 0.0050	
	Pt–O	0.9	0.81	1.99 ± 0.10	0.0061 ± 0.0113	
Cat. 18	Pt–Pt	5.2	0.81	2.70 ± 0.04	0.0085 ± 0.0052	0.006
	Pt–Pd	2.0	0.81	2.72 ± 0.02	0.0066 ± 0.0049	
	Pt–O	1.1	0.81	1.99 ± 0.06	0.0055 ± 0.0069	
Cat. 19	Pt–Pt	5.4	0.81	2.68 ± 0.06	0.0097 ± 0.0074	0.008
	Pt–Pd	2.0	0.81	2.72 ± 0.04	0.0082 ± 0.0078	
	Pt–O	1.1	0.81	1.98 ± 0.08	0.0056 ± 0.0079	

a): k^3 : k-range = 0.3–1.2 nm⁻¹. r-range = 0.17–0.33 and 0.10–0.33 nm for Pt foil and Pd@Pt catalysts, respectively. b): Coordination number. c): Intrinsic loss factor. d): Bond length. e): Debye-Waller factor. f): Goodness-of-fit index.

Table 21. EXAFS fit parameters^{a)} of Cat. 20.

Sample	Shell	CN ^{b)}	S ₀ ^{2,c)}	R ^{d)} / x 10 ⁻¹ [nm]	σ ^{2,e)} / x 10 ⁻² [nm ²]	R _{factor} ^{f)}
Pt foil	Pt–Pt	12	0.81	2.77 ± 0.00	0.0044 ± 0.0002	0.001
Cat. 20	Pt–Pt	6.0	0.81	2.71 ± 0.03	0.0081 ± 0.0041	0.005
	Pt–Pd	2.4	0.81	2.73 ± 0.02	0.0067 ± 0.0040	
	Pt–O	0.7	0.81	1.98 ± 0.08	0.0045 ± 0.0091	

a): k^3 : k-range = 0.3–1.2 nm⁻¹. r-range = 0.17–0.33 and 0.10–0.33 nm for Pt foil and Pd@Pt catalysts, respectively. b): Coordination number. c): Intrinsic loss factor. d): Bond length. e): Debye-Waller factor. f): Goodness-of-fit index.

3.4.3.4. Electrochemical measurements

Measured using the same methods as described in the experimental section of Chapter 2.

3.5. References

- [1] Y. Hashiguchi, F. Watanabe, T. Honma, I. Nakamura, S. S. Poly, T. Kawaguchi, T. Tsuji, H. Murayama, M. Tokunaga, T. Fujitani, *Colloids Surf. A* **2021**, *620*, 126607.
- [2] K. Sasaki, J. X. Wang, H. Naohara, N. Marinkovic, K. More, H. Inada, R. R. Adzic, *Electrochim. Acta* **2010**, *55*, 2645–2652.
- [3] Y. Shinke, T. Miyazawa, M. Hiza, I. Nakamura, T. Fujitani, *React Chem Eng* **2021**, *6*, 1381–1385.
- [4] T. Kashiwagi, K. Sue, Y. Takebayashi, T. Ono, *Chem Eng Sci*, **2022**, *262*, 118009.
- [5] A. I. Frenkel, C. W. Hills, R. G. Nuzzo, *J. Phys. Chem. B* **2001**, *105*, 12689–12703.
- [6] S. Alayoglu, P. Zavalij, B. Eichhorn, Q. Wang, A. I. Frenkel, P. Chupas, *ACS Nano* **2009**, *3*, 3127–3137.
- [7] G. Zhang, Z.-G. Shao, W. Lu, F. Xie, H. Xiao, X. Qin, B. Yi, *Appl. Catal. B* **2913**, *132–133*, 183–194.
- [8] A. Frenkel, *Z. Krist.* **2007**, *222*, 605–611.
- [9] S. Nagamatsu, T. Arai, M. Yamamoto, T. Ohkura, H. Oyanagi, T. Ishizaka, H. Kawanami, T. Uruga, M. Tada, Y. Iwasawa, *J. Phys. Chem. C* **2013**, *117*, 13094–13107.
- [10] H. A. Gasteiger, S. S. Kocha, B. Sompalli, F. T. Wagneret, *Appl. Catal. B Environ.* **2005**, *56*, 9–35.
- [11] M. Shao, A. Pele, K. Shoemaker, *Nano Lett.* **2011**, *11*, 3714–3719.
- [12] L. R. Ruhaak, E. Steenvoorden, C. A. M. Koeleman, A. M. Deelder, M. Wuhler, *Proteomics* **2010**, *10.12*, 2330–2336.
- [13] S. Campisi, M. Schiavoni, C. E. Chan-Thaw, A. Villa, *Catalysts* **2016**, *6*, 185.
- [14] T. E. Fischer, S. R. Kelemen, *J. Catal.*, **1978**, *53*, 24–34.
- [15] J. C. Summers, K. Baron, *J. Catal.*, **1979**, *57*, 380–389.
- [16] M. Saito, H. Otsuka, *J. Jpn. Soc. Colour Mater.* **2011**, *84*, *1*, 12–17.
- [17] J. Wan, G. Fang, H. Yin, X. Liu, D. Liu, M. Zhao, W. Ke, H. Tao, Z. Tang, *Adv. Mater.* **2014**, *26*, 8101–8106.
- [18] T. Fujigaya, C. Kim, Y. Hamasaki, N. Nakashima, *Scientific reports* **2016**, *6.1*, 1–10.
- [19] S. Yamazaki, M. Asahi, T. Ioroi, *Electrochim. Acta.* **2019**, *297*, 725–734.
- [20] S. Yamazaki, M. Asahi, N. Taguchi, T. Ioroi, *J. Electroanal. Chem.* **2019**, *848*, 113321.
- [21] G. E. Ryschkewitsch, E. R. Birnbaum, *Inorganic Chemistry*, 1965, *4.4*, 575–578.
- [22] M. F. Frederick, E. S. Lewis *J. Am. Chem. Soc.*, 1958, *80*, 4296–4299.
- [23] Y. Zhang, L. Liu, C. Sun, Y. Du, Y. Zhou, Q. Xie, *J Alloys Compd*, **2021**, *888*, 161564.
- [24] H. H. Ingelsten, R. Bagwe, A. Palmqvist, M. Skoglundh, C. Svanberg, K. Holmberg, D. O. Shah,

- J Colloid Interface Sci*, **2001**, *241*, 104–111.
- [25] A. R. Tao, S. Habas, P. Yang, *small*, **2008**, *4*, 310–325.
- [26] T. Teranishi, R. Kurita, M. Miyake, *J Inorg Organomet Polym Mater* 2000, *10*, 145–156.
- [27] T. S. Ahmadi, Z. L. Wang, T. C. Green, A. Henglein, M. A. El-Sayed, *Science* 1996, *272*, 1924–1925.
- [28] Sumitomo Seika Chemicals Co Ltd, B. Hori, M. Hishiike, H. Itsuda, JPH0733779A.
- [29] M. D. Taylor, L. R. Grant, C. A. Sands, *J. Am. Chem. Soc.* **1955**, *77*, 1506–1507.
- [30] T. Honma, H. Oji, S. Hirayama, Y. Taniguchi, H. Ofuchi, M. Takagaki, *AIP Conf., Proc.* **2010**, *1234*, 13–16.
- [31] H. Oji, Y. Taniguchi, S. Hirayama, H. Ofuchi, M. Takagaki, T. Honma, *J. Synchrotron Rad.* **2012**, *19*, 54–59.
- [32] B. Ravel, M. Newville, *J. Synchrotron Radiat.* **2005**, *12*, 537–541.

**Chapter 4. Effects of the Pt Shell Thickness on the Oxygen Reduction
Reaction on a Well-Defined Pd@Pt Core-Shell Model Surface**

4.1. Introduction

I have been developing Pd@Pt core-shell catalysts, which are electrocatalysts for cathodes, for the purpose of expanding the use of PEFCs. In order to improve the productivity, which is a problem of existing synthesis methods such as Cu-UPD method, I worked on the development of flow synthesis method of core-shell catalysts and succeeded in the flow synthesis of Pd@Pt NPs.¹ As a result of further optimization of flow synthesis conditions, Pd@Pt_{1ML}/C with a uniform monoatomic layer of Pt shell was successfully synthesized. This catalyst showed catalytic activity comparable to that of the Cu-UPD method synthesis, confirming that this flow method is a possible alternative to the Cu-UPD method for the synthesis of core-shell catalysts. This study is described in Chapter 3.

Having successfully achieved flow synthesis of highly active Pd@Pt_{1ML}/C catalysts, I decided to subsequently elucidate the factors behind the high activity of the core-shell catalysts. It has been reported that Pd@Pt core-shell catalysts, with Pd as the core metal, not only have higher Pt weight activity but also higher Pt atomic efficiency compared to Pt catalysts.²⁻⁶

There have been several reports concerned with the effect of Pt thickness on the ORR activities of Pd@Pt core-shell NPs and the Pt-deposited Pd(111) surface.⁷⁻⁹ Choi et al. have found that the ORR activity of Pd@Pt core-shell NPs depends strongly on the Pt shell thickness; Pd@Pt NPs with a Pt shell thickness of 0.94 nm show improved specific activity because of the faster reduction of OH_{ad} with lower bonding strength formed on the surface compared to Pt/C catalysts and Pd@Pt NPs with a different Pt shell thickness.⁷ However, it is not clear the reason why the adsorption energy of OH on Pt depends on the thickness of the Pt shell. Bando et al. have demonstrated that the ORR activity of both Pt_{0.6nm}/Pd(111) and Pt_{1.2nm}/Pd(111) is 4 times that of clean Pt(111).⁸ They concluded that the activity enhancement of Pt/Pd(111) depended on the compressive surface strains of the topmost Pt(111) lattice induced by a lattice mismatch between the topmost Pt(111) and substrate Pd(111) lattices.⁸ The effect of geometric structural changes on the ORR process has not been clearly articulated. Wang et al. have examined ORR activity over Pd@Pt/C catalysts with Pt shells of 1, 2, and 3 monolayers (MLs); they have used DFT calculations with a nanoparticle model to demonstrate that the enhancement of specific activity (SA) is largely attributable to a compressive strain effect. Their calculations have revealed the effect of nanosize-induced surface contraction on facet-dependent oxygen binding energy (BE).⁹ Moreover, they have reported that the ORR activity of Pt_{1ML}/Pd(111) is higher than that of Pt(111); they have explained that the improvement in catalytic activity may be related to modification of the electronic properties of Pt 5d due to the electronic interaction between Pt and Pd.¹⁰ This change results in faster hydrogenation of O, which can decrease the strength of Pt-OH adsorption and increase the ORR kinetics. However, they have also shown that the reason for the

improved ORR activity of the Pd@Pt/C catalyst is the increase of the surface roughness on the atomic scale and the low coordination of some Pt atoms.¹¹ There is agreement that the Pd@Pt core-shell structure improves ORR activity by weakening the adsorption of OH, a reaction intermediate, onto Pt. However, the reason for the weakening of OH adsorption onto Pt has not always been clear.

By the way, as I have mentioned, flow synthesis allows precise control of the structure of the resulting particles. Moreover, since it is a versatile process, core-shell nanoparticles of various core metals can be easily prepared by using other metal precursors instead of Pd precursors and by selecting appropriate reducing agents. Alloy cores can also be synthesized by using multiple metal precursors. Accordingly, by utilizing the flow synthesis method, I can expect to synthesize more active (i.e., Pt atom efficient) core-shell NPs with appropriate particle size, surface structure such as Pt shell thickness, and core element type. To achieve this goal, it is necessary to clarify the correlation between catalyst structure and catalytic activity, and to elucidate the factors that cause ORR activity. Therefore, I decided to investigate the relationship between Pt thickness and ORR activity and between Pt thickness and surface structure.

In this chapter, I prepared a model surface of a Pd@Pt core-shell by depositing Pt onto a Pd rod substrate at various thicknesses. I then investigated the influence of the Pt thickness on the electronic state, the surface structure, and the ORR activity. I found that the electronic state of Pt changed as a function of the Pt thickness and that there was a good correlation between the electronic state and the ORR activity. I then performed DFT calculations to examine how the electronic state of Pt affected the ORR process.

4.2. Results and Discussion

4.2.1. Electronic structure of Pt relative to Pd@Pt core-shell model surface

I used XPS to investigate the electronic state of Pt on the Pd@Pt model surfaces of Pt deposited on a Pd rod substrate. The preparation method for Pd@Pt model surfaces is described in the experimental section. Figure 1A shows XPS spectra of Pt 4f on the surfaces with 0.5 to 4 ML of Pt deposited. Figure 1B shows the BE of Pt 4f_{7/2} as a function of Pt shell thickness (0.5 to 4 ML). For comparison, Figure 1B shows the XPS result obtained for a Pt rod as black dotted lines. For a Pt deposition of 0.5 ML, the Pt 4f_{7/2} peak occurred at 70.7 eV. The BE in this case was 0.2 eV lower than the BEs of the Pt rod and Pt(111) (70.9 eV).¹² This means that charge transfer occurred from the Pd substrate to the Pt layer,^{13,14} and the deposited Pt was in an anionic (Pt^{δ-}) electronic state. The fact that the electronic state of the Pt surface at 1 ML did not change from that of Pt at 0.5 ML indicated that the deposited Pt maintained its anionic state. However, when the amount of Pt deposited was increased to 2 ML, the Pt 4f_{7/2} peak shifted to 70.8 eV. Moreover, when 3 and 4 MLs of Pt were deposited, the Pt 4f_{7/2} peak occurred at 70.9 eV, which was almost the same as the BEs of the Pt rod and Pt(111). There was a clear correlation between the charge transfer to the Pt shell layer from the Pd substrate and the Pt shell thickness (Figure 1B). The magnitude of the negative charge on the Pt decreased as the amount of deposited Pt increased when the latter exceeded 2 ML, and when the latter exceeded 3 ML, the electronic state of Pt was almost completely unaffected by the electron transfer from the Pd substrate and became identical to that of the bulk Pt. Radosavkic et al. have reported the results of a core-level photoemission study of the growth of Pt on Pd(111).¹⁵ They have demonstrated that the BE of the Pt 4f_{7/2} surface peak measured by photoelectron spectroscopy is constant at 70.5±0.03 eV if the deposited Pt is less than 1 ML. In contrast, the BE of the Pt 4f_{7/2} surface peak shifts to higher energy with increasing Pt coverage when the Pt coverage exceeds 1 ML, and above 2 ML it remains constant at 70.75±0.03 eV, which is equal to the BE of the bulk Pt. The trend of their results is similar to that of the Pt shells obtained in this study and indicates that the Pt was negatively charged up to a deposition of 1 ML. However, Radosavkic et al. have reported that at a Pt deposition less than 1 ML, a surface alloy is formed on top of the first two layers because of interdiffusion of Pt.¹⁵ Pure Pt layers are then formed with 2 ML or more of deposition. Moreover, Bando et al. have investigated the crystal structure of the topmost surface of the deposited Pt on Pd(111).⁸ They have reported that the deposited Pt grows epitaxially on a Pd(111) substrate, but at high substrate temperatures, the deposited Pt forms a bimetallic surface by thermal diffusion into the Pd atoms of the substrate. Since I deposited Pt on the Pd rods at room temperature, I believe that formation of a surface alloy by thermal diffusion of Pt was suppressed, but the surface state of the deposited Pt needs to be clarified.

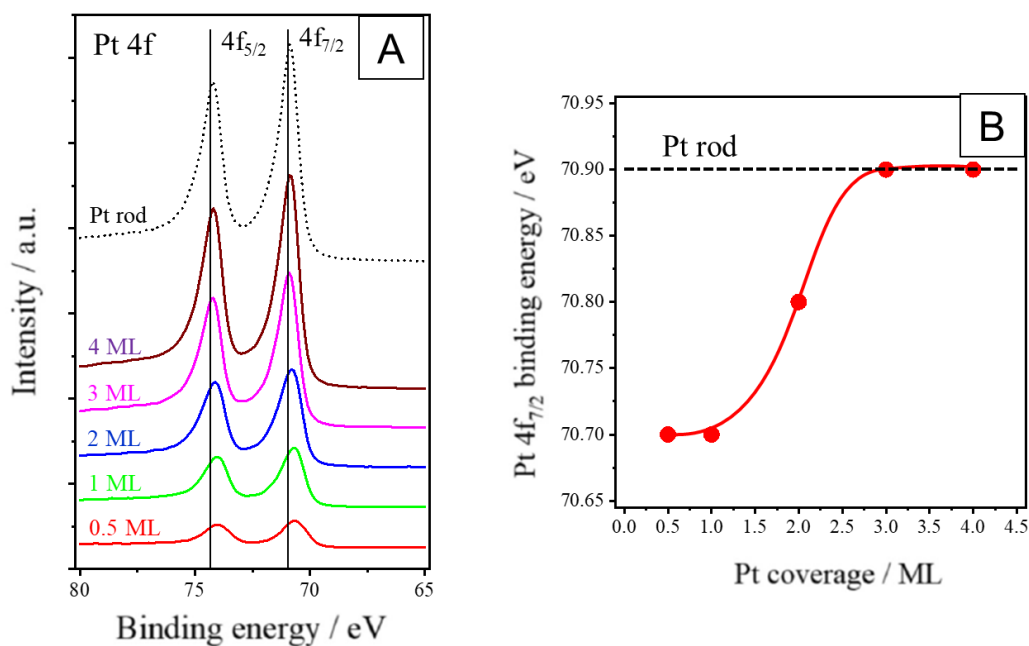


Figure 1. Pt 4f XPS spectra of Pd@Pt model surface (A) and Pt 4f_{7/2} peak position of Pd@Pt model surface as a function of Pt coverage (B). The dotted line is BE of Pt rod.

4.2.2. Pt surface state of Pd@Pt core-shell model

Next, I performed XAFS measurements on Pt-deposited Pd rods to investigate the crystal structure of the deposited Pt. Figure 2, and Table 1 shows EXAFS data and theoretical fits of the Pt L₃ edge on the Pd@Pt model surface. EXAFS data were analyzed by fitting Pt edge data to account for homometallic (Pt–Pt, Pd–Pd) and heterometallic (Pt–Pd, Pd–Pt) interactions.¹⁶ The Pt–Pt and Pt–Pd coordination numbers (CNs) for the samples with 1 ML of deposited Pt were 1.6 and 6.1, respectively, which were quite different from the theoretical values for a single layer of Pt shell (CN_{Pt–Pt} : 6, CN_{Pt–Pd} : 3). This result strongly suggests that Pt deposited on Pd rods diffuses between Pd atoms to form a bimetallic surface. In the present XAFS measurements, I believe that thermal diffusion of Pt atoms into the Pd rod occurred because the sample surface was heated locally during the XAFS measurement. In contrast, the Pt–Pt coordination number increased and the Pt–Pd coordination number decreased as the amount of deposited Pt increased. The fact that the CNs of the Pt–Pd and Pt–Pt were almost in agreement with the theoretical values for a single layer Pt shell at a Pt deposition of 4 ML (CN_{Pt–Pt} : 5.9, CN_{Pt–Pd} : 2.5) indicated that a considerable amount of Pt thermally diffused into the Pd.^{8,15}

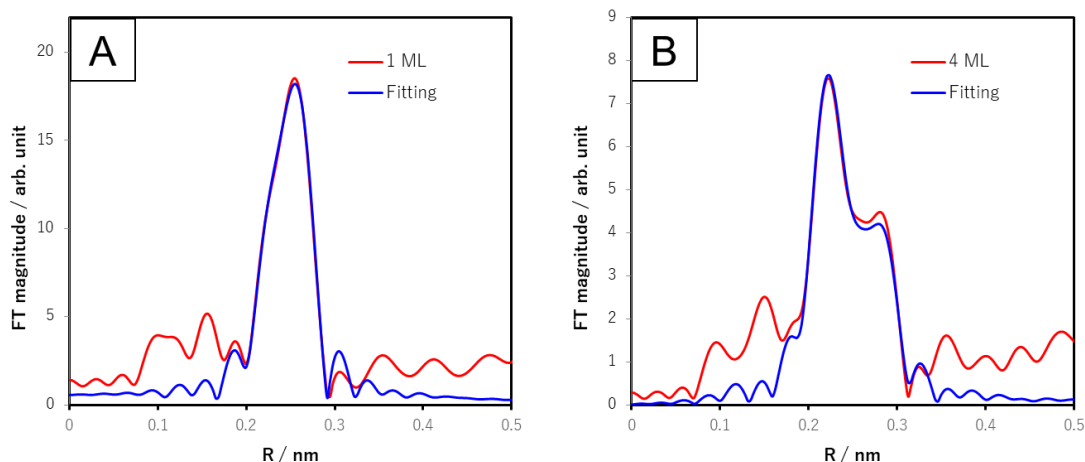


Figure 2. Fourier transform of the data (red lines) and first-shell fit (blue line) of Pt L₃ edges from A) 1 ML and B) 4 ML.

Table 1. EXAFS fit parameters of Pd@Pt model surface.^{a)}

Sample	Shell	CN ^{b)}	S ₀ ^{2,c)}	R ^{d)} [nm]	σ ^{2,e)} x 10 ⁻² [nm ²]	R _{factor} ^{f)}
Pt foil	Pt–Pt	12	0.82	0.28 ± 0.00	0.0044 ± 0.0002	0.001
1 ML	Pt–Pt	1.6	0.82	0.27 ± 0.05	0.0034 ± 0.0039	0.005
	Pt–Pd	6.1	0.82	0.27 ± 0.01	0.0049 ± 0.0021	
4 ML	Pt–Pt	5.9	0.82	0.27 ± 0.02	0.0057 ± 0.0016	0.008
	Pt–Pd	2.5	0.82	0.27 ± 0.02	0.0030 ± 0.0023	

a): k^3 : k-range = 0.3–1.2 nm⁻¹ and 0.3–1.4 nm⁻¹ for Pt foil and Pd@Pt model surface, respectively. r-range = 0.17–0.33 and 0.19–0.33 nm for Pt foil and Pd@Pt model surface, respectively. b): Coordination number. c): Intrinsic loss factor. d): Bond length. e): Debye-Waller factor. f): Goodness-of-fit index.

I therefore investigated the state of the Pt shell on the surface of the Pd rods by conducting CO adsorption experiments using infrared reflection absorption spectroscopy (IRAS). Figure 3 shows the IRAS spectra of the surfaces with 0.5 to 4 MLs of Pt deposited on the Pd rod exposed to CO at room temperature. Figure 3 also shows the CO adsorption peaks of Pt (111) and Pd (111). Two peaks were observed at 2083 and 1873 cm⁻¹ on a 0.5 ML Pt surface; the 2083 cm⁻¹ peak was assigned to the top site on the Pt surface and the 1873 cm⁻¹ peak to CO adsorbed on the bridge site of Pt.¹⁷ In addition, a peak of CO adsorbed to the Pd bridge site was apparent at around 1920 cm⁻¹.¹⁸ This result clearly shows that the surface of the Pd rod is partially exposed. On the 1 ML surface, CO adsorption onto Pt was observed at almost the same peak position as it was on the 0.5 ML surface, but the fact that there

was no peak associated with CO adsorption onto the Pd surface showed that the entire surface of the Pd rod was covered with 1 ML of deposited Pt. Since it has been reported that CO is preferentially adsorbed onto Pd sites on Pt-Pd mixed alloy surfaces,¹⁵ I concluded that Pt-Pd alloys were not formed by room-temperature deposition. As the ML of the Pt increased, the peak position of the CO adsorbed on the top site shifted to a higher wavenumber and became almost the same as the peak position of Pt(111) with 3 ML of deposited Pt. In contrast, the peak position of the CO bridge site shifted to a lower wavenumber and became the same peak position of Pt(111) at 4 ML of deposited Pt. I believe that these shifts in the adsorption position of CO are influenced by changes in the surface Pt shell electronic state, as shown in Figure 1.¹⁹

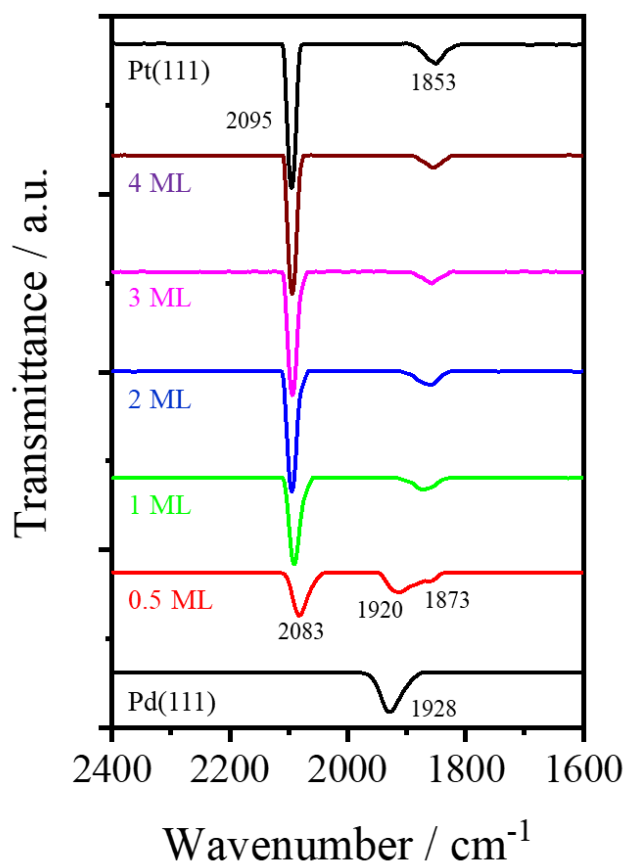


Figure 3. IRAS spectra of CO adsorbed on the Pd@Pt model surface with various Pt shell thickness, Pt(111), and Pd(111) surfaces.

Figure 4 shows the IRAS spectra of the surface of the Pd rod with 1 ML of deposited Pt after heat treatment at various temperatures (27 to 400 °C) and then exposure to CO. As the heating temperature increased, the adsorption peak of CO on Pd, which was not observed at room temperature, was clearly observed. Moreover, it was clear that the CO adsorption positions on Pt (2075 cm^{-1} on the top site, 1863 cm^{-1} on the bridge site) and Pd (1903 cm^{-1} on the bridge site) changed significantly on the heat-treated surface. These changes strongly suggested that the interdiffusion of Pt and Pd was accelerated by heat and formed a surface alloy above room temperature. I thus discovered that Pt deposited on Pd rods diffused into the Pd interior to form a Pd-Pt alloy when treated at high temperatures, whereas the Pt forms a core-shell structure covering the Pd rod surface when deposited near room temperature. This result supports the thermal diffusion of Pt into the Pd rod in the XAFS measurements described earlier.

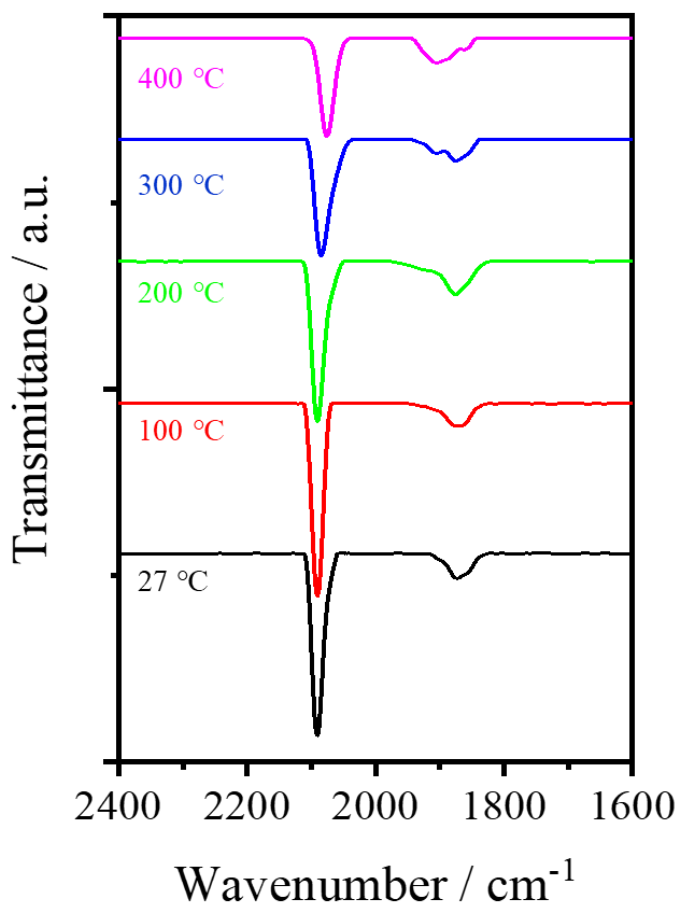


Figure 4. IRAS spectra of CO adsorbed on the Pd@Pt model surface (1 ML) with heated various temperatures (27 to 400 °C).

4.2.3. ORR activity evaluation of Pd@Pt core-shell model

The ORR activities of the Pd@Pt model surface with different Pt thicknesses (0.5 to 4 MLs) and a commercial Pt/C catalyst were evaluated for comparison by the rotating electrode method. Details of the evaluation method are described in the experimental section. Figure 5 shows the results of the kinetic current (I_k) evaluation at 0.9 V and 1600 rpm for each Pd@Pt model surface and Pt/C catalyst. Table 2 summarizes the I_k and specific activity (SA) estimated from the results of the evaluation of the ORR activity of these samples. The close agreement between the SA values of the Pt/C catalyst and the Pt rod suggests that this measurement method can be used to evaluate the ORR activity of the Pd@Pt model surface. The fact that the SA of the Pd@Pt model surfaces with Pt deposits of 0.5 ML and 1 ML were similar and 2.6 times the SA of the Pt/C and Pt rod strongly indicated that the atomic efficiency of Pt in the core-shell structure was enhanced by the effect of the Pd substrate. The SA decreased with increasing numbers of Pt MLs, and the SA with more than 3 ML was almost equivalent to those of the Pt/C catalyst and Pt rod.

Figure 6 shows the SA of Pd@Pt model surfaces as a function of Pt shell thickness (0.5 to 4 MLs). It was apparent that the relationship between the SA of Pt and the ML of Pt was the exact opposite of the relationship between the BE of Pt and the ML of Pt (Figure 1B). The more negatively charged the Pt, the higher the ORR activity. I therefore further investigated the effect of catalytic activity and Pt electronic state, i. e., Pt negative charge, on the ORR reaction mechanism.

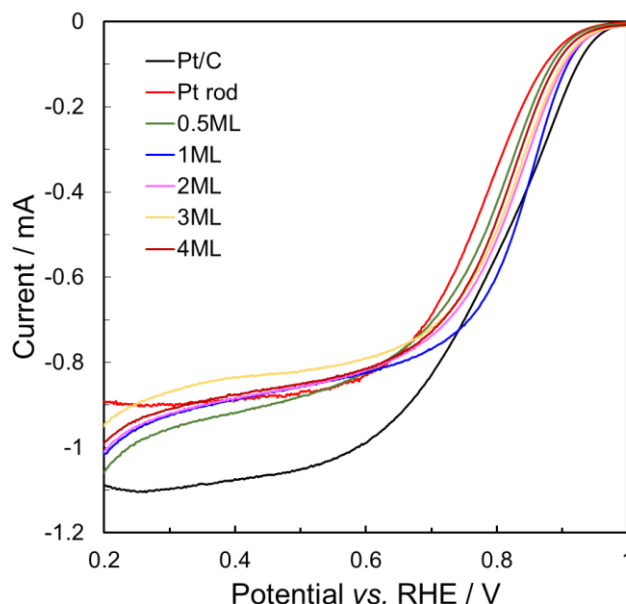
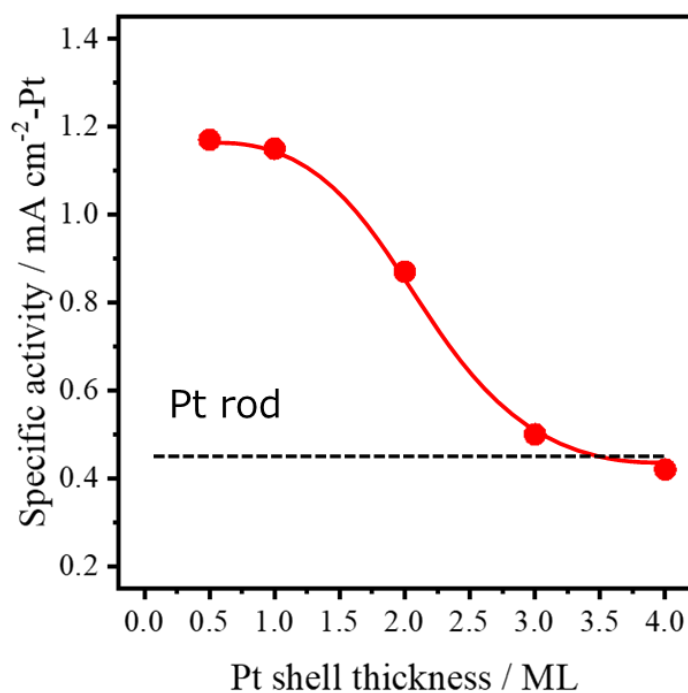


Figure 5. ORR polarization curves of the various Pd@Pt model surface, Pt/C catalyst, and Pd rod in O₂-saturated 0.1 M HClO₄ at a scan rate of 10 mV s⁻¹ and rate of 1600 rpm.

Table 2. ORR activities of the Pd/C catalyst, Pd rod, and Pd@Pt model surfaces.

Pt ML	Surface area of Pt ^{a)} [cm ²]	Kinetic current ^{b)} [mA]	Specific activity [mA cm ⁻² -Pt]
Pt/C	0.52	0.23	0.44
Pt rod	0.13	0.06	0.46
0.5	0.06	0.07	1.17
1	0.13	0.15	1.15
2	0.15	0.13	0.87
3	0.18	0.09	0.50
4	0.19	0.08	0.42

a): Pt surface area of model surfaces were estimated from the amount of CO adsorption at room temperature. b): The kinetic current for the ORR is obtained at 0.9 V and 1600 rpm.

**Figure 6.** Specific current densities of Pd@Pt model surfaces as a function of Pt shell thickness.

4.2.4. DFT calculations for Pd@Pt surfaces

The effect of negatively charged Pt on the ORR reaction was examined by computational chemistry. First, I constructed a three-layer periodic slab model where one layer contains 16 atoms (Figure 7) to confirm the electronic state of Pt. Hirshfeld atomist charge²⁰ of Pt atoms of pure Pt(111) surface was computed to be -0.015 whereas that of Pd@Pt_{1ML} was computed to be -0.073. This result

supports the experimental result (XPS) that Pt in Pd@Pt_{1ML} is more negatively charged than pure platinum.

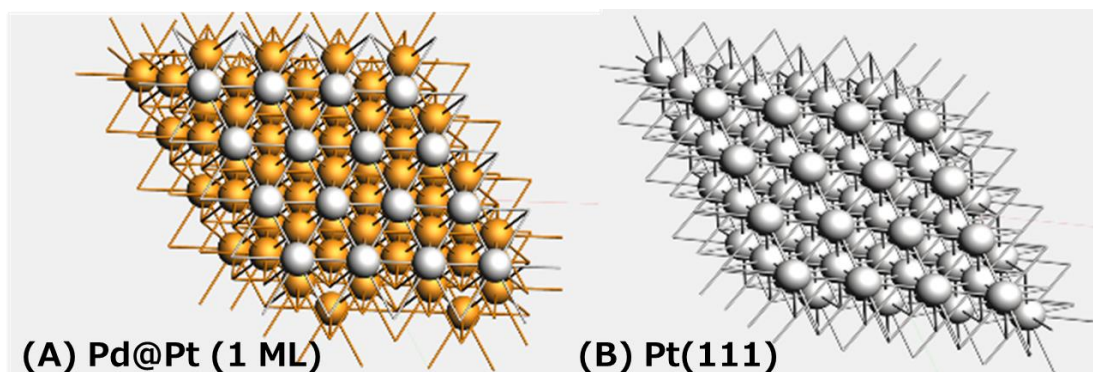


Figure 7. (A) Top view of Pd@Pt_{1ML} and (B) pure Pt catalysts. Color description: Pt: white, Pd: brown.

Next, I performed preliminary calculations on the energy barriers of the rate-determining step of ORR reaction using simple cluster models. Pt and Pd@Pt surfaces were modelled using a cluster model approach that simulated the Pt(111) surface. The models consisted of three layers. Each layer consisted of 9, 10, and 9 atoms. Figure 8 shows their optimized structures. It has previously been shown that such a cluster model gives results for the geometry and bond energies that are within experimental uncertainty.²¹ The average Mulliken charge of the top layer of Pt atoms was computed to be -0.21 for a pure Pt_{9,10,9} cluster and -0.47 for a Pt₉-Pd_{10,9} cluster (Table 3). This result is consistent with the Hirshfeld atomist charge calculated earlier and with the experimentally observed trend.

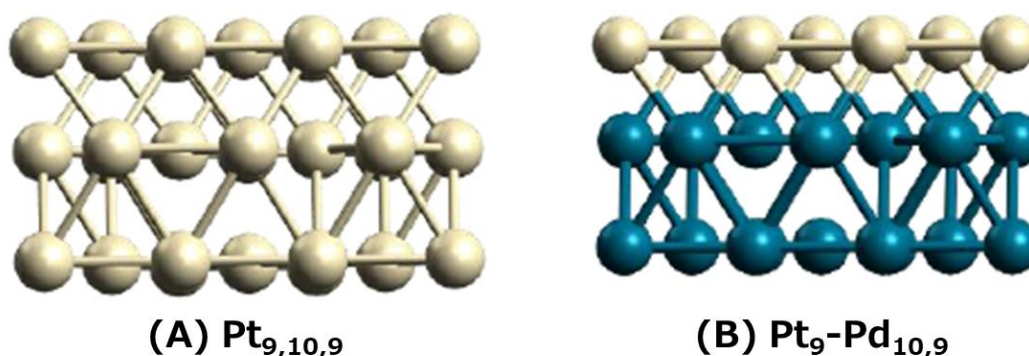
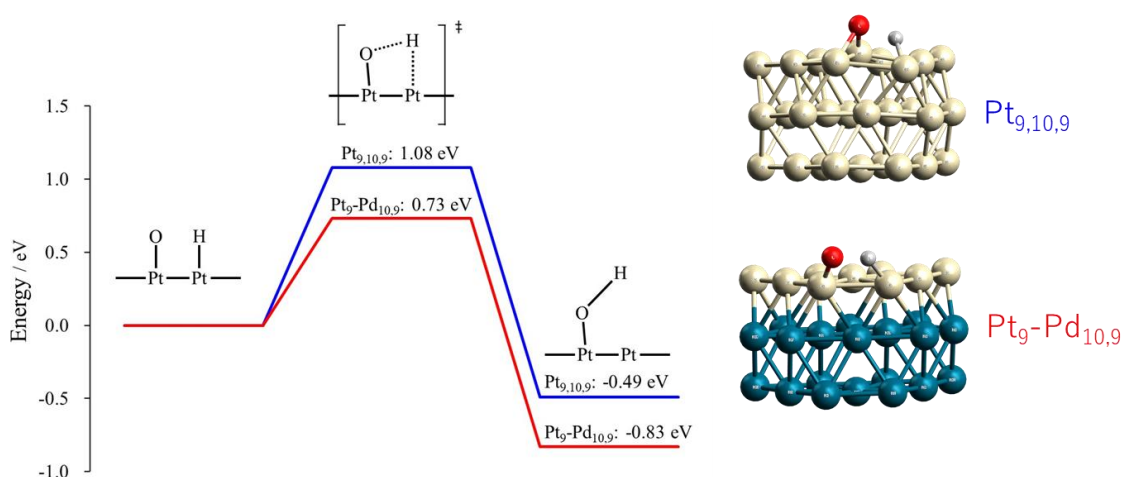


Figure 8. Structure of three layers metal clusters. (A) Pt_{9,10,9} (indices indicates the number of atoms per layer) (B) Pt₉-Pd_{10,9}. Color description: White: Pt, Cyan: Pd.

Table 3. Mulliken charge of surface Pt atoms for Pt_{9,10,9} and Pt₉-Pd_{10,9}

Pt _{9,10,9}	Mulliken charge	Pt ₉ -Pd _{10,9}	Mulliken charge
20 Pt 0.017512 -0.109709	0.017512	20 Pt -0.345100 -0.089170	-0.3451
21 Pt 0.017833 -0.107257	0.017833	21 Pt -0.343419 -0.067944	-0.34342
22 Pt -0.643392 0.224124	-0.64339	22 Pt -0.575752 0.163840	-0.57575
23 Pt -0.648272 0.225382	-0.64827	23 Pt -0.576348 0.139563	-0.57635
24 Pt -0.373647 -0.193140	-0.37365	24 Pt -1.090036 -0.220945	-1.09004
25 Pt -0.015054 0.130630	-0.01505	25 Pt -0.328255 0.143302	-0.32826
26 Pt -0.147340 0.269143	-0.14734	26 Pt -0.314639 0.325203	-0.31464
27 Pt -0.149992 0.265646	-0.14999	27 Pt -0.313726 0.307753	-0.31373
28 Pt -0.014894 0.136706	-0.01489	28 Pt -0.324832 0.133370	-0.32483
Average	-0.21747	Average	-0.46801

Next, barrier heights related to ORR were calculated for both clusters. The ORR consists of several elementary reaction steps, and a previous study has reported that the process of O-H formation is the rate-determining step.²² I thus focused on this step for the comparison of ORR activities of both clusters. Figure 9 shows potential energy surfaces for the O-H formation obtained from DFT calculations. The height of the barrier to the reaction was higher for the pure Pt cluster. The DFT calculations thus suggested that a more negatively charged Pt surface lowered the barrier height associated with the formation of O-H. This result was consistent with the trend of the experiment (ORR activity evaluation).

**Figure 9.** Potential energy surface of the OH formation step

4.3. Conclusion

In this chapter, I performed various evaluations using Pd@Pt model surfaces. The results showed that the electronic state of Pt on the Pt@Pd core-shell catalyst was significantly dependent on the film thickness, with the smaller film thickness being more negatively charged. The more negatively charged Pt also exhibited higher ORR activity. These experimental results were supported by computational chemistry results. The reason for the higher ORR activity of the 1 ML Pd@Pt catalyst could be attributed to the fact that the electron transfer from Pd to Pt lowers the activation energy of the rate-determining step of the ORR, the activation energy. The results suggest that the atomic efficiency of Pt has been improved. These findings are useful for future development of new core-shell catalysts with higher activity (i.e., Pt atom efficiency).

4.4. Experimental

4.4.1. Preparation of the Pd@Pt Model Surface

The preparation of the Pt-deposited Pd rod sample was performed in an ultra-high-vacuum chamber (UHV, $<5 \times 10^{-10}$ Torr) of XPS or IRAS apparatus. A schematic diagram of the preparation is shown in Figure 10. Pd rod substrate (DRE-PDD, 4 mm diameter) was cleaned by cycles of Ar⁺ sputtering and annealing at 927 °C. The cleanliness of the Pd rod surface was verified by means of XPS or Auger electron spectroscopy (AES). The Pd@Pt model surface was prepared by depositing Pt on a clean Pd rod surface at room temperature by evaporation from a Pt rod (2.0 mm diameter, 99.98% purity, Nilako Co., Ltd.) using an electron beam evaporator (EBE). The Pt deposition was carried out under the conditions of a filament current of 2.0 A, an applied voltage of 900–930 V, an emission current of 22 mA, and a flux current of 10 nA. The Pt deposition rate was 0.03 MLmin⁻¹, which was estimated using a quartz microbalance. The deposition amount of Pt was controlled by the deposition time at a constant flux of 10 nA. The 1 ML corresponded to the surface covered by one layer (0.277 nm thickness) of Pt atoms.

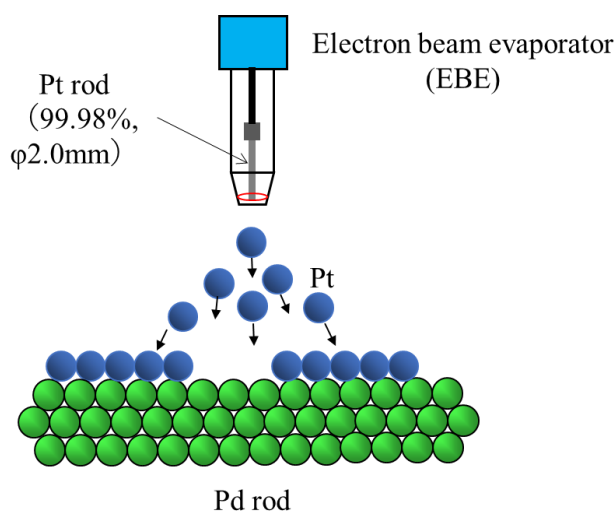


Figure 10. Schematic diagram of Pd@Pt model surface preparation

4.4.2. XPS Measurements

The XPS experiments were performed on a UHV instrument, whose details were reported in elsewhere.²³ The spectra were referenced to the Fermi level, which shows the Pt 4f_{7/2} peak at 70.9 eV binding energy for clean Pt(111) single crystal. After Pt deposition onto the Pd rod substrate, the sample was transferred to the XPS analysis chamber, and the Pd 3d and Pt 4f peaks were measured to obtain the electronic state of Pt and Pt 4f_{7/2}/Pd 3d_{5/2} peak area ratio. The Pt 4f_{7/2}/Pd 3d_{5/2} peak area

ratios for 0.5, 1, 2, 3, 4 ML Pt/Pd substrate were obtained to be 0.07, 0.16, 0.37, 0.68, 1.10, respectively. By checking these ratios, we confirmed that Pt was deposited on the Pd surface to the specified amount.

4.4.3. XAFS Measurements

All measurements were performed at the Super Photon ring-8 GeV (SPring-8) using Beam Line BL39XU. The sample was sprayed with Ar (2 L/min) for protection and measured at the Pt L₃ edge (11,564 eV) at room temperature using a Si(111) double crystal monochromator in a Fluorescence mode. Details on data processing and analysis were described in capture 2.¹

4.4.4. IRAS Measurements

The equipment used for the IRAS experiment is the same as described in elsewhere.²⁴ After Pt deposition onto the Pd rod substrate, the sample was checked by AES that Pt was deposited on the Pd surface to the specified amount, and then the CO adsorption experiments were carried out with CO (99.999% pure) at 0.5 to 20 L (1 L=10⁻⁶ Torr) and a sample temperature of 27 to 227 °C.

4.4.5. Electrochemical Measurements

Electrochemical experiments were carried out in a three-electrode cell at 25 °C using a BAS ALS-760E electrochemical workstation with a BAS RRDE-3A rotation system. The Pd rod and Pd@Pt model surfaces were mounted in the disk replaceable electrode and used as the working electrode. Details of the electrochemical measurement method were described in Capture 2.¹ The ORR polarization curves measured at a disk rotation rate of 1600 rpm. The kinetic current I_k for the ORR was obtained at 0.9 V using Equation (1).²⁵

$$I_k = I_d / (I_d - I) \quad (1)$$

where I is the experimentally measured current at 0.9 V, I_d is the diffusion limited current at 0.3 V on the experimentally measured current. The specific activity for the ORR was calculated by dividing I_k by Pt surface area of Pd@Pt model surface, and Pt rod. Pt/C was evaluated using the same method as in capture 2.¹ I_k was obtained using equation (1) as for the model surface. Pt surface area of Pt/C was calculated on the basis of the charges associated with the adsorption of hydrogen in the region 0.05–0.4 V after a double-layer correction with a reference value of 210 $\mu\text{C cm}^{-2}$ for the adsorption of a monolayer of hydrogen from the Pt surfaces. The surface area of Pt on the Pd@Pt model surfaces with various Pt shell thickness were estimated from the IRAS peak area for CO adsorbed on the Pt surface.

The IRAS peak area of CO adsorbed on the Pt rod surface was assumed to be the surface area of the Pt rod (0.13 cm^2). The Pt surface area of each Pd@Pt model surface was estimated from the ratio of the IRAS peak area for CO adsorbed on Pt on the model surface and the that on the Pt rod.

4.4.6. Computational Details

To model pure Pt and Pd@Pt catalysts, we constructed three-layer periodic slab model where one layer contains 16 atoms in the unit cell (See Figure 7). For modelling pure Pt(111), the surface was constructed from bulk Pt structure. For Pd@Pt core-shell, Pd(111) surface was firstly constructed from bulk Pd and then surface layer atoms were replaced by Pt atoms. For periodic DFT calculations, I employed the BAND engine in Amsterdam Modeling Suite (AMS).²⁶ For DFT calculations I employed revised Perdew-Burke-Ernzerhof (PBE) functional^{27,28} with Grimme's dispersion.²⁹ As for the basis sets, I used the double- ζ plus polarization basis sets (DZP) where the large frozen core approximation was taken into account. Numerical quality was set to default values of AMS. To account for relativistic effects, the ZORA method was employed.³⁰ Geometry optimization were carried out for two catalysts where we the optimizations were terminated if the default convergence criteria of AMS suites were met.

For a preliminary study with a simple cluster model, see below. Three layers cluster model of Pt(111) was taken from the previous study.²¹ Pd@Pt core-shell was modeled by replacing lower two layer Pt atoms of the above cluster by Pd atoms. For the DFT calculations, I employed M06-L functional.³¹ For Pt and Pd atoms, core electrons were represented by the Hay-Wadt relativistic effective-core potential,³² and for the valence electrons, the revised version of basis sets for the LANL effective core potentials augmented with the f--polarization function was used.^{33,34} For other atoms, 6-31G(d,p) basis sets was used. To speed up DFT calculations, density fitting approximation which enables the performance improvement with minimal loss of accuracy was used.^{35,36} Geometry optimizations were performed with Gaussian 16 quantum chemistry package.³⁷ Frequency computations for the optimized geometries were carried out to check the nature of stationary points.

4.5. References

- [1] Y. Hashiguchi, F. Watanabe, T. Honma, I. Nakamura, S. S. Poly, T. Kawaguchi, T. Tsuji, H. Murayama, M. Tokunaga, T. Fujitani, *Colloids Surf. A* **2021**, *620*, 126607.
- [2] J. Zhang, M. B. Vukmirovic, Y. Xu, M. Mavrikakis, R. R. Adzic, *Angew. Chem. Int. Ed.* **2005**, *44*, 2132–2135.
- [3] R. R. Adzic, J. Zhang, K. Sasaki, M. B. Vukmirovic, M. Shao, J. X. Wang, A. U. Nilekar, M. Mavrikakis, J. A. Valerio, F. Uribe, *Top. Catal.* **2007**, *46*, 249–262.
- [4] K. Sasaki, H. Naohara, Y.-M. Choi, Y. Cai, W.-F. Chen, P. Liu, R. R. Adzic, *Nat. Commun.* **2012**, *3*, 1–9.
- [5] K. Gong, Y.-M. Choi, M. B. Vukmirovic, P. Liu, C. Ma, D. Su, R. R. Adzic, *Z. Phys. Chem.* **2012**, *226*, 1025–1038.
- [6] K. Cao, Q. Zhu, B. Shan, R. Chen, *Sci. Rep.* **2015**, *5*, 8470.
- [7] R. Choi, S. I. Choi, C. H. Choi, K. M. Nam, S. I. Woo, J. T. Park, S. W. Han, *Chem. Eur. J.* **2013**, *19*, 8190–8198.
- [8] Y. Bando, Y. Takahashi, E. Ueta, N. Todoroki, T. Wadayama, *J. Electrochem. Soc.* **2015**, *162*, F463–F467.
- [9] J. X. Wang, H. Inada, L. Wu, Y. Zhu, Y. Choi, P. Liu, W.-P. Zhou, R. R. Adzic, *J. Am. Chem. Soc.* **2009**, *131*, 17298–17302.
- [10] F. H. B. Lima, J. Zhang, M. H. Shao, K. Sasaki, M. B. Vukmirovic, E. A. Ticianelli, R. R. Adzic, *J. Phys. Chem. C* **2007**, *111*, 404–410.
- [11] J. Zhang, Y. Mo, M. B. Vukmirovic, R. Klie, K. Sasaki, R. R. Adzic, *J. Phys. Chem. B* **2004**, *108*, 10955–10964.
- [12] C. D. Wagner, W. M. Riggs, L. E. Davis, J. F. Moulder, G. E. Muilenberg, *Handbook of X-ray Photoelectron Spectroscopy* (Perkin-Elmer, Eden Prairie, MN, 1978).
- [13] H. Y. T. Chen, J. P. Chou, C. Y. Lin, C. W. Hu, Y. T. Yang, T. Y. Chen, *Nanoscale* **2017**, *9*, 7207–7216.
- [14] G. Roh, H. Lee, Y. Jeong, J. H. Kim, H. Kim, *Int. J. Hydrogen Energy* **2019**, *44*, 21588–21596.
- [15] D. Radosavkic, J. Thiele, N. Barrett, C. Guillot, R. Belkhou, *Surf. Sci.* **1997**, *377–379*, 168–171.
- [16] B. Ravel, M. Newville, *J. Synchrotron Radiat.* **2005**, *12*, 537–541.
- [17] C. W. Olsen, R. I. Masel, *Surf. Sci.* **1988**, *201*, 444–460.
- [18] W. K. Kuhn, J. Szanyi, D. W. Goodman, *Surf. Sci.* **1992**, *274*, L611–L618.
- [19] J. A. Rodriguez, C. M. Truong, D. W. Goodman, *J. Chem. Phys.* **1992**, *96*, 7814–7825.
- [20] F. L. Hirshfeld, *Theor. Chim. Acta* **1977**, *29*, 129–138.

- [21] T. Jacob, R. P. Muller, W. A. Goddard III, *J. Phys. Chem. B* **2003**, *107*, 9465–9476.
- [22] Y. Sha, T. H. Yu, Y. Liu, B. V. Merinov, W. A. Goddard III, *J. Phys. Chem. Lett.* **2010**, *1*, 856–861.
- [23] J. Nakamura, I. Nakamura, T. Uchijima, Y. Kanai, T. Watanabe, M. Saito, T. Fujitani, *J. Catal.* **1996**, *160*, 65–75.
- [24] I. Nakamura, H. Mantoku, T. Furukawa, T. Fujitani, *J. Phys. Chem.* **2011**, *115*, 16074–16080.
- [25] S. Yamazaki, M. Asahi, N. Taguchi, T. Ioroi, Y. Kishimoto, H. Daimon, M. Inaba, K. Koga, Y. Kurose, H. Inoue, *ACS Catal.* **2020**, *10*, 14567–14580.
- [26] G. te. Velde, E. J. Baerends, *Phys. Rev. B.* **1991**, *44*, 7888–7903.
- [27] J. P. Perdew, K. Burke, M. Ernzerhof, *Phys. Rev. Lett.* **1996**, *77*, 3865–3868.
- [28] Y. Zhang, W. Yang, *Phys. Rev. Lett.* **1998**, *80*, 890.
- [29] S. Grimme, S. Ehrlich, L. Goerigk, *J. Comput. Chem.* **2011**, *32*, 1456–1465.
- [30] E. van Lenthe, E. J. Baerends, J. G. Snijders, *J. Chem. Phys.* **1994**, *99*, 4597–4610.
- [31] Y. Zhao, D. G. Truhlar, *J. Chem. Phys.* **2006**, *125*, 194101.
- [32] P. J. Hay, W. R. Wadt, *J. Chem. Phys.* **1985**, *82*, 299–310.
- [33] L. E. Roy, P. J. Hay, R. L. Martin, *J. Chem. Theory Comput.* **2008**, *4*, 1029–1031.
- [34] A. W. Ehlers, M. Böhme, S. Dapprich, A. Gobbi, A. Höllwarth, V. Jonas, K. F. Köhler, R. Stegmann, A. Veldkamp, G. Frenking, *Chem. Phys. Lett.* **1993**, *208*, 111–114.
- [35] B. I. Dunlap, *J. Chem. Phys.* **1983**, *78*, 3140–3142.
- [36] B. I. Dunlap, *J. Mol. Struct.* **2000**, *529*, 37–40.
- [37] M. J. Frisch, G. W. Trucks, H. B. Schlegel, G. E. Scuseria, M. A. Robb, J. R. Cheeseman, G. Scalmani, V. Barone, G. A. Petersson, H. Nakatsuji, X. Li, M. Caricato, A. V. Marenich, J. Bloino, B. G. Janesko, R. Gomperts, B. Mennucci, H. P. Hratchian, J. V. Ortiz, A. F. Izmaylov, J. L. Sonnenberg, D. Williams-Young, F. Ding, F. Lipparini, F. Egidi, J. Goings, B. Peng, A. Petrone, T. Henderson, D. Ranasinghe, V. G. Zakrzewski, J. Gao, N. Rega, G. Zheng, W. Liang, M. Hada, M. Ehara, K. Toyota, R. Fukuda, J. Hasegawa, M. Ishida, T. Nakajima, Y. Honda, O. Kitao, H. Nakai, T. Vreven, K. Throssell, J. A. Montgomery, Jr., J. E. Peralta, F. Ogliaro, M. J. Bearpark, J. J. Heyd, E. N. Brothers, K. N. Kudin, V. N. Staroverov, T. A. Keith, R. Kobayashi, J. Normand, K. Raghavachari, A. P. Rendell, J. C. Burant, S. S. Iyengar, J. Tomasi, M. Cossi, J. M. Millam, M. Klene, C. Adamo, R. Cammi, J. W. Ochterski, R. L. Martin, K. Morokuma, O. Farkas, J. B. Foresman, D. J. Fox, *Gaussian 16, Revision A.03*, Gaussian, Inc. Wallingford CT, **2016**.

**Chapter 5. Application of Flow Synthesized Pd@Pt Core-Shell
Nanoparticle Catalysts to Acceptorless Dehydrogenation of
Pyrimidines from Alcohols and Amidines**

5.1. Introduction

I have been developing a flow synthesis process for Pd@Pt core-shell catalysts to expand the use of PEFCs. As a result, I have succeeded in flow synthesis of core-shell catalysts with activity and structure comparable to those synthesized by the existing Cu-UPD method. This result shows that the flow synthesis method is a promising method for synthesizing core-shell type catalysts with both high productivity and advanced control of catalyst structure. As mentioned in Chapter 1, there are very few reported cases of organic synthesis reactions using core-shell catalysts compared to electrocatalysts for fuel cells. Therefore, I decided to apply this flow synthesis process to organic synthesis reactions in order to further verify the usefulness of this process.

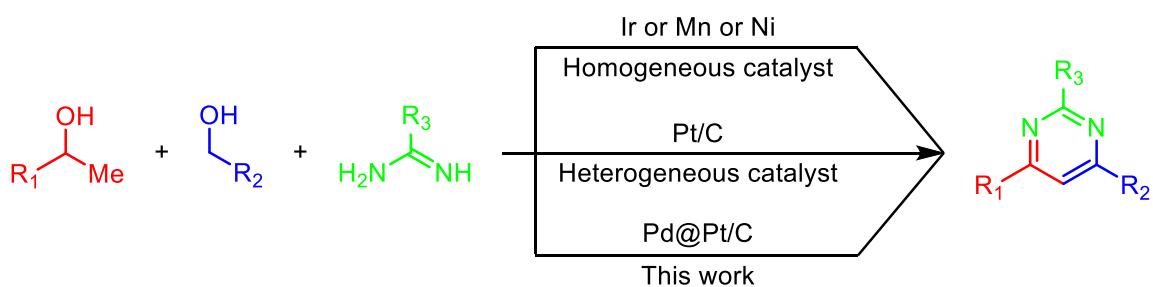
Various organic syntheses have been reported using Pt as a catalyst.¹⁻³ Since the active site of these reactions is Pt as well as Pd@Pt catalysts, they are suitable for examining the effect of core-shelling. Among these reports, I focused on the pyrimidine synthesis by acceptorless dehydrogenative coupling (ADC) from alcohols and amidines catalyzed by Pt/C, as recently reported by Poly, Shimizu et al.³

Pyrimidines are important heterocycles in the synthesis of pharmaceuticals ingredients, agrochemicals, and various functional materials.⁴⁻⁶ They have structural moieties as in natural products and biologically active molecules.⁷ Pyrimidine is a key factor of some important drugs used for the treatment of hyperthyroidism, acute leukemia in children, and adult granulocytic leukemia.⁷⁻¹⁰ In addition, several other pyrimidines show wide-spread pharmacological activities as antitumor, antibacterial, antifungal, antimalarial, analgesic, anticancer, and anti-cholesterol drug.^{8, 11-21} Therefore, it is desirable to develop green and sustainable synthetic methods for pyrimidine derivatives using readily available raw materials.

Over the past several decades, alcohols have been regarded as effective and inexpensive substrates that are converted into value-added heteroatom-containing chemicals.^{22,23} Among the transformations, H₂ evolving, acceptorless dehydrogenation (AD) reactions have become promising for eco-friendly C–C and C–N bond formation reactions using alcohols.^{3,24-43}

There are several reports of multicomponent reactions of heterocycles synthesis with variations in oxidants, solvents, and starting materials.⁴⁴⁻⁴⁸ Transition metal based homogeneous catalysts have been utilized for synthetic processes related to fine chemicals, such as flavors and pharmaceuticals. Following these studies, several groups have recently reported new synthetic methods using the ADC to obtain pyrimidines from easily available starting materials. The methods employ methodology. Kempe et al.,^{19,49} Kirchner et al.,⁵⁰ Herbert et al.,⁵¹ Kundu et al.,⁵² Adhikari et al.⁵³ have reported the synthesis of pyrimidines through ADC condensation with a basic additive (KO^{*t*}-Bu) using

homogeneous transition metal (such as Ir, Mn, and Ni) in one-pot multicomponent reaction.



Scheme 1. Multi-component synthesis of pyrimidines

Compared to conventional homogeneous catalyst systems,^{17,36,49-53} the Pt/C catalyst system reported by Poly, Shimizu et al.³ achieved high activity, high turnover number (TON), wide substrate range, and good reactivity. Furthermore, the heterogeneous nature of the reaction facilitates catalyst reuse, making the reaction industrially valuable. If the core-shell catalyst can be used to reduce the use of Pt, which is a limited resource, the usefulness of this reaction can be further enhanced, thereby demonstrating the potential for application development of Pd@Pt catalysts (Scheme 1). Therefore, I decided to investigate a three-component one-pot synthesis of multi substituted pyrimidines using flow-synthesized Pd@Pt catalyst.

5.2. Results and Discussion

5.2.1. Characterization of Pd@Pt/PVP/C

Pd@Pt core-shell NPs were synthesized using the flow-reactor process with K_2PdCl_4 as a Pd precursor, H_2PtCl_6 as a Pt precursor, $NaBH_4$ as a reductant, and PVP K30 as a capping agent with a total loading of Pd and Pt for 5 wt%. The details of the flow reactor and the preparation method of Pd@Pt/PVP/C catalyst are in experimental section at Capture 2. Then the catalyst was characterized by various characterization techniques. DF-STEM observations and elemental mapping by EDS were performed to directly observe the state of the supported NPs and the core-shell structure (Figure 1). The particle size of this Pd@Pt/PVP/C catalyst is 3.6 nm (Figure 1A, B). Figure 1C-F shows STEM image and EDS mapping images for Pd@Pt/PVP/C samples. In this case, the edge of the sample was rich in Pt (red) while the core was rich in Pd (green). From this result, I can conclude that the structure of core-shell catalyst Pd@Pt/PVP/C had been successfully synthesized. Moreover, from the results of EELS line analysis (Figure 2A,B), the thickness of the Pt shell was estimated to be approximately 0.5 nm, suggesting that the Pt shell consisted of two atomic layers.

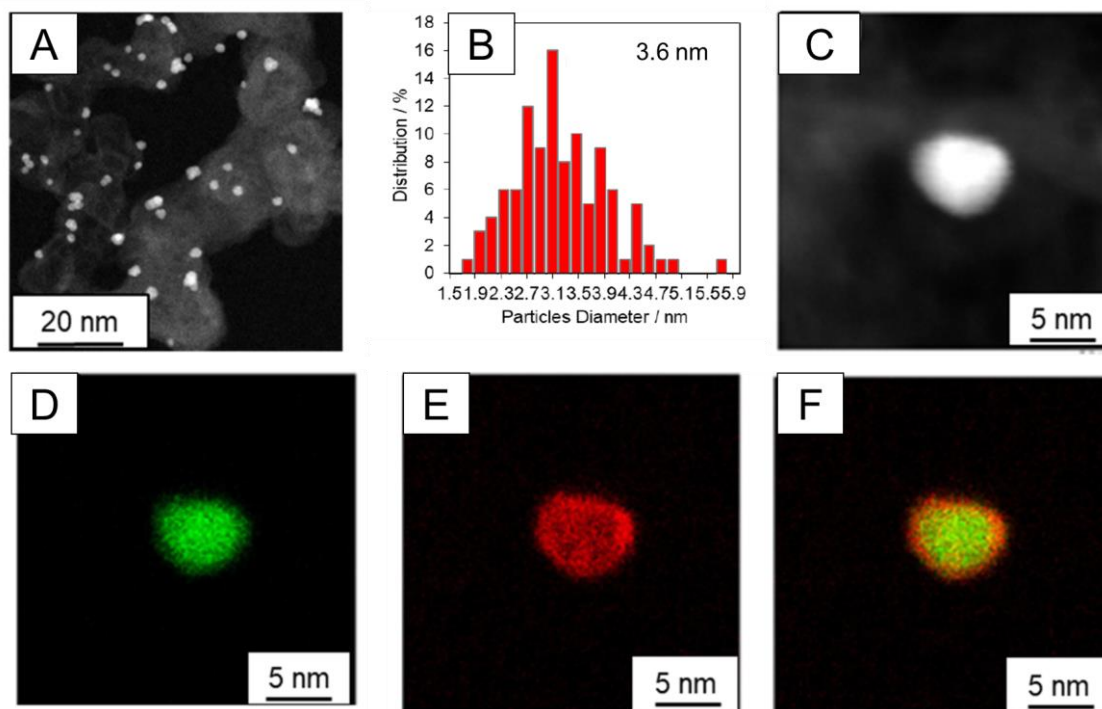


Figure 1. DF-STEM image (A), particle size distributions histogram (B), and DF-STEM-EDS mapping images (C-F) with Pd shown in green and Pt in red, of Pd@Pt/PVP/C NPs synthesized by the flow process.

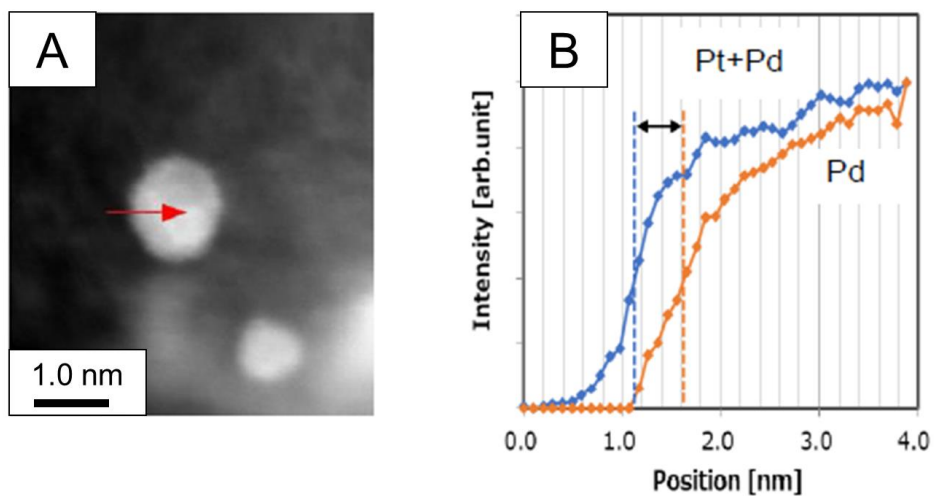


Figure 2. HAADF STEM atomic resolved (A) image of the Pd@Pt/PVP/C catalyst synthesized by flow method Chemical mapping (B) of the Pd@Pt/PVP/C catalyst depicting the HAADF intensity (blue curve) and the EELS signal (orange curve) derived from the Pd peak of M edge around 420 eV.

TEM and TEM-EDS images of the catalyst after pre-reduction under a H₂ atmosphere at 300 °C are shown in Figure 3. EDS mapping results showed that the core-shell structure was stable after reduction (Figure 3C-F). The particle size was 3.7 nm, almost the same as the 3.6 nm of the fresh catalyst, and no significant agglomeration was observed.⁵⁴ Table 1 shows Pt dispersion for the catalysts (pre-reduced at 300 °C) estimated by a standard CO chemisorption method. The result shows that 5 wt% Pt/C and 2.5 wt% Pd@Pt/PVP/C have similar Pt dispersion.

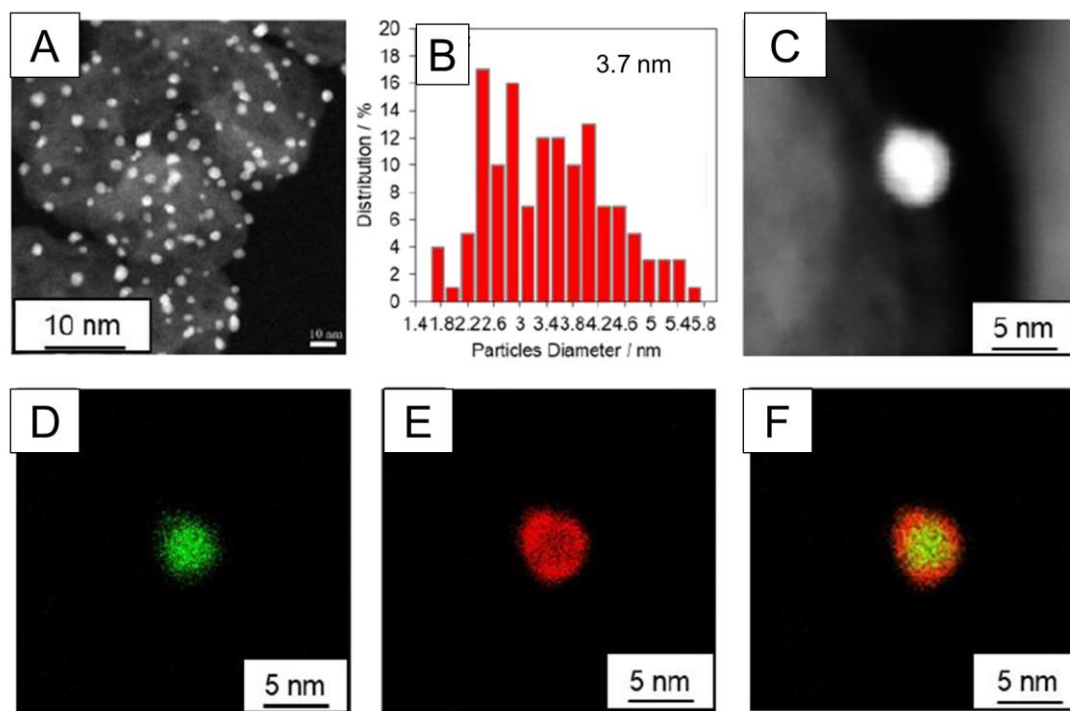


Figure 3. DF-STEM image (A), particle size distributions histogram (B), and DF-STEM-EDS mapping images (C-F) with Pd shown in green and Pt in red, of H₂-300-Pd@Pt/PVP/C.

Table 1. CO adsorption data of the catalysts pre-reduced at 300 °C

Catalyst	Pt content [wt%]	Pd content [wt%]	Pt dispersion [%]	Surface area [m ² g ⁻¹]
Pt/C	5	0	11.93	29.46
Pd@Pt/PVP/C	2.5	2.5	12.65	31.24

Figure 4A shows the Pt L₃ edge XANES spectra of Pd@Pt/PVP/C before and after pre-reduction and Pt foil. The peak height of the as-prepared Pd@Pt/PVP/C is slightly higher than that of Pt foil, and the reduction treatment decreased the peak height. This suggests that Pt species in the as-prepared Pd@Pt/PVP/C is a mixture of metallic Pt (0) as a main Pt species and a small amount of oxidized Pt species, which is converted to the metallic Pt (0) by the reduction treatment at 300 °C. As shown in Figure 4B, the Fourier transforms of the EXAFS for the as-prepared and reduced Pd@Pt/PVP/C show significantly lower peak height for the Pt–Pt (and/or Pt–Pd) coordination than that for Pt foil, indicating that metal particle sizes of these samples are small. The EXAFS curve-fitting analysis (Table 2) of the as-prepared and reduced Pd@Pt/PVP/C shows the presence of Pt–Pt and Pt–Pd bonds with bond distance (0.271–0.273 nm) that is close to that of Pt foil. Present fitting result at *k/R* space in Figure 5. The Pt–Pt and Pt–Pd coordination numbers were almost the same before and after

reduction. Because the coordination number of Pt–Pt shell (4.7) is adequately higher than that of Pt–Pd shell (2.3), Pd is supposed to be covered by Pt metal, giving the core-shell structure even after the H₂ treatment.⁵⁵ The result indicates that majority of Pt atoms are surrounded by Pt and a small part of Pt atoms are next to Pd atoms, and this local structure does not change after the reduction treatment. This EXAFS result is consistent with the Pd@Pt core-shell model observed by the DF-STEM-EDS mapping images. Summarizing the XANES/EXAFS and DF-STEM-EDS results, it is shown that carbon-supported Pd@Pt core-shell metal nanoparticles are successfully prepared by the present flow reactor approach.⁵⁴

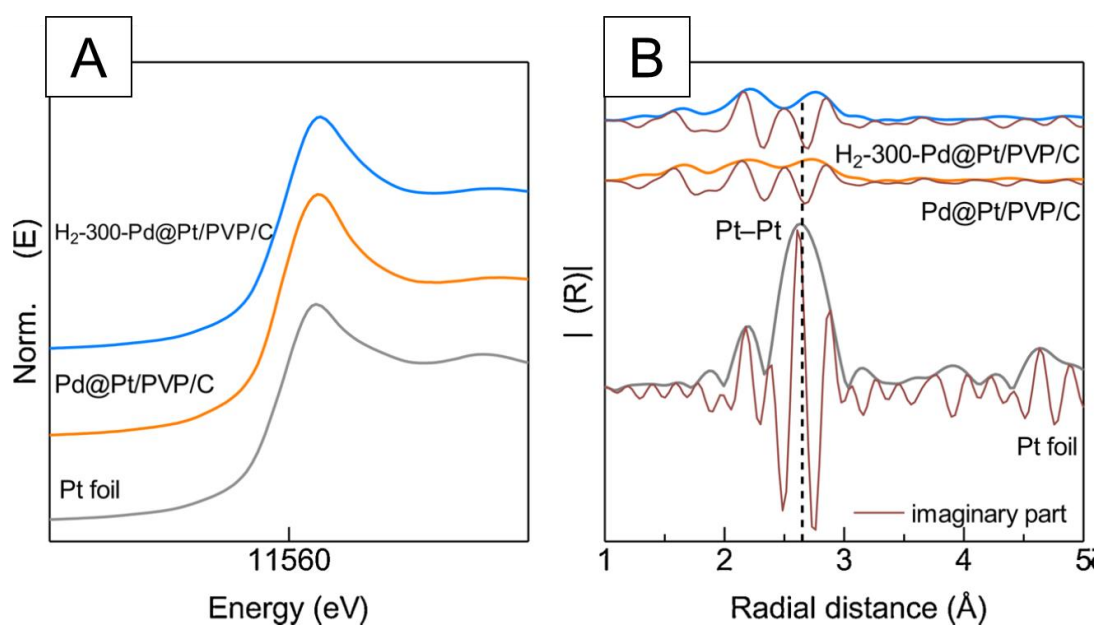


Figure 4. Pt L3-edge (A) XANES spectra and (B) EXAFS spectra of Pd@Pt/PVP/C before and after the pre-reduction at 300 °C.

Table 2. Curve-fitting analysis of Pt L₃-Edge EXAFS of Pd@Pt/PVP/C.^{a)}

Sample	Shell	CN ^{b)}	R ^{c)} / x 10 ⁻¹ [nm]	σ ^{2,d)} / x 10 ⁻¹ [nm ²]	R _f [%] ^e
As-synthesized Pd@Pt/PVP/C	Pt–Pt	4.6	2.71 ± 0.01	0.081 ± 0.04	9.0
	Pt–Pd	1.9	2.72 ± 0.01	0.081 ± 0.05	
	Pt–Cl	1.2	2.09 ± 0.04	0.095 ± 0.07	
Pd@Pt/PVP/C (after H ₂ reduction)	Pt–Pt	4.7	2.72 ± 0.01	0.082 ± 0.03	7.0
	Pt–Pd	2.3	2.73 ± 0.01	0.070 ± 0.04	
	Pt–Cl	0.97	2.09 ± 0.05	0.098 ± 0.08	

a): k-range = 0.3–1.6 nm⁻¹. r-range = 0.16–0.34. Number of free parameters = 12. b): Coordination number. c): Bond length. d): Debye-Waller factor. f): Residual factor.

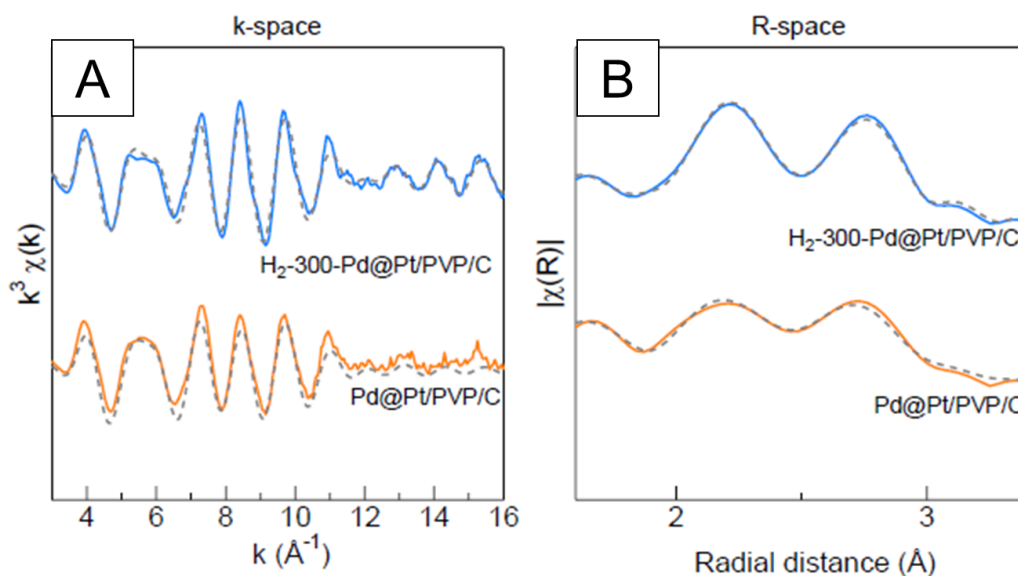


Figure 5. *k*-space and R-space (A) XANES spectra and (B) EXAFS spectra of Pd@Pt/PVP/C before and after the pre-reduction at 300 °C. Solid and dashed lines describe the experimental data and fitting results, respectively.

5.2.2. Catalyst screening and reaction conditions

Synthesis of 2,4,6-triphenyl pyrimidine (**4a**) by the reaction of 1-phenylethanol (**1a**), benzyl alcohol (**2a**) and benzamidine (**3a**)³ was investigated as a model reaction for the dehydrogenative cross-coupling of alcohols to form pyrimidines (Table 3).

Table 3. Catalyst screening for the Synthesis of 2,4,6 triphenyl pyrimidine from 1-phenyl ethanol, benzyl alcohol and benzamidine.

$\text{Ph-CH(OH)-Me} + \text{Ph-CH}_2\text{-OH} + \text{Ph-NH-C(=NH)-NH}_2 \xrightarrow[\text{1.5 mmol KOt-Bu, 2 mL toluene, reflux, 24 h}]{\text{Cat.}}$

Entry	Pd [wt%]	Pt [wt%]	Cat. amount [mol%]	GC yield [%]
1	-	5	1	95
2	5	-	1	42
3	-	2.5	1	68
4	2.5	-	1	17
5 ^{a)}	2.5	2.5	0.5	81
6 ^{b)}	2.5	2.5	0.5	93
7 ^{c)}	2.5	2.5	0.5	84

a): Pd@Pt/PVP/C prepared in batch process. b): Pd@Pt/PVP/C prepared in flow process (with 1.1 mmol KOt-Bu). c): Pd@Pt/C prepared in flow process.

Table 3 shows the catalyst screening results for the synthesis of **4a** with the reaction of 1.25 mmol of **1a**, 1.5 mmol of **2a**, and 1.0 mmol of **3a** refluxing in toluene for 24 h. I compared various monometallic and bimetallic core-shell catalysts in the terms of the yield of the product **4a** based on amidine **3a**. The catalytic tests for the monometallic catalysts (Pt/C and Pd/C) were carried out using 1 mol% of the catalyst. Pt/C and Pd/C with metal content of 5 wt% show the pyrimidine yield of 95% and 42%, respectively (entries 1–2). On the other hand, the yields of Pt/C and Pd/C, where the metal content was reduced to 2.5 wt%, were lower at 68% and 17%, respectively (Entry 3-4). The catalytic tests for the core-shell catalysts (Pd@Pt/PVP/C prepared in batch process and flow process, Pd@Pt/C prepared in direct-support flow process) were carried out using 0.5 mol% of the Pt. The reaction by 0.5 mol% core-shell Pd@Pt catalysts prepared by the flow process showed 93% yield (entry 6) comparable to the yield by 1 mol% Pt/C, suggesting that catalytic efficiency is improved by the presence of Pd core. The Pd@Pt catalyst prepared by a batch process (entry 5) showed lower yield than that prepared by the flow process (93%) (entry 6). The lower activity of former catalyst might be due to its larger metal particle size (about 5.0 nm). This shows the advantage of the flow synthesis method in that it can synthesize finer core-shell catalysts than the batch synthesis method. PVP is widely used as a capping agent that plays an important role to prevent the aggregation of nanoparticles.^{56,57} The core-shell Pd@Pt catalyst without using PVP (entry 7) showed lower yield

(84%) than that with PVP (93%). These results indicate that unlike the ORR reaction, PVP does not inhibit this reaction.

It is well known that a bimetallic core-shell structure with an inner core of a metal and an external shell of another metal may provide unique physical and chemical properties.^{58,59} In Pd@Pt core-shell catalysts, Pt is reported to be slightly electron rich.⁶⁰ In Capture 3, I also reported the negative charge transfer to Pt in Pd@Pt.⁶¹ This might accelerate Pt-catalyzed C–H bond dissociation step as an important step of the present pyrimidine synthesis.³

5.2.3. Recyclability test of Pd@Pt/PVP/C

The recyclability of the catalyst system was then tested (Figure 6). After the standard reaction for 24 h, the catalyst was separated from the reaction mixture by centrifugation, dried at 40 °C for 3 h under vacuum, and reduced at 300 °C for 0.5 h in H₂. The recovered Pd@Pt/PVP/C catalyst showed high yields of 93-78% for at least 5 cycles. The reaction rate decreased slightly during the recycling test, which is consistent with the results of previous recycling tests on Pt/C catalyst.³

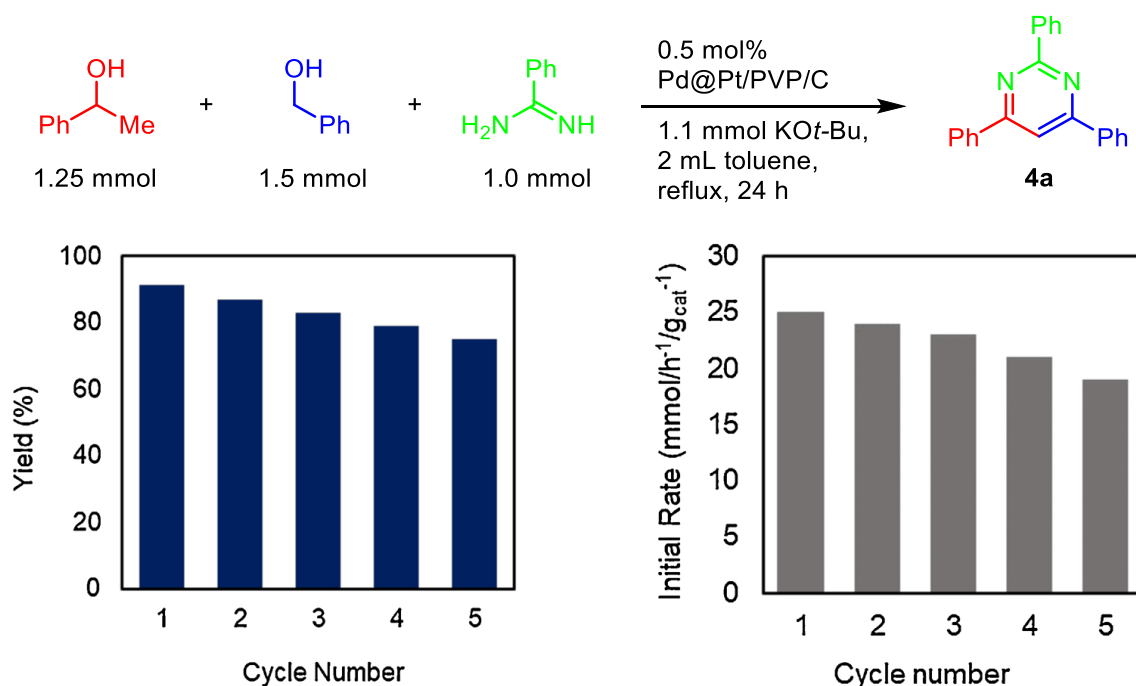


Figure 6. Catalyst reuse for the synthesis promoted by Pd@Pt/PVP/C under the standard reaction conditions.

To investigate the possible reasons for the gradual catalyst deactivation, the recycled catalyst was characterized using DF-STEM and EDS mapping (Figure 7). The result revealed that the particles size

for the recycled Pd@Pt/PVP/C catalyst (3.7 nm) is close to that for the fresh catalyst (3.6 nm) (Figures 2 and 7). Comparison of the mapping images of the fresh (Figure 1F) and recycled (Figure 7F) catalyst shows that the core-shell structure is slightly changed by the reaction treatment, which can result in the slight decrease in the activity of the recycled catalyst. The reason for this change is still unclear, but one possibility is that it is due to slight mixing of Pd and Pt during the different catalyst treatments. It was also observed that the particle size of the NPs increased slightly during recycling. The secondary particles were slightly larger than the primary particles, suggesting that agglomeration of the NPs may have occurred.

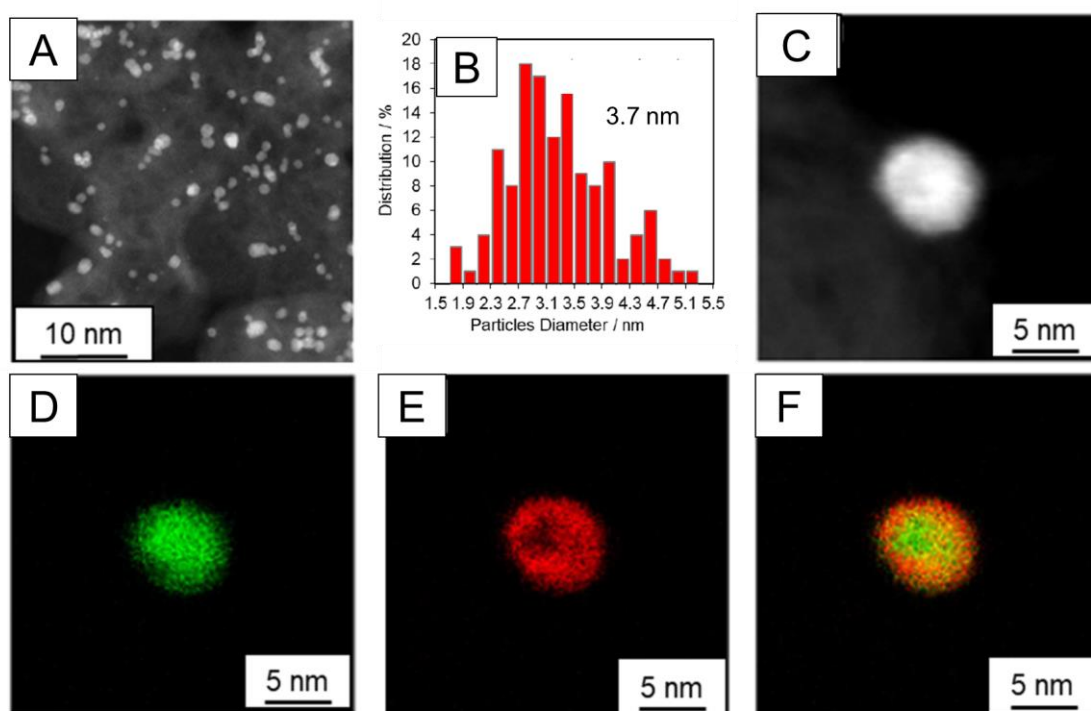
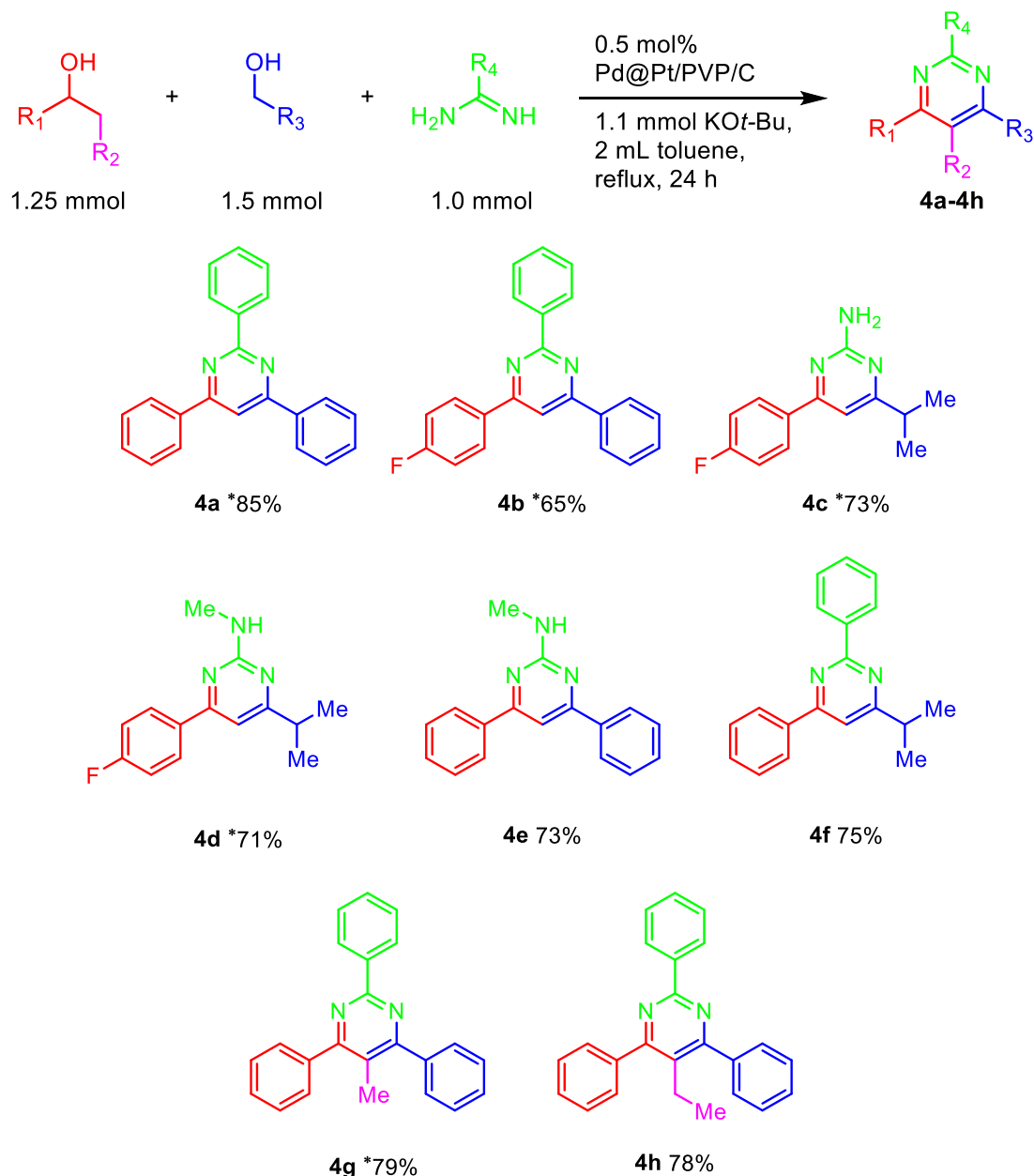


Figure 7. DF-STEM image (A), particle size distribution histogram (B), and DF-STEM-EDS mapping images (A-D) with Pd shown in green and Pt in red, of Recycle-Pd@Pt/PVP/C NPs synthesized by the flow process.

2.4. Performance of Pd@Pt/PVP/C-catalyzed dehydrogenation reaction

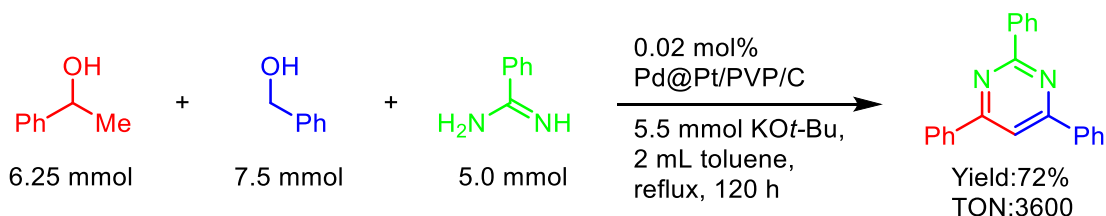
Under the optimized reaction conditions, I studied the synthesis pyrimidines from various secondary alcohols, primary alcohols and amidines. As shown in Scheme 2, various primary alcohols including aromatic and aliphatic alcohols, and amidines were coupled to yield the corresponding pyrimidines in good to high yields (65–93%). The reaction proceeded in good yield even with primary alcohols having an alkyl group instead of an aryl group as substituent R₂ (**4c**, **4d**, and **4f**). The reaction

proceeded without problems even when guanidine was used as a substrate instead of amidine (**4c**, **4d**, and **4e**). It should be noted that products **4c** and **4d** are important intermediates in the total synthesis of rosuvastatin, which is used as a pharmaceutical drug for treatment of patients with high levels of cholesterol.^{3,62} Notably, tetra-substituted pyrimidine derivatives were also synthesized in good yields by this protocol (**4g** and **4h**).



Scheme 2. Synthesis of pyrimidines from various secondary alcohols, primary alcohols and amidines. Asterisk marked yields mean the isolated yields and they are confirmed by NMR analysis. Other yields without asterisk mean yields are confirmed by only GC.

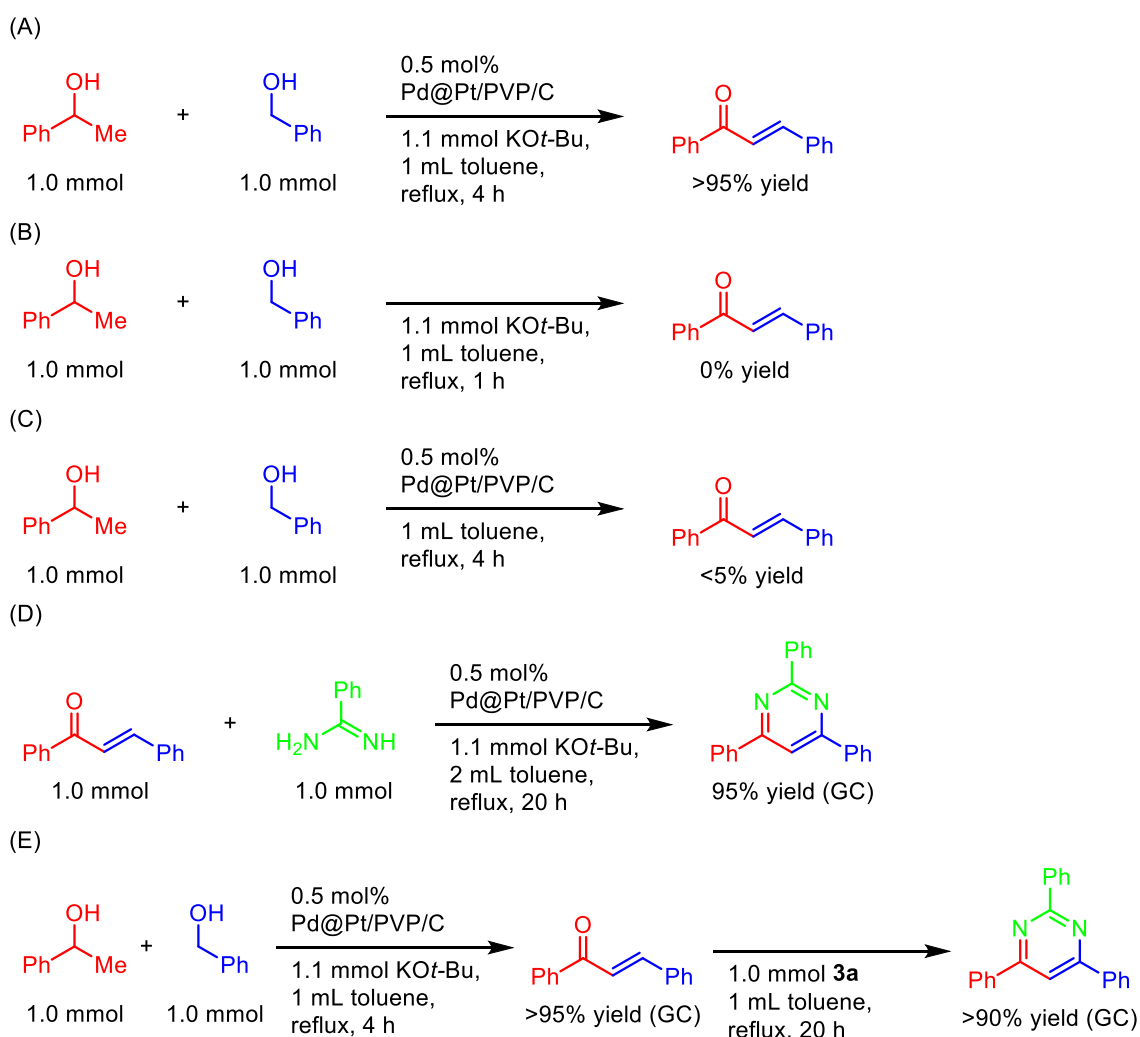
Next, I performed a pyrimidine synthesis on the gram scale (Scheme 3). The amount of Pd@Pt/PVP/C used was reduced from 0.5 mol% to 0.02 mol%, but the reaction proceeded in good yield, yielding the desired product in 72 % yield. This corresponds to TON 3600. This result demonstrates the high catalytic efficiency of this system.



Scheme 3. Gram scale synthesis of pyrimidines from 1-phenyl ethanol, benzyl alcohol and benzamidine.

5.2.5. Control experiment

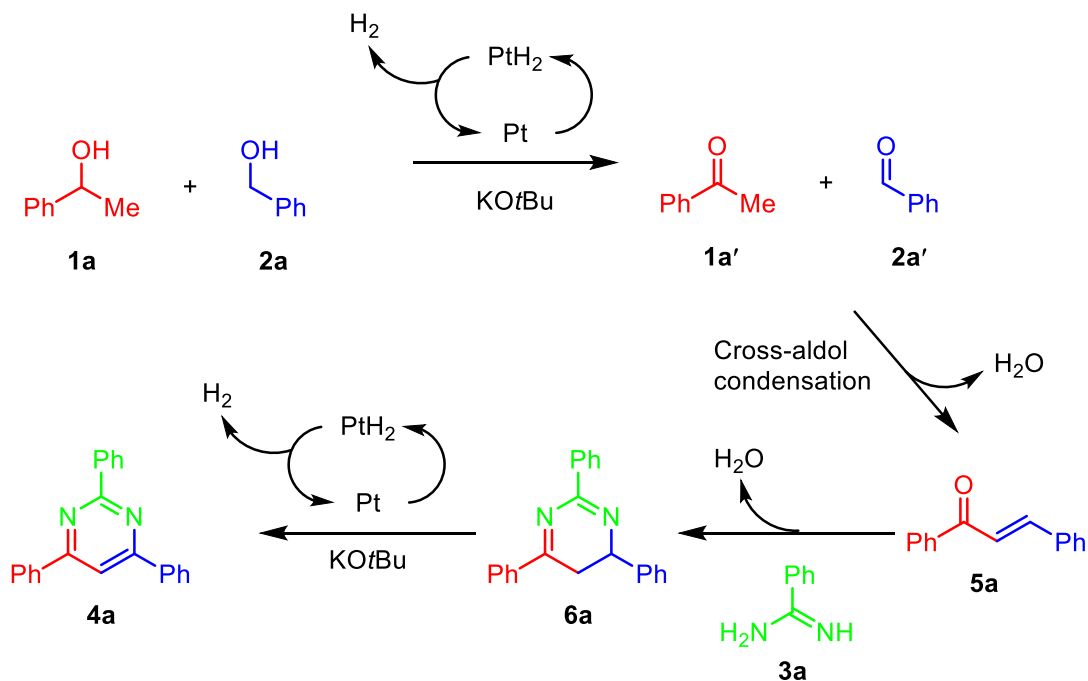
Finally, I performed control experiments to explore the plausible reaction mechanism for the formation of substituted pyrimidines via selective C–C and C–N bond formation reaction catalyzed by Pd@Pt/PVP/C catalyst. First, the reaction of benzyl alcohol (**1a**) and 1-phenylethanol (**2b**) was carried out under the standard reaction conditions (Scheme 4A). The reaction for 4 h gave chalcone, which generated by aldol condensation, in >95% isolated yield. On the other hand, when a similar reaction was performed under conditions without Pd@Pt/PVP/C catalyst, both alcohols remained unreacted (Scheme 4B). This result suggested that the dehydrogenation of alcohols was catalyzed by Pd@Pt/PVP/C where Pt sites acts as an active site of dehydrogenation and deprotonation steps of the reaction. In the absence of base (KOt-Bu), both alcohols reacted very slowly and produced 5% of chalcone (Scheme 4C). This suggests that base plays an important role such as deprotonation of alcohols and aldol condensation. The reaction of benzamidine (**3a**) with chalcone in the presence of Pd@Pt/PVP/C catalyst and base gave the pyrimidine product **4a** in 95% GC yield (Scheme 4D). The reaction of chalcone, prepared by the reaction of **1a** and **2a**, with amidine **3a** gave the pyrimidine product **4a** in 90% yield (Scheme 4E). These results indicate that chalcone is reaction intermediate, and reacts with amidine to form pyridine product.



Scheme 4. Control experiments for the multicomponent synthesis of pyrimidines.

2.6. Reaction pathway

Based on the results of control experiments and literature reports^{3,52} a possible reaction pathway for the formation of substituted pyrimidines is proposed in Scheme 5. First, Secondary alcohol (**1a**) and primary alcohol (**2a**) undergo dehydrogenation by a Pd@Pt core-shell catalyst to give ketone **1a'** and aldehyde **2a'**, and H₂. Next, a subsequent base-mediated aldol condensation afford an α,β -unsaturated ketone intermediate **5a**, which in turn reacts with the amidine (**3a**) to give dihydropyrimidine intermediate (**6a**) via intermolecular condensation. Finally, dehydrogenation by a Pd@Pt core-shell catalyst of intermediate **6a** produces the desired pyrimidine product **4a**. The generation of ketone **1a'**, aldehyde **2a'** and α,β -unsaturated ketone **5a** was confirmed using GC-MS.



Scheme 5. Plausible reaction mechanism.

5.3. Conclusion

In this study, acceptorless dehydrogenative synthesis of pyrimidines was achieved using flow synthesized Pd@Pt/C catalyst. The Pd@Pt/C catalyst was applicable to a wide range of substrates (primary and secondary alcohols, amidines) and yielded multi substituted pyrimidines in moderate to good yields. The Pd@Pt catalyst showed higher catalytic activity at lower Pt loadings than the Pt catalyst. These results confirm that core-shell catalysts can be used for applications other than fuel cell catalysts and prove their usefulness. Compared to existing core-shell catalyst synthesis methods, flow synthesis is an effective method for the continuous production of highly active core-shell catalysts, since it offers both precisely control the nanoparticles particle size and productivity of nanoparticles.

5.4. Experimental

5.4.1. General

Commercially available organic and inorganic compounds from Wako Pure Chemical Industry and sigma Aldrich were used without further purifications. Carbon ECP was purchased from Lion Specialty Chemicals Co., Ltd. All aqueous solutions were prepared using highly purified deionized water with a resistivity of 18.2 M Ω cm. The GC (Shimadzu GC-2025) and GCMS (Shimadzu GCMS-QP2010) analyses were carried out with HP-5 column (Agilent) using nitrogen as the carrier gas. ¹H and ¹³C NMR spectra were recorded using at ambient temperature on JEOL-ECX 400 operating at 400 MHz and 100 MHz, respectively with tetramethyl silane as an internal standard.

5.4.2. Catalyst preparation

Synthesis of Pd@Pt core shell in flow reactor

Flow synthesis of the Pd@Pt catalyst was performed using the method described in the experimental section of Chapter 2.

5.4.3. Characterization of catalyst

5.4.3.1. TEM / EDS / EELS

Analyzed using the same methods as described in the experimental section of Chapter 2.

5.4.3.2. XAFS measurement

Measured and analyzed using the same methods as described in the experimental section of Chapter 2.

5.4.3.3. CO adsorption measurement

CO pulse adsorption measurements were performed to determine the extent of platinum dispersion. In these tests, 0.1g of catalyst samples treated at different temperature were placed in a U-shaped quartz tube and then reduced under a flow of H₂ (20 mL/min) at 300 °C for 60 min, purged with pure Ar (30 mL/min). After cooling to room temperature naturally, pulses of CO gas were passed through the U-shaped tube and the level of adsorption was assessed by TCD.

5.4.4. Catalytic tests

Pd@Pt (39 mg; 0.5 mol%, 2.5 wt% Pt with respect to the benzamidine) was used as a standard catalyst. After the reduction at 300 °C, the catalyst in the closed glasstube sealed with a septum inlet

was cooled to room temperature under H₂. Toluene (2 mL) was injected to the pre reduced catalyst inside the glass tube through a septum inlet. Then the septum was tentatively removed under air, and primary alcohol (1.5 mmol), secondary alcohol (1.25 mmol), amidine (1.0 mmol), KO^t-Bu (1.1 mmol), *n*-dodecane (0.25 mmol) and a magnetic stirrer bar was put in the tube (cylindrical Pyrex glass tube, 17 cm³), containing a magnetic stirrer bar and placed in a heated reactor, at reflux conditions, under a nitrogen atmosphere with stirring at 400 rpm.

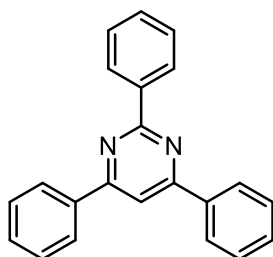
For the standard reaction of benzyl alcohol, 1-phenylethanol and benzamidine and yields of products (based on benzamidine) were determined by GC using *n*-dodecane as an internal standard adopting the GC sensitivity estimated using the isolated products or commercial products. Substrate scopes for the Pd@Pt catalyzed system were also explored. The developed catalytic system was effective for the reaction of various primary alcohols (benzylic, aliphatic), secondary alcohols (1-phenylethanol, aliphatic) and amidines (aliphatic and benzamidine) providing high yields (65-93%) of the corresponding pyrimidines, the products were isolated by column chromatography with silicagel 60 (spherical, 63-210 μm, Wako Chemical Co. Ltd.) using hexane as eluting solvent, and the yields of the isolated pyrimidine derivatives (based on benzamidine) were determined. The products were identified by ¹H and ¹³C NMR and GC MS equipped with the same column as GC.

5.4.5. NMR and GC/MS analysis

¹H and ¹³C NMR spectra were assigned and reproduced to the corresponding literature. ¹H and ¹³C NMR spectra were recorded using at ambient temperature on JEOL-ECX 400 operating at 400.17 and 100.92 MHz, respectively with tetramethyl silane as an internal standard. Abbreviations used in the NMR experiments: s, singlet; d, doublet; t, triplet; q, quartet; m, multiplet, br, broad singlet. GC-MS spectra was taken by SHIMADZU QP2010.

5.4.6. Characterization of Products

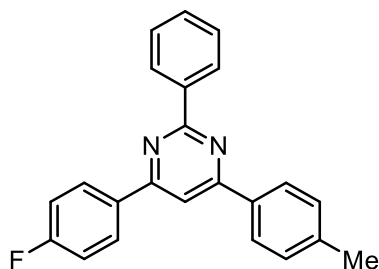
2,4,6-triphenylpyrimidine:^{3,50}



4a

¹H NMR (400.17 MHz, CDCl₃, TMS): δ 8.74 (d, J= 6.18 Hz, 1H), 8.30 (d, J= 7.26 Hz, 4H), 8.02 (s, 1H), 7.57-7.25 (m, 10H), ¹³C NMR (150.92 MHz, CDCl₃): δ 164.78, 164.53 (CX2), 138.17 (CX3), 130.76 (CX2), 130.62 (CX3), 128.91 (CX4), 128.48 (CX2), 128.44 (CX4), 110.30; GC-MS m/e 308.15.

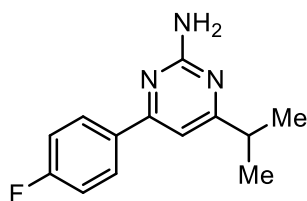
4-(4-Fluoro-phenyl)-2-phenyl-6-p-tolyl-pyrimidine:^{3,49}



4b

¹H NMR (400 MHz, CDCl₃, TMS): δ 8.72-8.70 (m, 2H), 8.32-8.27 (m, 4H), 7.97 (s, 1H), 7.57-7.52 (m, 6H), 7.27-7.22 (m, 2H), 2.17 (s, 3H), ¹³C NMR (100 MHz, CDCl₃): δ 165.83, 164.84, 164.50, 163.62, 163.46 (d, J = 187.84 Hz), 137.99, 137.42, 136.20, 130.84 (d, J = 143.05 Hz), 129.32, 129.22, 128.90 (d, J = 8.67 Hz), 128.44, 127.24, 116.04, 115.83 (d, J = 21.67 Hz), 109.89, 30.92; GC-MS m/e 340.15.

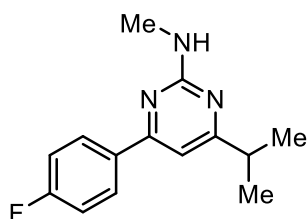
4-(4-Fluoro-phenyl)-6-isopropyl-pyrimidin-2-ylamine:^{3,50}



4c

¹H NMR (600.17 MHz, CDCl₃, TMS): δ 8.09-8.05 (m, 2H), 7.48-7.44 (m, 2H), 7.42 (s, 1H), 5.26 (s, 2H), 4.82-4.80 (m, 1H), 2.15 (s, 6H), ¹³C NMR (150.92 MHz, CDCl₃): δ 165.31, 162.84, 133.88, 139.74, 137.93, 130.33, 128.66, 128.49, 127.65, 127.07, 103.20, 45.68, 30.90; GC-MS m/e 231.10.

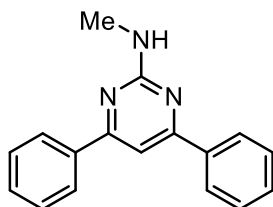
4-(4-Fluoro-phenyl)-6-isopropyl-pyrimidin-2-yl-methyl-amine:^{3,50}



4d

¹H NMR (400 MHz, CDCl₃, TMS): δ 8.05-7.97 (m, 2H), 7.18-7.08 (m, 2H), 6.80 (s, 1H), 5.26 (br. s., 1H), 3.05 (d, J = 4.55 Hz, 3H), 2.88-2.79 (m, 1H), 1.28 (d, J = 8.23 Hz, 6H), ¹³C NMR (100 MHz, CDCl₃): δ 177.28, 165.31 (d, J = 173.48 Hz), 163.59, 163.20, 162.73, 134.24, 128.98 (d, J = 7.67 Hz), 128.89, 115.51 (d, J = 21.09 Hz), 102.95, 36.26, 28.53, 21.85; GC-MS m/e 245.15.

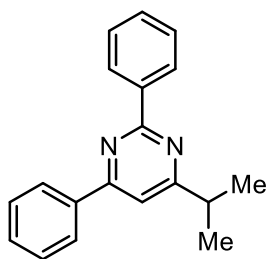
(4,6-Diphenyl-pyrimidin-2-yl)-methyl-amine:



4e

GC-MS m/e 261.15.

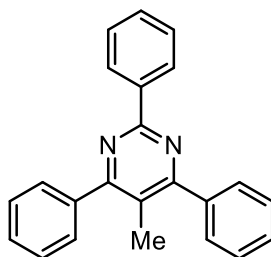
4-isopropyl-2,6-diphenylpyrimidine:³



4f

GC-MS m/e 274.1.

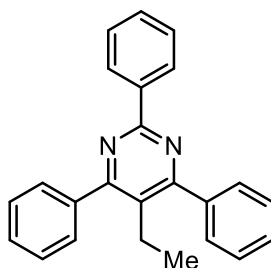
5-methyl-2,4,6-triphenylpyrimidine:⁶³



4g

¹H NMR (400 MHz, CDCl₃, TMS): δ 8.05-7.97 (m, 2H), 7.61-7.45 (m, 4H), 7.44-7.25 (m, 9H), 2.17 (s, 3H), ¹³C NMR (100 MHz, CDCl₃): δ 171.13, 162.99, 130.98, 130.13, 128.83, 128.56, 127.98, 127.35, 126.86, 126.38, 30.92. GC-MS m/e 322.4.

5-ethyl-2,4,6-triphenylpyrimidine:



4h

GC-MS m/e 336.2.

5.5. References

- [1] D. Tongsakul, S. Nishimura, K. Ebitani, *J. Phys. Chem. C* **2014**, *118*, 11723–11730.
- [2] R. Arundhathi, T. Mizugaki, T. Mitsudome, K. Jitsukawa, K. Kaneda, *ChemSusChem* **2013**, *6*, 1345–1347.
- [3] S. S. Poly, S.M.A.H. Siddiki, A.S. Touchy, K.W. Ting, T. Toyao, Z. Maeno, Y. Kanda, K.I. Shimizu, *ACS Catal.* **2018**, *8*, 11330–11341.
- [4] V. Sharma, N. Chitranshi, A. K. Agarwal, *Int. J. Med. Chem.* **2014**, *2014*, 202784–202815.
- [5] M. Sahu, N. Siddiqui, *Int. J. Pharm. Pharm. Sci* **2016**, *8*, 8–21.
- [6] G. G. Furin, *Adv. Heterocycl. Chem.* **2006**, *42*, 285–319.
- [7] R. Singh, *World J. Pharm. Pharm. Sci.* **2014**, *6*, 124–127.
- [8] A. Agarwal, K. Srivastava, S. K. Puri, P. M. S. Chauhan, *Bioorg. Med. Chem. Lett.* **2005**, *15*, 3133–3136.
- [9] J. J. Fiol, M. Barcel'ó-Oliver, A. Tasada, A. Frontera, 'A. Terr'on, 'A. García-Raso, *Coord. Chem. Rev.* **2013**, *257*, 2705–2715.
- [10] M. Asif, *Int. J. Bioorganic Chem.* **2017**, *2*, 146–152.
- [11] A. R. Katritzky, C. W. Rees, *Comp. Heterocycl. Chem.* **1985**, *74*, 233–233.
- [12] J. M. Andersen, J. M. Dietschy, *J. Biol. Chem.* **1978**, *253*, 9024–9032.
- [13] G. Joshi, H. Nayyar, J. Marin Alex, G. S. Vishwakarma, S. Mittal, R. Kumar, *Curr. Top. Med. Chem.* **2016**, *16*, 3175–3210.
- [14] D. J. Brown, *The Pyrimidines* **1962**, *139*, 29–30.
- [15] M. Johar, T. Manning, C. Tse, N. Desroches, B. Agrawal, D. Y. Kunimoto, R. Kumar, *J. Med. Chem.* **2007**, *50*, 3696–3705.
- [16] N. Azas, P. Rathelot, S. Djekou, F. Delmas, A. Gellis, C. Di Giorgio, P. Vanelle, P. Timon-David, *Farmaco* **2003**, *58*, 1263–1270.
- [17] N. A. Abdel-Latif, N. M. Sabry, A. M. Mohamed, M. M. Abdulla, *Monatsh. Chem.* **2007**, *138*, 715–724.
- [18] A. G. E. Amr, A. M. Mohamed, S. F. Mohamed, N. A. Abdel-Hafez, A. E. F. G. Hammam, *Bioorg. Med. Chem.* **2006**, *14*, 5481–5488.
- [19] N. Deibl, K. Ament, R. Kempe, *J. Am. Chem. Soc.* **2015**, *137*, 12804–12807.
- [20] R. Mishra, I. Tomar, *ChemInform.* **2011**, *2*, 758–771.
- [21] M. Bessi'eres, V. Roy, L. A. Agrofoglio, *RSC Adv.* **2014**, *4*, 59747–59749.
- [22] C. O. Tuck, E. P'erez, I. T. Horv'ath, R. A. Sheldon, M. Poliakoff, *Science* **2012**, *337*, 695–699.

- [23] M. A. R. Meier, *Macromol. Rapid Commun.* **2019**, *40*, 1800524–1800534.
- [24] S. Michlik, R. Kempe, *Nat. Chem.* **2013**, *5*, 140–144.
- [25] M. Zhang, H. Neumann, M. Beller, *Angew. Chem. Int. Ed.* **2013**, *52*, 597–601.
- [26] S. Parua, S. Das, R. Sikari, S. Sinha, N. D. Paul, *J. Org. Chem.* **2017**, *82*, 7165–7175.
- [27] C. Gunanathan, D. Milstein, *Acc. Chem. Res.* **2011**, *44*, 588–602.
- [28] S. M. A. Hakim Siddiki, T. Toyao, K. I. Shimizu, *Green Chem.* **2018**, *20*, 2933–2952.
- [29] P. Daw, A. Kumar, N. A. Espinosa-Jalapa, Y. Diskin-Posner, Y. Ben-David, D. Milstein, *ACS Catal.* **2018**, *8*, 7734–7741.
- [30] F. Li, L. Lu, P. Liu, *Org. Lett.* **2016**, *18*, 2580–2583.
- [31] F. Li, C. Sun, N. Wang, *J. Org. Chem.* **2014**, *79*, 8031–8039.
- [32] R. Wang, J. Ma, F. Li, *J. Org. Chem.* **2015**, *80*, 5737–5744.
- [33] S. Parua, R. Sikari, S. Sinha, G. Chakraborty, R. Mondal, N.D. Paul, *J. Org. Chem.* **2018**, *83*, 11154–11166.
- [34] N. A. Espinosa-Jalapa, A. Kumar, G. Leitus, Y. Diskin-Posner, D. Milstein, *J. Am. Chem. Soc.* **2017**, *139*, 11722–11725.
- [35] M. Nielsen, H. Junge, A. Kammer, M. Beller, *Angew. Chem. Int. Ed.* **2012**, *51*, 5711–5713.
- [36] A. Khalafi-Nezhad, F. Panahi, *ACS Catal.* **2014**, *4*, 1686–1692.
- [37] D. Srimani, Y. Ben-David, D. Milstein, *Angew. Chem. Int. Ed.* **2013**, *52*, 4012–4015.
- [38] R. H. Crabtree, *Chem. Rev.* **2017**, *117*, 9228–9246.
- [39] P. Daw, Y. Ben-David, D. Milstein, *J. Am. Chem. Soc.* **2018**, *140*, 11931–11934.
- [40] H. A. Ho, K. Manna, A. D. Sadow, *Angew. Chem. Int. Ed.* **2012**, *51*, 8607–8610.
- [41] N. D. Schley, G. E. Dobereiner, R. H. Crabtree, *Organometallics* **2011**, *30*, 4174–4179.
- [42] D. Srimani, Y. Ben-David, D. Milstein, *Chem. Commun.* **2013**, *49*, 6632–6634.
- [43] P. Daw, A. Kumar, N. A. Espinosa-Jalapa, Y. Ben-David, D. Milstein, *J. Am. Chem. Soc.* **2019**, *141*, 12202–12206.
- [44] J. Zhu, H. Bienaym'e, *Multicomponent Reactions.* **2005**, *15*, 2624–2624.
- [45] R. Mondal, S. Sinha, S. Das, G. Chakraborty, N. D. Paul, *Adv. Synth. Catal.* **2020**, *362*, 594–600.
- [46] S. Wang, N. Luo, Y. Li, C. Wang, *Org. Lett.* **2019**, *21*, 233–236.
- [47] A. K. Bains, D. Adhikari, *Catal. Sci. Technol.* **2019**, *9*, 9051–9059.
- [48] R. Mondal, I. B. Lozada, O. Stotska, D. E. Herbert, *J. Org. Chem.* **2018**, *57*, 4966–4978.
- [49] N. Deibl, R. Kempe, *Angew. Chem. Int. Ed.* **2017**, *56*, 1663–1666.
- [50] M. Mastalir, M. Glatz, E. Pittenauer, G. Allmaier, K. Kirchner, *J. Am. Chem. Soc.* **2016**, *138*, 15543–15546.

- [51] R. Mondal, D. E. Herbert, *Organometallics* **2020**, *39*, 1310–1317.
- [52] M. Maji, S. Kundu, *Dalton Trans.* **2019**, *48*, 17479–17487.
- [53] A. K. Bains, D. Adhikari, *Catal Sci Technol*, **2020**, *10*, 6309–6318.
- [54] Y. F. Nishimura, T. Hamaguchi, S. Yamaguchi, H. Takagi, K. Dohmae, T. Nonaka, Y. Nagai, *J. Phys. Conf. Ser.* **2016**, *712*, 012067–012072.
- [55] A. I. Frenkel, *Chem. Soc. Rev.* **2012**, *41*, 8163–8178.
- [56] S. Bhlapibul, K. Pruksathorn, P. Piumsomboon, *Renew. Energy* **2012**, *41*, 262–266.
- [57] A. E. Yarulin, R. M. Crespo-Quesada, E. V. Egorova, L. L. Kiwi-Minsker, *React. Kinet. Catal.* **2012**, *53*, 253–261.
- [58] F. Tao, M. E. Grass, Y. Zhang, D. R. Butcher, J. R. Renzas, Z. Liu, J.Y. Chung, B. S. Mun, M. Salmeron, G.A. Somorjai, *Science* **2012**, *41*, 7977–7979.
- [59] H. Kobayashi, M. Yamauchi, H. Kitagawa, Y. Kubota, K. Kato, M. Takata, *J. Am. Chem. Soc.* **2008**, *130*, 1818–1819.
- [60] S. Hayashi, R. Ishida, S. Hasegawa, S. Yamazoe, T. Tsukuda, *Top. Catal.* **2018**, *54*, 5915–5918.
- [61] Y. Hashiguchi, I. Nakamura, T. Honma, T. Matsushita, H. Murayama, M. Tokunaga, Y. K. Choe, T. Fujitani, *ChemPhysChem* **2023**, *24*, e202200389.
- [62] J. Y. Xu, W. H. Cheng, X. Zhu, H. L. Wu, K. Wang, *Asian J. Chem.* **2008**, *5*, 847–853.
- [63] T. Shi, F. Qin, Q. Li, W. Z hang, *Org. Biomol. Chem.* **2018**, *48*, 9487–9491.

Concluding Remarks

In this dissertation, I systematically studied a flow synthesis process for core-shell nanoparticle catalysts.

In Chapter 2, I developed a flow synthesis method for Pd@Pt catalysts. I found that Pd@Pt NPs can be synthesized by sequential mixing of Pd precursor, Pt precursor, and reducing agent using a flow reactor. Furthermore, by modifying the loading process on the catalytic support, I succeeded in synthesizing Pd@Pt/C without using polymeric capping agents (PVP K30) that inhibit ORR activity. The obtained flow-synthesized Pd@Pt/C showed higher ORR activity than Pt/C, but lower activity than the core-shell catalyst synthesized by the Cu-UPD method. Nevertheless, I have demonstrated that the flow process is an effective method for the synthesis of core-shell NPs catalysts that can achieve continuity, productivity, and scalability.

In Chapter 3, I developed a flow synthesis process for Pd@Pt_{1ML}/C with highly controlled Pt shell thickness. First, the structural analysis by XAFS revealed that the low activity of flow synthesized Pd@Pt/C was caused by the heterogeneity of the Pt shell structure. Next, a new high-throughput flow synthesis system for the preparation of core-shell catalysts was developed and various process conditions were rapidly evaluated. As a result, Pd@Pt_{1ML}/C with a uniform monoatomic layer of Pt shell was successfully synthesized by using 2-MePy·BH₃ as the reducing agent for Pt. The role of 2-MePy is to coordinate to Pt with N to suppress the stacking of Pt shells to form a uniform Pt_{1ML} shell, and to suppress the aggregation of the formed NPs. The obtained Pd@Pt_{1ML}/C catalyst was confirmed by XAFS and TEM-EDS and EELS results to have 1 ML of Pt shell as the average structure as well as single particles. ORR activity evaluation showed that Pd@Pt_{1ML}/C exhibited about 3 times higher gravimetric activity than Pt/C. This ORR activity is comparable to that of core-shell catalysts synthesized by the Cu-UPD method. Therefore, this flow method is a promising alternative to the Cu-UPD method for the synthesis of core-shell type catalysts with both high productivity and advanced catalyst structure control.

In Chapter 4, the effect of Pt shell thickness on the ORR reaction was studied to elucidate the ORR activity factors of core-shell type catalysts. The results of Pd@Pt model surface experiments showed that the charge transfer from Pd to Pt (Pt^{δ-}) is stronger and the ORR activity is higher when the Pt shell thickness is thinner. DFT calculations also support the charge transfer to Pt, further suggesting that the core-shell conversion lowers the activation energy of the rate-determining step of the ORR. These findings are useful for future development of new core-shell catalysts with higher activity.

In Chapter 5, to further validate the usefulness of the flow-synthesized Pd@Pt catalyst, I investigated its application to organic synthetic reactions. As a result, Pd@Pt catalyst was found to be more active than Pt catalyst in the three-component one-pot synthesis of multi substituted pyrimidines, confirming the potential of the core-shell catalyst for application development.

Acknowledgements

This research was carried out under the supervision of Prof. Makoto Tokunaga in Department of Chemistry, Graduate school Science, Kyushu University. I would like to express my gratitude to Professor Makoto Tokunaga. I appreciate that he gave me great insight into chemistry and invaluable suggestion, and always warmly encouraged me.

I also would like to express my deepest gratitude to Dr. Tadahiro Fujitani (National Institute of Advanced Industrial Science and Technology (AIST)). I have learned a lot from his enthusiastic and warm guidance on my research approach. He also reviewed this disratitation.

I would also like to thank Prof. Ryoichi Kuwano (Kyushu University) for reviewing this disratitation. I believe that my research has been developed by the very thought-provoking comments I received at the research presentation meeting.

I would like to thank Associate Prof. Haruno Murayama and Assistant Prof. Eiji Yamamoto (Kyushu University) for their enthusiastic guidance in conducting this research. They gave me a lot of advice in the laboratory seminar and also reviewed this disratitation.

I would like to thank Dr. Isao Nakamura, Dr. Sharmin Sultana Poly, and Dr. Fumihiro Watanabe (AIST) for their cooperation in various experiments and for their guidance and advice on my research. I would like to take this opportunity to thank them. I would also like to express deep appreciation to Mr. Kosuke Sato (Research Association of High-Throughput Design and Development for Advanced Functional Materials) for his cooperation in many experiments, including the evaluation of catalytic activity.

I am deeply grateful to Dr. Tetsuo Honma (Japan Synchrotron Radiation Research Institute) for teaching and supporting about XAFS measurements and result in analysis. I also would like to express my thanks to Dr. Yoong-Kee Choe (AIST) and Prof. Shigeyoshi Sakaki (Kyoto University) for their collaboration on DFT calculation. In addition, I would like to thank to Prof. Ken-ichi Shimizu, Mr. Shunsaku Yasumura (Hokkaido University), and Asima Sultana (AIST) for their collaboration on research of pyrimidine synthesis.

I would like to thank Ms. Yukari Uchida, a secretary of the laboratory. She always helped me to handle various procedures. I also would like to show my deep appreciation to the other laboratory members.

This work is based on results obtained from project (JPNP16010) commissioned by New Energy and Industrial Technology Development Organization (NEDO). I would like to thank all involved.

I also would like to express my deepest gratitude to my supervisors, seniors, and colleagues at UBE Corporation: Mr. Hiroyuki Miyata, Dr. Tetsurou Tsuji, Dr. Tatsuya Kawaguchi, Mr. Hiroyuki

Takagi, Mr. Toshiyuki Matsushita, Mr. Kimihiko Yoshimura, Dr. Yasuhiro Tanaka, Mr. Kazuto Nakamura, Mr. Suguru Fukazawa.

Finally, special thanks are given to my family for their warm encouragement and constant support.

Yuta Hashiguchi

List of Publications

- [1] Sharmin Sultana Poly, Yuta Hashiguchi, Asima Sultana, Isao Nakamura, Ken-ichi Shimizu, Shunsaku Yasumura, Tadahiro Fujitani, Flow reactor approach for the facile and continuous synthesis of efficient Pd@Pt core-shell nanoparticles for acceptorless dehydrogenative synthesis of pyrimidines from alcohols and amidines, *Appl Catal. A* **2021**, *619*, 118158.
- [2] Yuta Hashiguchi, Fumihiro Watanabe, Tetsuo Honma, Isao Nakamura, Sharmin Sultana Poly, Tatsuya Kawaguchi, Tetsuro Tsuji, Haruno Murayama, Makoto Tokunaga, Tadahiro Fujitani, Continuous-flow synthesis of Pd@Pt core-shell nanoparticles, *Colloids Surf. A* **2021**, *620*, 126607.
- [3] Yuta Hashiguchi, Isao Nakamura, Tetsuo Honma, Toshiyuki Matsushita, Haruno Murayama, Makoto Tokunaga, Yoong-Kee Choe, Tadahiro Fujitani, Effects of the Pt Shell Thickness on the Oxygen Reduction Reaction on a Well-Defined Pd@Pt Core-Shell Model Surface, *ChemPhysChem* **2023**, *24*, e202200389.